

**THERMAL ASSESSMENT OF LIQUEFIED NATURAL GAS STORAGE TANKS**

by

Zhihao Wang

B.A.Sc, Harbin Engineering University, 2008

M.A.Sc., Tsinghua University, 2011

A THESIS SUBMITTED IN PARTIAL FULFILLMENT OF  
THE REQUIREMENTS FOR THE DEGREE OF

DOCTOR OF PHILOSOPHY

in

THE FACULTY OF GRADUATE AND POSTDOCTORAL STUDIES  
(Mechanical Engineering)

THE UNIVERSITY OF BRITISH COLUMBIA

(Vancouver)

June 2021

© Zhihao Wang, 2021

The following individuals certify that they have read, and recommend to the Faculty of Graduate and Postdoctoral Studies for acceptance, the dissertation entitled:

Thermal Assessment of Liquefied Natural Gas Storage Tanks

submitted by Zhihao Wang in partial fulfillment of the requirements for

the degree of Doctor of Philosophy

in Mechanical Engineering

**Examining Committee:**

Dr. Walter Mérida, Mechanical Engineering, UBC

Supervisor

Dr. Sheldon Green, Mechanical Engineering, UBC

Supervisory Committee Member

Dr. Patrick Kirchen, Mechanical Engineering, UBC

Supervisory Committee Member

Dr. C. Jim Lim, Chemical and Biological Engineering, UBC

University Examiner

Dr. Mark Martinez, Chemical and Biological Engineering, UBC

University Examiner

**Additional Supervisory Committee Members:**

Dr. Ian Frigaard, Mechanical Engineering, UBC

Supervisory Committee Member

## **Abstract**

In this Ph.D. research study, a non-equilibrium thermodynamic model and a non-equilibrium multilayer thermodynamic model are developed to assess the thermal performance of liquefied natural gas (LNG) storage tanks by reducing the computation time compared with computational fluid dynamics (CFD) methods.

The non-equilibrium thermodynamic model incorporates a resistance-capacitance network to evaluate the thermal performance of vertical and horizontal LNG storage tanks. This model is validated against two sets of experimental data, and compared with the equilibrium thermodynamic model. The results indicate that, under stationary conditions, the equilibrium and non-equilibrium thermodynamic models predict the pressure and temperature profiles in the vertical and horizontal LNG storage tanks with good accuracy. However, the non-equilibrium thermodynamic model is the only model that can predict the thermal performance of the storage tanks under dynamic operating conditions such as sudden pressure changes due to the vapor return to a tank or LNG dispensing to heavy-duty trucks. Also, the results highlight that the LNG holding time in horizontal storage tanks is longer than that in vertical storage tanks under dynamic operating conditions.

The non-equilibrium multilayer thermodynamic model is developed to study the thermal stratification and rollover in LNG storage tanks. This model divides the liquid and vapor domains in the tanks into multi-layers, considers the boundary layer formation along the tank vertical walls

and, uses adaptive mesh to accommodate the changes in the LNG level over time. This model is verified against experimental data available in the literature to predict the thermal stratification and rollover in cryogenic storage tanks. The parametric study indicates that in atmospheric LNG storage tanks, the amount of heat transfer to the tank and the tank aspect ratio (i.e., diameter to height ratio) do not affect the rollover start time. However, they affect the LNG evaporation rate. The rollover start time is directly affected by the ratio between the amount of fresh LNG loaded to the tank (cargo) and the amount of LNG left in the tank (heel) before loading the cargo. This work suggests that the cargo to heel ratio should be monitored regularly to prevent the rollover in LNG storage tanks.

## **Lay Summary**

In this Ph.D. study, the non-equilibrium and non-equilibrium multilayer models are developed to evaluate the thermal performance of liquefied natural gas (LNG) storage tanks with minimum computation time.

The results of the equilibrium and non-equilibrium thermodynamic modelling indicate that they can predict the thermal performance of storage tanks under stationary conditions. Under dynamic conditions, the non-equilibrium thermodynamic model is the only model that can predict the thermal performance of the storage tanks.

The non-equilibrium multilayer thermodynamic model successfully predicts the thermal stratification and rollover in storage tanks. The results demonstrate that the heat transfer rate to the tank and the tank diameter to height ratio do not affect the rollover start time. In contrast, the ratio between the fresh LNG loaded to the tank and the LNG left in the tank is a key factor in the rollover start time. This ratio should be monitored regularly to prevent the rollover.

## Preface

The original idea of developing the numerical models to investigate the thermal performance in the liquefied natural gas storage tanks was proposed by my supervisor, Dr. Walter Mérida.

Zhihao Wang is responsible for identifying and analyzing the specific topics of this Ph.D. research documented herein. He contributed to the establishment of the numerical models and the models' algorithm, model validation, and results analysis from the numerical models in the form of conferences and publications.

Zhihao Wang completed the development of in-house computer programming codes and the editorial preparation of this dissertation under the supervision of Dr. Walter Mérida. I would like to acknowledge our collective group members, Dr. Amir Sharafian and Dr. Paul Blomerus, who offered critical suggestions during the model development and results discussion.

- Chapter 1 is composed from the final version of Zhihao Wang's Ph.D. proposal and the literature review study prepared throughout this Ph.D. research project.
- The description of the non-equilibrium thermodynamic model in Chapter 2 and results analysis of the non-equilibrium thermodynamic model in Chapter 3 has been published in an ISI journal paper:

Z. Wang, A. Sharafian, and W. Mérida, "Non-equilibrium thermodynamic model for liquefied natural gas storage tanks," *Energy*, vol. 190, 2020.

and an international conference paper

Z. Wang, A. Sharafian, and W. Mérida, "Evaluate the Performance of Vertical and Horizontal Liquefied Natural Gas Storage Tanks by Using a Non-Equilibrium Resistance-Capacitance Model." *Proceedings of the ASME 2019 International Mechanical Engineering Congress and Exposition. Volume 8: Heat Transfer and Thermal Engineering.* Salt Lake City, Utah, USA. November 11–14, 2019. V008T09A086. ASME.

Zhihao Wang was responsible for the establishment of the non-equilibrium thermodynamic model, code programming, and results analysis. Dr. Walter Mérida provided the idea of evaluating the thermal performance of liquefied natural gas storage tanks. Drs. Walter Mérida and Amir Sharafian offered critical suggestions on the discussion of the results, and the revision of the manuscripts.

- The description of the non-equilibrium multilayer thermodynamic model in Chapter 2 and the results analysis of the non-equilibrium multilayer thermodynamic model in Chapter 4 are incorporated into a manuscript that was submitted to a peer-reviewed journal in April 2021. Now received revision feedback (June 2021).

Z. Wang, A. Sharafian, and W. Mérida, "Thermal stratification and rollover phenomena in liquefied natural gas tanks."

Zhihao Wang was responsible for developing the non-equilibrium multilayer thermodynamic model, code programming, and results analysis. Drs. Walter Mérida and Amir Sharafian offered critical suggestions on the results discussion, and revision of the manuscript.

# Table of Contents

<b>Abstract.....</b>	<b>iii</b>
<b>Lay Summary .....</b>	<b>v</b>
<b>Preface.....</b>	<b>vi</b>
<b>Table of Contents .....</b>	<b>viii</b>
<b>List of Tables .....</b>	<b>xii</b>
<b>List of Figures.....</b>	<b>xiv</b>
<b>List of Symbols .....</b>	<b>xvii</b>
<b>List of Abbreviations .....</b>	<b>xxiv</b>
<b>Glossary .....</b>	<b>xxv</b>
<b>Acknowledgements .....</b>	<b>xxvii</b>
<b>Dedication .....</b>	<b>xxix</b>
<b>Chapter 1: Introduction .....</b>	<b>1</b>
1.1 Background.....	1
1.2 Analyzing the thermal performance of LNG storage tanks .....	6
1.3 Rollover phenomenon and pertinent literature review.....	17
1.4 Research objectives.....	22
1.5 Technical road map.....	23
<b>Chapter 2: Development of Non-equilibrium and Non-equilibrium Multilayer</b>	
<b>Thermodynamic Models.....</b>	<b>25</b>
2.1 Non-equilibrium thermodynamic model.....	26
2.1.1 Governing equations in the non-equilibrium thermodynamic model.....	27

2.1.1.1	Conservation of mass in the liquid and vapor phases .....	27
2.1.1.2	Conservation of energy in the liquid and vapor phases .....	29
2.1.1.3	Heat transfer rate through the tank wall.....	31
2.1.1.4	Heat transfer rate at the vapor-liquid interface .....	34
2.1.1.5	Equation of state .....	35
2.1.2	Computational algorithm in the non-equilibrium thermodynamic modelling .....	38
2.1.2.1	Equilibrium thermodynamic modelling.....	38
2.1.2.2	Non-equilibrium thermodynamic modelling .....	39
2.2	Non-equilibrium multilayer thermodynamic model .....	41
2.2.1	Governing equations in the non-equilibrium multilayer thermodynamic model.....	41
2.2.1.1	Conservation of mass in the liquid and vapor phases .....	41
2.2.1.2	Conservation of energy in the liquid and vapor phases .....	45
2.2.1.3	Boundary layer.....	49
2.2.1.4	Thermal stratification in the liquid domain .....	50
2.2.1.5	Mass transfer between the heel and cargo layers.....	51
2.2.2	Computational algorithm in the non-equilibrium multilayer thermodynamic modelling .....	54
<b>Chapter 3: Results from Non-equilibrium Thermodynamic Modelling.....</b>		<b>56</b>
3.1	Model validation .....	56
3.1.1	The horizontal tank .....	56
3.1.2	The vertical tank .....	58
3.2	Base-case model analysis.....	63
3.3	Performance of LNG storage tanks in refueling stations during truck refueling.....	70

3.4	Summary .....	74
<b>Chapter 4: Results from Non-equilibrium Multilayer Thermodynamic Modelling .....</b>		<b>75</b>
4.1	Model validation .....	75
4.2	Parametric study on the rollover start time .....	80
4.2.1	Effect of heat transfer rate to the tank on the rollover start time .....	81
4.2.2	Effect of cargo to heel height ratio on the rollover start time .....	82
4.2.3	Effect of tank aspect ratio on the rollover start time .....	84
4.3	Summary .....	85
<b>Chapter 5: Conclusions and Future Work .....</b>		<b>87</b>
5.1	Contributions of this Ph.D. work .....	87
5.2	Conclusions .....	87
5.2.1	Analysis of the non-equilibrium thermodynamic model .....	87
5.2.2	Analysis of the non-equilibrium multilayer thermodynamic model .....	88
5.3	The limitations and future work .....	89
<b>Bibliography .....</b>		<b>92</b>
<b>Appendices .....</b>		<b>105</b>
<b>Appendix A .....</b>		<b>105</b>
A.1	Thermal resistance-capacitance network .....	105
A.2	Heat transfer coefficients in the vertical LNG storage tank .....	109
A.3	Heat transfer coefficients in the horizontal LNG storage tank .....	111
<b>Appendix B .....</b>		<b>112</b>
B.1	Vapor-liquid equilibrium calculations .....	112
B.2	Calculation of the bubble pressure .....	113

B.3	Calculation of the dew pressure .....	114
B.4	Calculation of the bubble temperature .....	115
B.5	Calculation of the dew temperature .....	116
B.6	Dynamic viscosity and thermal conductivity of the liquid and vapor phases.....	116

## List of Tables

Table 1.1. A review of studies on the thermal performance of LNG storage tanks by using the CFD simulation. ....	6
Table 1.2. A review of analytical and lumped-parameter models to predict the thermal stratification in cryogenic storage tanks. ....	12
Table 1.3. A review of studies on the rollover in cryogenic storage tanks. ....	19
Table 3.1. The geometry, thermal properties, and initial conditions in a horizontal LNG storage tank reported by Harper and Powars [89]. ....	57
Table 3.2. The geometry of the vertical tank and its initial conditions in the experiment of Ludwig et al. [90]. ....	59
Table 3.3. Radial and axial locations for the thermocouples inside the vertical nitrogen tank [90]. ....	60
Table 3.4. Specs of vertical and horizontal LNG storage tanks, and boundary and initial conditions. ....	64
Table 4.1. The tank geometry in the La Spezia rollover incident [26]. ....	76
Table 4.2. Initial composition of LNG and vapor phase [27], LNG level, pressure, as well as the temperature and densities of LNG in the heel and cargo layers, and the vapor phase. ....	76
Table 4.3. The thermal boundary conditions on the tank in the La Spezia rollover incident [27]. ....	77
Table 4.4. The initial LNG and gaseous natural gas compositions, temperatures, and densities used for the parametric study. ....	81

Table A1. Details of the thermal resistance-capacitance network shown in Figure 2.3. .... 105

Table A2. Variables in the calculation of the convection transfer coefficients on the wall. .... 110

## List of Figures

Figure 1.1. Shares of coal and natural gas as a primary energy source in (a) the United States and (b) China between 1990 and 2018 [8].....	2
Figure 1.2. The thermal phenomenon in LNG storage tanks: (a) thermal stratification (b) rollover.....	5
Figure 1.3. Scope of the Ph.D. research project and applications. ....	24
Figure 2.1. (a) Schematic of heat and mass transfer in an LNG storage tank and (b) the main segments of the LNG storage tank considered in the non-equilibrium thermodynamic model. ..	26
Figure 2.2. Details of the heat transfer from the environment to the liquid and vapor phases inside a vertical storage tank.....	32
Figure 2.3. The thermal resistance-capacitance network for vertical and horizontal storage tanks. The dashed lines are only for the horizontal storage tanks.....	32
Figure 2.4. The flow chart of solving governing equations for the equilibrium and non-equilibrium thermodynamic modelling. The dotted and dashed lines are for the equilibrium and non-equilibrium thermodynamic modelling, respectively.....	40
Figure 2.5. A schematic of the multilayer model in the liquid and vapor domains in a vertical cylindrical storage tank.....	42
Figure 2.6. Flow chart to solve the governing equations in a non-equilibrium multilayer thermodynamic model for a cryogenic vertical storage tank.....	55

Figure 3.1. A comparison between the results of the equilibrium and non-equilibrium thermodynamic models developed in this study and the experimental data of a horizontal tank reported by Harper and Powars [89]...... 58

Figure 3.2. Schematic of the liquid nitrogen vertical tank and the location of thermocouples [90]. ..... 59

Figure 3.3. Comparison of equilibrium thermodynamic, non-equilibrium thermodynamic, and CFD models against the experimental data of Ludwig et al. [90]: (a) Tank pressure and (b) temperature profiles in the vapor and liquid nitrogen..... 62

Figure 3.4. Thermal performance of the vertical LNG storage tank at 50% and 80% initial LNG filling levels: (a) pressure, (b) temperature, (c) LNG level, (d) total heat transfer rate to the storage tank, (e) inner vertical wall temperature, and (f) outer vertical wall temperature. .... 65

Figure 3.5. Thermal performance of the horizontal LNG storage tank at 50% and 80% initial LNG filling levels: (a) pressure, (b) temperature, (c) LNG level, (d) total heat transfer rate to the storage tank, (e) inner top and bottom wall temperatures, and (f) outer top and bottom wall temperatures..... 68

Figure 3.6. (a) Holding time and (b) average daily BOG generation rate of the vertical and horizontal LNG storage tanks calculated by using the equilibrium and non-equilibrium thermodynamic models at the base-case conditions given in Table 3.4. .... 70

Figure 3.7. Changes in the pressure and temperature of (a, b) vertical storage tank and (c, d) horizontal storage tank to fuel the fleet of 10 trucks. .... 72

Figure 3.8. Changes in the pressure and temperature of (a, b) vertical storage tank and (c, d) horizontal storage tank to fuel the fleet of 20 trucks. .... 74

Figure 4.1. A schematic of the LNG storage tank in the La Spezia rollover incident in 1971..... 76

Figure 4.2. Changes in the LNG densities adjacent to the heel-cargo interface over time calculated by the non-equilibrium multilayer thermodynamic model and compared against the experimental rollover time [26]. ..... 78

Figure 4.3. (a) LNG temperature profiles in the cargo and heel layers, (b) temperature distribution and thermal stratification in the tank over time, (c) LNG density profiles in the cargo and heel layers at the rollover start time, and (d) changes in the methane (CH<sub>4</sub>) mole fraction in the cargo and heel layer over time. .... 79

Figure 4.4. Effect of heat transfer rate from the environment to the LNG storage tank on the rollover start time: (a) bulk temperatures of heel and cargo layers, (b) LNG evaporation accumulation over time, (c) the LNG density at the heel-cargo interface, and (d) the rollover start time. .... 82

Figure 4.5. Effect of cargo to heel height ratio on the rollover start time: (a) bulk temperatures of heel and cargo layers, (b) LNG evaporation accumulation over time, (c) the LNG density at the cargo-heel interface, and (d) the rollover start time..... 83

Figure 4.6. Effect of tank aspect ratio on the rollover start time: (a) bulk temperatures of the heel and cargo layers, (b) LNG evaporation accumulation over time, (c) the LNG density at the cargo-heel interface, and (d) the rollover start time. .... 85

## List of Symbols

$A$	Area, $m^2$
	Coefficient defined in the standard Peng-Robinson Equation of State
$A_{ij}$	Binary parameters defined in the Peng-Robinson Equation of State
$AR$	Aspect ratio
$a, b$	Coefficients defined in the standard Peng-Robinson Equation of State
$B$	Coefficient defined in the standard Peng-Robinson Equation of State
$C$	Thermal mass, $J/K$
$c$	Volume-translated term defined in volume-translated Peng-Robinson Equation of State
$c_l$	Species-dependent parameter defined in volume-translated Peng-Robinson Equation of State
$c_p$	Specific heat capacity at constant pressure, $J/kg \cdot K$
$c_{species\ i}$	Molar volume concentrations of species $i$ , $kmole/m^3$
$D_{inner}$	Tank inner diameter, $m$
$d$	Dimensionless distance function defined in volume-translated Peng-Robinson Equation of State
$d_{layer\ i}$	Thickness of liquid or vapor layer cell $i$ , $m$
$f_c, f_e$	Condensation and evaporation coefficient, $s^{-1}$
$f_\omega$	Constant coefficient defined in the Peng-Robinson Equation of State

$Gr$	Grashof number calculated based on the temperature difference between a fluid and a wall
$Gr_q$	Grashof number calculated based on the heat flux rate applied to the wall
$g$	Gravity acceleration, $m/s^2$
$H$	Height, $m$
$h$	Specific mass enthalpy of fluids, $J/kg$ Molar enthalpy of liquid or vapor phase defined in the Peng-Robinson Equation of State, $J/kmol$
$h_{interface}$	Convective heat transfer coefficients at the vapor-liquid interface, $W/m^2 \cdot K$
$h_{mass,species\ i}$	Convective mass transfer film coefficient for species $i$ , $m/s$
$K_i$	K-values from vapor-liquid equilibrium state for species $i$
$K_{species\ i}^e$	K-values from liquid evaporation for species $i$
$K_{species\ i}^c$	K-values from vapor condensation for species $i$
$\bar{k}$	Average thermal conductivity of vapor or liquid phases, $W/m \cdot k$
$k_{ij}$	Binary coefficients defined in the calculation of thermal conductivity of a liquid mixture based on Li model
$L_{ref}$	Reference length, $m$
$l$	Distance of numerical cell from the vapor-liquid interface, $m$
$M$	Molar mass, $kg/kmol$
$m$	Mass, $kg$
$\dot{m}$	The upward mass flow rates in the boundary layer, $kg/s$
$\dot{m}_e$	Evaporation rate, $kg/s$

$\dot{m}_c$	Condensation rate, $kg/s$
$\dot{m}'''_{cond}$	Volumetric condensation rate, $kg/(s \cdot m^3)$
$\dot{m}'''_{evap}$	Volumetric evaporation rate, $kg/(s \cdot m^3)$
$N$	Mole numbers in vapor or liquid phase layer, $kmol$
	Total quantities of species in the liquid and vapor mixtures
$Nu$	Nusselt number
$n$	Total layers in vapor or liquid phase
$P$	Pressure, $Pa$
$\mathcal{P}_{interface}$	Perimeter of the heel-cargo interface, $m$
$Pr$	Prandtl number
$\dot{Q}$	Heat transfer rate, $W$
$\dot{q}''$	Heat flux rate, $W/m^2$
$R$	Thermal resistance, $K/W$
$R_{inner}$	Inner radius of the tank, $m$
$R_u$	Universal gas constant, $J/mol \cdot K$
$Ra$	Rayleigh number
$T$	Temperature, $K$
$t$	Time, $s$
$t_{insulation}$	Thickness of insulation layer in LNG storage tanks, $m$
$U$	Total internal energy, $J/kg$
	Overall heat transfer coefficient, $W/m^2 \cdot K$
$u$	Specific mass internal energy of liquid or vapor phases, $J/kg$

$V$	The average velocity of the upward boundary-layer flow, $m/s$
$\forall$	Volume, $m^3$
$\nu$	Specific molar volume, $m^3/kmol$
$\nu_{PR}$	Specific molar volume calculated by standard Peng-Robinson Equation of State, $m^3/kmol$
$\nu_{VTPR}$	Specific molar volume calculated by volume-translated Peng-Robinson Equation of State, $m^3/kmol$
$w$	Mass fraction of the species $i$ , $kg/kg$
$x_i$	Molar fraction of species $i$ in the liquid phase, $mol/mol$
$y_i$	Molar fraction of species $i$ in the vapor phase, $mol/mol$
$Z$	Compressibility factor

*Greek letter*

$\alpha$	Thermal diffusivity, $m^2/s$
$\alpha_{specie i}$	Molar volume concentration expansion coefficient, $m^3/kmole$
$\beta$	Thermal expansion coefficient, $1/K$
$\Delta$	Thickness of the thermal stratification layer, $m$
$\delta$	Thickness of liquid and vapor layers affected by the evaporation and condensation, $m$
	Thickness of the velocity boundary layer, $m$
$\delta_c$	Volume correction at the critical temperature defined in volume-translated Peng-Robinson Equation of State
$\eta$	Cargo to heel height ratio

$\mu$	Dynamic viscosity, $Pa\cdot s$
$\nu$	Kinematic viscosity, $m^2/s$
$\zeta$	Adjustment factor
$\rho$	Density, $kg/m^3$
$\phi$	Superficial volume fraction
	Fugacity
$\omega$	Acentric factor in the Peng-Robinson Equation of State
	Relaxation coefficient

### *Superscripts*

<i>I</i>	Conduction domain in the liquid phase
<i>II</i>	Convection domain in the liquid phase
<i>ideal</i>	Ideal gas
<i>initial</i>	Initial value
<i>new</i>	New value in the iteration
<i>ref</i>	Reference
<i>t</i>	Time step

### *Subscripts*

<i>i,j,k</i>	Index of layers in liquid and vapor phases
<i>i,j</i>	Species <i>i, j</i>
<i>BL</i>	Boundary layer
<i>Bulk</i>	Bulk fluid outside the boundary layer
<i>b</i>	Tank bottom wall

<i>bubble</i>	Bubble point of liquid mixture
<i>cri</i>	Critical
<i>cross</i>	Cross-section
<i>dew</i>	Dew point of vapor mixture
<i>dis</i>	Liquid dispensing
<i>evap</i>	Evaporation
<i>f</i>	Fluid (liquid or vapor phase)
<i>fil</i>	Liquid filling
<i>heat</i>	Convective heat transfer
<i>i</i>	Inner
<i>inj</i>	Vapor injection
<i>insulation</i>	Insulation layer
<i>interface</i>	Vapor-liquid interface
<i>L, l</i>	Liquid
<i>layer</i>	Liquid or vapor layer
<i>mix</i>	Mixture
<i>mass</i>	Convective mass transfer
<i>o</i>	Outer
<i>ref</i>	Reference
<i>sat</i>	Saturation
<i>t</i>	Tank top wall
<i>tank</i>	Cryogenic storage tank

<i>total</i>	Total
<i>V, v</i>	Vapor
<i>wall</i>	Tank side wall

## List of Abbreviations

BOG	Boil-off gas
CFD	Computational fluid dynamics
EoS	Equation of state
FEM	Finite element method
GHG	Greenhouse gas
LNG	Liquefied natural gas
MAWP	Maximum allowable working pressure
PR	Peng-Robinson
VLE	Vapor-liquid equilibrium

## Glossary

<i>Boil-off gas</i>	The gas evaporated from the vapor-liquid interface in an LNG storage tank due to the heat transfer from the environment.
<i>Equilibrium thermodynamic model</i>	A thermodynamic model developed based on the assumption that changes in the vapor and liquid phases are slow enough to ensure the system reaches the equilibrium state at each time step.
<i>LNG holding time</i>	The maximum duration of holding LNG in a storage tank until the pressure of the tank reaches its maximum allowable working pressure without venting.
<i>Non-equilibrium thermodynamic model</i>	A thermodynamic model developed based on the assumption that the vapor and liquid phases are two independent control volumes, and exchange heat and mass at the vapor-liquid interface.
<i>Non-equilibrium multilayer thermodynamic model</i>	A thermodynamic model developed based on the assumption that the vapor and liquid phases are two independent control volumes, and exchange heat and mass at the vapor-liquid interface. Also, the liquid and vapor domains are divided into multilayers (control volumes) to show the temperature gradients in each domain.
<i>Rollover</i>	A sudden pressure increase in an LNG storage tank due to the mixing of two stratified LNG layers in a short period of time.

*Thermal stratification*      The temperature gradient formed in an LNG storage tank due to the fluid buoyancy effect.

## **Acknowledgements**

First of all, I would like to sincerely appreciate my Ph.D. supervisor, Dr. Walter Mérida, who introduced me to the clean energy field, especially in the liquefied natural gas sector. He supplied the direction of the entire Ph.D. research work and gave me insightful and constructive feedback in addressing problems, academic presentations, and dissertation manuscript editing. In addition, he consistently cared about the research progress through the entire Ph.D. research work around his busy schedule. His meticulous attitude and professional insights continuously motivated me to be an independent thinker, and an excellent researcher in the future. I am sure the motivation will benefit me forever. Working with Dr. Walter Mérida is one of the most enjoyable experiences in my life.

I also extend my gratitude to the natural gas research group leader, Dr. Amir Sharafian. He supplied me with numerous suggestions during every team meeting. During my Ph.D. study, the academic discussion with him expanded my technical knowledge. His enthusiasm and perseverance in the research embraced me to face the obstacles positively during the research and solved them progressively. I was greatly benefited from his meticulous attitude to the presentation and academic writing. This rewarding experience has shaped my academic character.

I also want to thank Drs. Omar Herrera and Paul Blomerus, who supplied helpful guidance during the initial phase of my Ph.D. life. I would also extend my appreciation to my supervisory

committee: Drs. Sheldon Green, Patrick Kirchen, and Ian Frigaard for their feedback on my research proposal.

To the members of Mérida labs, past and present, great thanks for creating a lovely, friendly, fun work environment. Special thanks to Hadyan Ramadhan, who also worked in the natural gas team during 2018-2020, and brought peer review on my research. Special thanks also go to Ms. Nadia Adame, who supported many suggestions and encouragements on my presentation skills.

I also deliver thanks to my friends who have always been here to support me morally. Special attention to Elvis (Zhenglun) Cai who was also a former member in my lab, Chien-I Wu, Jingrong Lin, Hewen Chen, and Kevin Wei.

The financial support of the Natural Sciences and Engineering Research Council of Canada (NSERC) is gratefully acknowledged.

Particular thanks to my beloved family. My parents, Zhaoying Liang and Lei Wang, their loving considerations and continuous support both morally and financially helped me throughout this endeavor. Also, my cousin, Zhijia Wang encouraged me and gave me great confidence during the hard time. Thanks for your endless support and love. Without you, it would be impossible to complete this work.

## **Dedication**

*This dissertation is dedicated to my beloved family*

# Chapter 1: Introduction

## 1.1 Background

The scientific community has considered the increase in greenhouse gas (GHG) emissions as a primary cause of the recent increase in the global mean temperature and changes in the hydrological cycle [1]. The research conducted by International Energy Agency (IEA) demonstrated that coal combustion is the single primary contributor to the global temperature increase, and CO<sub>2</sub> emissions due to burning coal contributed more than 0.3°C in 1°C increase in the global mean annual surface temperature beyond the pre-industrial level [2]. According to IEA, the CO<sub>2</sub> concentration in the atmosphere was around 412.5 parts per million (ppm) in 2020, which increased by at least 45% from the pre-industrial level (ranging from 180 to 280 ppm) [3]. To tackle these challenges, taking immediate actions becomes necessary to protect public health, well-being, and the prosperity of the world [4].

Replacing traditional fossil fuels with low- and zero-carbon alternatives, such as natural gas and hydrogen, has been considered as an effective method to decarbonize the global energy mix and minimize GHG emissions. Abundant natural gas resources can serve as a bridge between traditional fossil fuels and zero-carbon fuels [5,6]. The combustion of natural gas generates around 45% less CO<sub>2</sub> than coal per million British thermal units (Btu) of energy [7], and does not emit particulates. Figure 1.1 shows the shares of coal and natural gas as primary energy sources in the United States and China from 1990 to 2018 [8]. Due to the environmental policies in the two

countries, the demand for natural gas increased in recent decades, and coal is gradually phasing out from the energy sector.

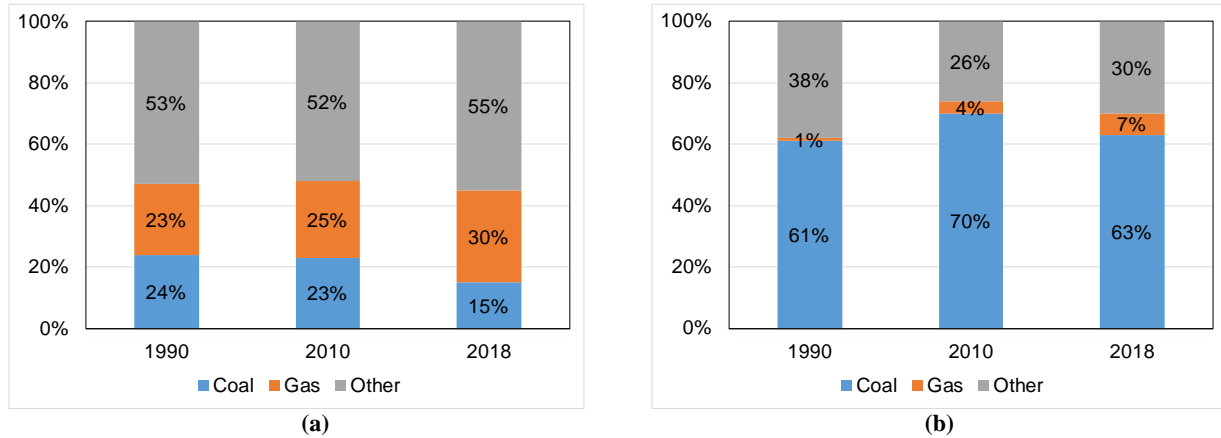


**Figure 1.1. Shares of coal and natural gas as a primary energy source in (a) the United States and (b) China between 1990 and 2018 [8].**

In Canada, the demand for thermal coal is predicted to drop from 34.5 million tons in 2017 to 2.3 million tons in 2040. Meanwhile, the industrial demand for natural gas is expected to increase from 1991.4 Petajoule (PJ) to 3056.8 PJ in 2040 [9]. The broad recognition of the merits of natural gas on the environment promotes coal-to-gas switching, which significantly reduces GHG emissions. During 2011-2019, around 600 million tonnes of equivalent CO<sub>2</sub> were cumulatively saved by replacing coal with natural gas [10], which equals 82% of the total equivalent CO<sub>2</sub> emitted in Canada in 2018 [11]. In line with the increase in the natural gas demand, the global liquefied natural gas (LNG) export hit 359 million tonnes in 2019, which increased by 12.5% from 2018 [10]. Although the demand for natural gas dropped by 4% in 2020 due to the economic slowdown caused by the Covid-19 crisis, the demand is expected to progressively rebound in 2021 at a growth rate of 1.5% until 2025 [12].

Natural gas is widely used for power generation, and industrial and household consumption. Natural gas is transported through pipelines or liquefied and transported by LNG marine carriers and tanker trucks for overseas and inland destinations, respectively.

Natural gas is liquefied at temperatures as low as  $-162^{\circ}\text{C}$  and stored in insulated double-wall storage tanks. LNG is a mixture of light and heavy hydrocarbons, such as methane, ethane, propane, *n*-butane, and other species, such as carbon dioxide and nitrogen [13]. Due to the large temperature gradient between the environment and the LNG inside a storage tank, heat is transferred to the storage tank and evaporates a portion of LNG (called as boil-off gas (BOG)), leading to an increase in the tank pressure. To avoid the over-pressurization of the tank and maintain the tank pressure below its maximum allowable working pressure (MAWP), the BOG is continuously released to the atmosphere [14], burned [15], used as fuel for generators [16], injected to pipelines [17] or re-liquefied [18].

For overseas destinations, LNG is transported by special marine carriers from liquefaction plants to regasification terminals, where it is stored in insulated storage tanks at atmospheric pressure [19]. The BOG generation and its removal from these storage tanks change the LNG composition over time and affect its thermodynamic properties, such as boiling temperature, densities, latent heat, and heating value. Methane is the main constituent of LNG and has the lowest boiling pressure and temperature compared with heavier hydrocarbons. Therefore, methane in the LNG mixture evaporates faster than other species. This preferential evaporation changes the composition of LNG, which is known as LNG weathering or ageing [20].

Beyond power generation applications, LNG can be used as a transport fuel due to its high volumetric energy density (22.2. MJ/L). LNG can substitute diesel and heavy fuel oil in heavy-duty vehicles and marine vessels, respectively [21,22]. LNG in refueling stations and onboard vessels is stored in double-wall vacuum-jacketed storage tanks at high pressures [14]. These pressurized storage tanks can hold LNG for several days without BOG release to the atmosphere. However, poor insulation, the degradation of insulation materials, and the underutilization of LNG can contribute to BOG generation, which gradually decreases the methane content of the LNG mixture. An LNG mixture with a low methane concentration can affect the combustion quality and increase knocking in heavy-duty engines of trucks and marine vessels [23,24].

Besides the weathering phenomenon inside the LNG tanks, the LNG adjacent to the vertical walls of the tank is heated and moves upward under buoyancy forces. Accumulation of the warmer LNG near the vapor-liquid interface creates a warm LNG zone, and its thickness grows due to the continuous heat leak to the tank over time. Consequently, the temperature gradient in the axial direction is developed. This phenomenon is considered as thermal stratification [25] (shown in Figure 1.2(a)). The thermal stratification affects the BOG generation rate and the optimum design for LNG storage tanks.

Another possible cause for thermal stratification in cryogenic storage tanks is the loading of a cryogenic liquid with a different composition (e.g., for the case of LNG) and density (e.g., liquid hydrogen and nitrogen at a different temperature) to the residual cryogenic liquid in the storage tanks (shown in Figure 1.2(b)). The difference between the physical properties of the loaded cryogenic liquid (cargo) and the residual cryogenic liquid inside the storage tank prior to loading

(heel) can cause thermal stratification. In some circumstances, the sudden mixing of these stratified layers causes a significant BOG generation and a sudden pressure increase in the tank. This phenomenon is known as “LNG rollover” [26–28], which caused the failure of the tank structure, as reported previously.

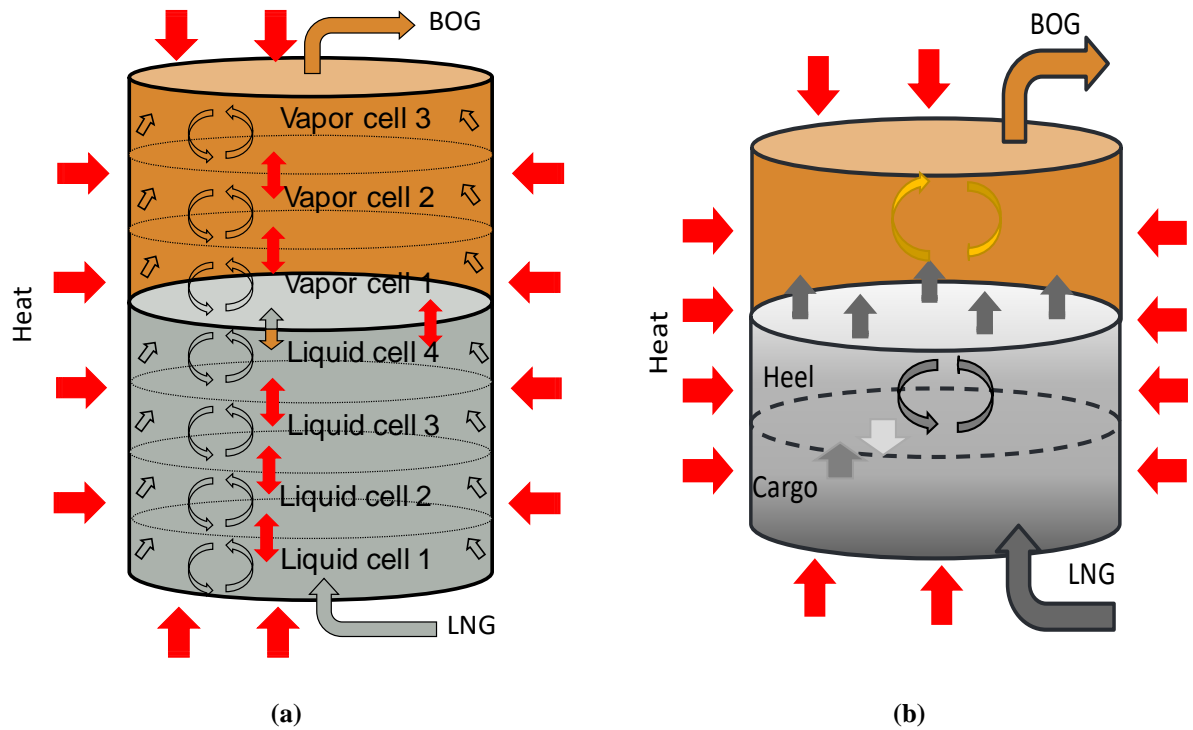


**Figure 1.2. The thermal phenomenon in LNG storage tanks: (a) thermal stratification (b) rollover.**

To tackle these undesired thermal phenomena and deploy LNG safely, having robust numerical models to study atmospheric and pressurized storage tanks becomes crucial. These numerical models help to analyze the thermal performance of LNG storage tanks and determine their heat transfer weaknesses.

## 1.2 Analyzing the thermal performance of LNG storage tanks

Computational Fluid Dynamics (CFD), equilibrium and non-equilibrium thermodynamics models, and analytical models are common methods to analyze the thermal performance of LNG storage tanks.

In the CFD method, the unsteady mass conservation, Navier Stokes (N-S), energy, and mass transfer equations are solved in the entire numerical domain. This method gives accurate results of the thermal stratification and pressure in the cryogenic tanks. Table 1.1 shows a review of studies that used a CFD simulation to analyze atmospheric and pressurized LNG storage tanks.

**Table 1.1. A review of studies on the thermal performance of LNG storage tanks by using the CFD simulation.**

Reference	Scope	Approach	Findings
Shi et al. [29], 1993	Studied the thermal stratification and the rollover effect in an LNG tank numerically and verified the results with an experimental flow visualization	<ul style="list-style-type: none"> <li>• Constant heat flux on the bottom and side walls of the tank</li> <li>• Fixed LNG level</li> <li>• Neglected the mass change due to the surface evaporation.</li> </ul>	<ul style="list-style-type: none"> <li>• Comparing the numerical and experimental visualization indicated that increasing the base-to-side heat flux ratio likely caused a stronger mixing and more severe rollover effect.</li> </ul>
Khelifi et al. [30], 2010	Investigated the evaporation of LNG inside a cylindrical cavity	<ul style="list-style-type: none"> <li>• 2D axisymmetric CFD simulation of a cylindrical cavity</li> <li>• Adiabatic bottom wall</li> <li>• Uniform heat flux on the side walls</li> </ul>	<ul style="list-style-type: none"> <li>• The minimum and maximum evaporation heat fluxes at the vapor-liquid interface were located at the center and near the sidewalls, respectively.</li> <li>• The evaporation heat flux increased by increasing the</li> </ul>

Reference	Scope	Approach	Findings
		<ul style="list-style-type: none"> <li>• Laminar natural convection heat transfer</li> </ul>	Rayleigh number and the cavity height-to-diameter ratio.
Roh et al. [31], 2012	Calculated the BOG generation rate in an atmospheric LNG tank	<ul style="list-style-type: none"> <li>• Fixed LNG level</li> <li>• Constant temperature at the vapor-liquid interface</li> </ul>	<ul style="list-style-type: none"> <li>• The heat transfer rate from the environment to the LNG mainly contributed to the BOG generation rather than the heat transfer from the vapor phase to the LNG.</li> <li>• The heat transfer rate from the environment to the LNG had a linear relationship with the external convection heat transfer coefficient.</li> <li>• The model was applicable to LNG storage tanks with a minor change in its pressure.</li> </ul>
Roh et al. [32], 2012	Studied the transient natural convection in a pressurized LNG storage tank	<ul style="list-style-type: none"> <li>• Used Ansys Fluent software</li> <li>• Only considered the liquid phase</li> <li>• Pressurized the tank up to 140 kPa</li> </ul>	<ul style="list-style-type: none"> <li>• The BOG generation rate decreased by increasing the tank pressure and size.</li> </ul>
Miana et al. [33], 2015	Simulated 2D and 3D storage tanks of LNG carriers	<ul style="list-style-type: none"> <li>• Used Ansys Fluent software</li> <li>• Took one week of computation time for the 3D LNG storage tank</li> </ul>	<ul style="list-style-type: none"> <li>• Increasing the insulation thickness from 270 mm to 400 mm decreased the heat transfer rate to the LNG and average BOG generation rate by up to 67% and 30%, respectively.</li> <li>• The thicker insulation decreased the capacity of the storage tank by 2.2%.</li> </ul>
Choi et al. [34], 2017	Studied the thermal stratification in a 4.9-m <sup>3</sup> cryogenic tank	<ul style="list-style-type: none"> <li>• Used Ansys Fluent software</li> </ul>	<ul style="list-style-type: none"> <li>• The BOG generation rate increased by increasing the heat transfer rate to the tank and decreasing the LNG capacity in the tank or LNG filling level.</li> <li>• Under a constant heat transfer rate to the tank, the low filling level accelerated the development of thermal</li> </ul>

Reference	Scope	Approach	Findings
			stratified layers near the vapor-liquid interface.
Saleem et al. [35], 2018	Developed a 2D CFD model of an LNG storage tank	<ul style="list-style-type: none"> <li>• Used Ansys Fluent software</li> <li>• Used high-power computation facilities</li> <li>• Took 118 hours of computation to simulate the tank behaviour for 40 hours.</li> </ul>	<ul style="list-style-type: none"> <li>• Took about 20 hours to have a proper mixing in the LNG and reach a steady-state BOG generation rate in the tank.</li> <li>• The hydrostatic pressure in the LNG storage tank did not have a significant effect on the steady-state BOG generation rate.</li> </ul>
Ovidi et al. [36], 2018	Established a CFD model of a 100-m <sup>3</sup> vertical cylindrical tank in an LNG refueling station	<ul style="list-style-type: none"> <li>• Used Ansys Fluent software</li> <li>• Studied the dynamic thermal behaviour of the LNG storage tank under well-insulation and damaged insulation (loss of vacuum) conditions.</li> <li>• Solved the numerical domain by using a 16-node parallel computing</li> <li>• Took 1,800 hours (75 days) to simulate the thermal behaviour of the tank for 2 hours.</li> </ul>	<ul style="list-style-type: none"> <li>• The accidental loss of vacuum in the LNG storage tank significantly increased the self-pressurization of the tanks.</li> </ul>

Reviewing the literature summarized in Table 1.1 indicates that CFD simulation can provide a detailed understanding of heat and mass transfer inside LNG storage tanks. However, the long computation time and the complex two-phase characteristics of the LNG limit its applications. For example, the computation time in Ref. [36] was 1,800 hours (75 days) to simulate the thermal behaviour of the tank for 2 hours. Studying the LNG behaviour and thermal performance of storage tanks, which hold LNG for several days in refueling stations and onboard vessels, or for several

months in LNG peak shaving plants and LNG carriers, is beyond the capabilities of the CFD simulations.

Another approach to overcome the limitations of the CFD simulations is to use equilibrium thermodynamic modelling. This method considers LNG storage tanks with vapor and liquid phases in the thermal equilibrium state. Magliore et al. [20] used equilibrium thermodynamic modelling to investigate the LNG weathering in atmospheric storage tanks. Their results showed that increasing the amount of nitrogen in the LNG mixture decreased the BOG generation rate, and changing in the ambient temperature by 1°C changed the BOG generation rate by 0.2%. Sharafian et al. [37] analyzed the thermal performance of LNG storage tanks in refueling stations. Their results showed that the tank holding time increased by decreasing the ambient temperature, increasing the tank volume, and using insulation materials with low thermal conductivity. Miana et al. [38] developed an equilibrium thermodynamic model and used four methods to estimate the BOG generation rates, namely, constant and variable evaporation rates, and heat flows calculated during loading and unloading processes. Using these four methods, Miana et al. [38] predicted the LNG weathering in LNG carriers. Their results showed that the constant and variable evaporation rates led to the more accurate prediction of the LNG weathering at a destination. Comparing the numerical and experimental data to predict the LNG weathering showed that the average error between the two sets of data was minimized by increasing the voyage length and ship storage capacity [38]. These two parameters could likely set the condition for liquid and vapor phases to reach the thermal equilibrium state. Therefore, the results of the equilibrium thermodynamic modelling became more accurate [38]. Khan et al. [39] calculated the BOG generation rate in an LNG regasification terminal by using Aspen HYSYS Dynamics software. Their results indicated

that using an LNG storage tank with the height-to-diameter ratio of one minimized the BOG generation rate.

Equilibrium thermodynamic modelling provides information on the performance of LNG storage tanks (pressure, temperature, BOG generation rate, etc.) with a short computation time (in the order of few minutes to several hours depending on the complexity of the storage tank, operating conditions, etc.). However, this model provides identical temperature and pressure for the liquid and vapor phases, and is not capable of predicting the thermal stratification in LNG storage tanks. Also, under dynamic operating conditions, such as a sudden vapor injection to or removal from the tank, the equilibrium thermodynamic models fail to predict the dynamic behaviour of the storage tank. Moreover, equilibrium thermodynamic modelling cannot predict the thermal stratification and the rollover effect in LNG storage tanks.

Non-equilibrium thermodynamic modelling is a complementary solution to tackle the limitations of equilibrium thermodynamic modelling. Non-equilibrium thermodynamic modelling considers the liquid and vapor phases separately. Therefore, the heat and mass transfer interactions between the liquid and vapor phases happen through a vapor-liquid interface. Effendy et al. [40] studied an atmospheric LNG storage tank of a regasification terminal using a non-equilibrium thermodynamic model. Their numerical results showed that during 15 days of operation, the liquid phase temperature remained constant, while the vapor phase temperature increased by about 15°C. Migliore et al. [41] developed a non-equilibrium thermodynamic model to predict the LNG weathering in atmospheric storage tanks. Their numerical results showed that the vapor temperature maintained about 8°C higher than the boiling temperature of LNG during the course

of a year. Also, the BOG generation rate calculated by their non-equilibrium thermodynamic model decreased by 25% compared with the equilibrium thermodynamic model reported in their previous study (Ref. [20]).

Krikkis [42] used the non-equilibrium thermodynamic modelling to calculate the LNG weathering during ship transportation and compared the results with the experimental data. Krikkis' experimental measurements showed that the LNG temperature in atmospheric storage tanks did not change significantly, while the vapor phase temperature varied from  $-143^{\circ}\text{C}$  to  $-72^{\circ}\text{C}$ . Comparing the results of the non-equilibrium thermodynamic modelling and the experimental data of a laden voyage showed that the modelling results predicted the BOG generation rate with good accuracy in comparison with the measured amount of vapor removed from the tank. Qu et al. [43] used a non-equilibrium thermodynamic modelling to study the BOG generation rate in a  $160,000\text{-m}^3$  LNG ship tank during the laden voyage and ballast phase. The average daily BOG generation rate was about 0.14%. For the self-pressurization, the steep pressurization occurred at the initial phase, while the saturation temperature was almost constant. Qu et al. [43] showed that using the tank pressure and sea conditions as the input parameters, their model accurately predicted the vapor temperature in the LNG tank and the average daily BOG generation rate during the laden voyage and ballast phase.

In Refs. [40–42], the researchers assumed a constant heat transfer convection coefficient and an identical temperature for the tank walls in contact with liquid and vapor phases. Also, they neglected the effect of the thermal capacity of the tank walls, which affect the amount of heat transfer rate from the environment to the LNG inside the tank as shown by Sharafian et al. [37].

However, the non-equilibrium thermodynamic models discussed above cannot predict the thermal stratification in the cryogenic tanks because they only solved the bulk temperatures of the liquid and vapor phases. To calculate the temperature gradient in the liquid and vapor phases, analytical and lumped-parameter models based on the non-equilibrium thermodynamic concept can be developed. The lumped-parameter model establishes several cells in the liquid and vapor phases, respectively. A review of the analytical and lumped-parameter models is shown in Table 1.2.

**Table 1.2. A review of analytical and lumped-parameter models to predict the thermal stratification in cryogenic storage tanks.**

Reference	Scope	Approach	Results
Bailey et al. [44], 1964	Analytical and experimental research on liquid thermal stratification in a liquid hydrogen tank	<ul style="list-style-type: none"> <li>Calculated the heat transfer between the hot upper layer and cold lower layer to obtain the thermal stratification growth rate without calculating the boundary layer equations</li> </ul>	<ul style="list-style-type: none"> <li>The stratification was not affected by the liquid oscillation, sloshing, or outflow</li> <li>The simple analytical method predicted the trend of the thermal stratification</li> </ul>
Chin et al. [45], 1965	Analytical and experimental study on the liquid thermal stratification in a liquid hydrogen tank	<ul style="list-style-type: none"> <li>Established the thermal stratification growth model based on the boundary layer theory</li> <li>Assumed no boundary velocity profile in the thermal stratified layer</li> <li>Analyzed the thermal stratification in the tank under uniform bottom and side walls heat flux rates and asymmetric</li> </ul>	<ul style="list-style-type: none"> <li>Under asymmetric side wall heating, experimental and analytical results showed that the temperature gradient in the radial direction was zero</li> <li>The energy integral across the entire thermal stratified layer was independent of the liquid height to tank diameter aspect ratio with a modified Grashof number ranging from <math>10^8</math> to <math>10^{15}</math></li> <li>The results based on a boiling free-convection boundary layer and boiling</li> </ul>

Reference	Scope	Approach	Results
		side wall heating conditions	convection boundary layer could predict the experimental data
Hurd et al. [46], 1966	Analytical and experimental study of the thermal stratification formation in the liquid and vapor domains	<ul style="list-style-type: none"> <li>Established the thermal stratification layers in the vapor and liquid domains</li> <li>Calculated the energy balance at the vapor-liquid interface to determine the evaporation rate</li> <li>Considered the tank expansion due to the pressure rise</li> </ul>	<ul style="list-style-type: none"> <li>The results of the vapor-liquid coupling model and nucleate boiling in the liquid free-convection boundary layer predicted the experimental data</li> <li>Correlations for the enthalpy of vapor and liquid were obtained based on the experimental data</li> </ul>
Arnett et al. [47], 1972	Analytical solution for the liquid thermal stratification in a liquid hydrogen tank	<ul style="list-style-type: none"> <li>Considered the boundary layer equations</li> <li>Assumed the liquid energy profile in the axial direction had an exponential form</li> <li>Calculated the vapor pressure based on the vapor-liquid interface temperature at the equilibrium state</li> </ul>	<ul style="list-style-type: none"> <li>Assuming a uniform saturated temperature as the initial condition for the vapor phase was not a good approximation</li> <li>The trend of pressure rise was not sensitive to the location of maximum heat flux, and was independent of the tank size as long as the amount of total heat transfer remains constant</li> </ul>
Winter et al. [48], 1968	Analytical and experimental research on the liquid thermal stratification in a water tank	<ul style="list-style-type: none"> <li>Calculated the boundary layer equations</li> <li>Established the differential equations for the mass and energy in the thermal stratification zone to obtain the stratified layer growth rate</li> </ul>	<ul style="list-style-type: none"> <li>The analytical model predicted the stratification growth rate but over-predicted the vapor-liquid interface temperature</li> <li>The dimensionless results showed that the stratification process was influenced by the properties of the fluid and tank geometrical parameters</li> </ul>

Reference	Scope	Approach	Results
		<ul style="list-style-type: none"> <li>Considered the upward mass flow rate in the thermal stratified zone</li> </ul>	
Gursu et al. [49,50], 1993	Analytical solution for the liquid thermal stratification in a hydrogen tank	<ul style="list-style-type: none"> <li>Established a homogenous model and a thermal stratification model to predict pressure rise</li> <li>In the homogeneous model, two methods were employed. The first method assumed that the entire tank (liquid and vapor) had a unique temperature. The second method assumed that the heat transfer from the sidewall only caused the evaporation of the liquid without affecting the liquid temperature</li> <li>Calculated the boundary layer equations. Energy profile in the axial direction was assumed that it had an exponential form in the thermal stratification model.</li> </ul>	<ul style="list-style-type: none"> <li>The thermal stratification model had better accuracy in predicting the pressure rise in a self-pressurized tank than the homogenous model</li> </ul>
Seo et al. [51], 2010	Experimental research and numerical modelling of a self-pressurized nitrogen tank	<ul style="list-style-type: none"> <li>Developed a thermal diffusion model and an equilibrium thermodynamic model</li> <li>Deployed the one-dimensional thermal</li> </ul>	<ul style="list-style-type: none"> <li>The equilibrium thermodynamic model could predict the pressure rise when the tank undergoes the transient condition</li> <li>The thermal diffusion model could predict the</li> </ul>

Reference	Scope	Approach	Results
		<p>conduction equation in the vapor and liquid domains</p> <ul style="list-style-type: none"> <li>Calculated the pressure based on the average temperature and density of vapor phase by using REFPROP 7.0 software</li> </ul>	<p>pressurization rate after 10 mins except for the initial period</p>
Daigle et al. [52], 2013	Multilayer model to calculate the thermal stratification in a helium and hydrogen mixture tank under various gravities	<ul style="list-style-type: none"> <li>Developed a multilayer model to predict the thermal stratification</li> <li>Calculated the upward boundary flow along the tank wall</li> <li>Adopted the ideal gas equation of state to calculate the vapor pressure</li> <li>Considered the gravity influence on the thermal stratification</li> </ul>	<ul style="list-style-type: none"> <li>The multilayer lumped-parameter could solve the thermal stratification compared with the high cost CFD method</li> <li>The temperature wave caused by the venting could be predicted by this model</li> <li>The increased gravity mainly fortified the heat exchange between the tank walls and the cryogenic fuel content.</li> </ul>
Joseph et al. [53], 2016	Transient two-phase thermodynamic lumped-parameter model employed to calculate the thermal stratification in a liquid hydrogen tank via SINDA/FLUINT software	<ul style="list-style-type: none"> <li>Established three zones (core conduction zone, return flow zone, and boundary flow zone) in the liquid domain.</li> <li>Calculated the vertical boundary layer equations in the liquid domain</li> <li>Used the compressibility factor from NIST data to obtain the real fluid state</li> </ul>	<ul style="list-style-type: none"> <li>The thinner insulation layer led to a higher pressure rise in the tank, and a higher stratified mass due to the larger heat leak.</li> <li>The temperature of the tank outer walls was affected by the ambient environment, such as solar flux.</li> </ul>

Reference	Scope	Approach	Results
		<ul style="list-style-type: none"> <li>Solved the tank wall temperature via three-dimensional heat transfer conduction equations</li> </ul>	
Kang et al. [54], 2018	Experimental and numerical study of the liquid thermal stratification in a pressurized liquid nitrogen tank	<ul style="list-style-type: none"> <li>Assumed the liquid domain as a solid zone and calculated the liquid temperature profile by the Finite Element Method (FEM).</li> </ul>	<ul style="list-style-type: none"> <li>Higher thermal aspect ratio (sidewall to the total heat transfer to the tank) accelerated the thermal stratification</li> </ul>
Duan et al. [55], 2021	Moving-boundary based a dynamic model deployed to calculate the thermal stratification in an LNG storage tank	<ul style="list-style-type: none"> <li>Solved the boundary layer equations</li> <li>Set up the stratification layer and bulk liquid control volume in the LNG domain</li> <li>Established one control volume to predict the vapor thermal performance</li> </ul>	<ul style="list-style-type: none"> <li>The lumped-parameter model with moving boundary layer could predict the thermal stratification, and pressure rise</li> <li>The thermal response of the liquid phase had three stages under the external heat flux: The boundary layer initially formed; the stratified layer developed from the vapor-liquid interface; fully-developed thermal stratification with steady temperature gradient formed in the axial direction</li> </ul>

Based on the literature review shown in Table 1.2, analytical methods appeared easy to use. They simulate the energy profile along the tank walls with an exponential function based on experimental observations. However, these methods cannot predict the heat exchange during the mixing of two stratified layers.

Lumped-parameter models numerically solve the temperature profile without using any energy profiles. These models consider the boundary flow along the tank vertical walls to reflect the convective heat transfer inside the liquid and vapor phases. In this work, a lumped-parameter model is used to develop a non-equilibrium multilayer thermodynamic model in the liquid and vapor phases.

### **1.3 Rollover phenomenon and pertinent literature review**

The thermal stratification in cryogenic storage tanks is caused by the natural convection or loading fresh cryogenic liquid with different composition and density from that left in the tank prior to loading. Mixing two different LNG products in the same storage tank at LNG terminal stations is a common practice. This could occur when the LNG level in the storage tank is low, and a new stock of LNG is loaded. In this case, the residual LNG (also called heel) and the new load of LNG (also called cargo) have different temperatures, densities, and compositions (as shown in Figure 1.2(b)). If the cargo with a higher density is loaded from the bottom of the LNG storage tank, the heel with a lower density remains on top of the cargo layer. This causes thermal stratification in the LNG storage tank. In the beginning, these thermally stratified layers are stable. However, the heat and mass transfer between the heel and cargo layers occur over time due to the temperature and composition differences. If the storage tank remains in this condition without enough safety measures, the density difference between the heel and cargo is finally equalized, making the heel-cargo interface unstable. Under this condition, the sudden mixing of the heel and cargo layers generates a significant amount of BOG due to the release of the heat accumulated in the cargo layer over time. This BOG generation increases the tank pressure abruptly, and in some circumstances, this can cause the failure of the tank structure, e.g., the La Spezia incident in 1971

[26]. In SNAM LNG Terminal located in La Spezia, Italy, an LNG storage tank, which initially stored around 9,539 m<sup>3</sup> LNG heel, received around 33,387 m<sup>3</sup> LNG cargo from LNG ship *Esso Brega*. After 18 hours, the tank pressure suddenly rose to 6.96 kPa (gauge pressure), exceeding the tank designed safety pressure of about 4.90 kPa and caused the failure of the tank structure. This phenomenon is identified as “rollover” [26,27]. To prevent any catastrophe, the common practice in cryogenic storage facilities is to destroy the thermal stratification. The below contents show some common methods to prevent rollover from occurring in the industry [56]:

- 1) If the density of the incoming LNG cargo is lighter than the LNG heel in the tank, a bottom filling operation will be chosen to complete the mixing of the two LNG layers.
- 2) If the density of the incoming LNG cargo is heavier than the LNG heel in the tank, a top filling operation will prevent the stratification and lower the risk of the rollover.
- 3) If the thermal stratification is observed in the LNG storage tanks, the following methods may be used to destroy the thermal stratification.
  - a. Transfer the LNG from the tank to another tank.
  - b. Circulate LNG in the tank by mixing devices, such as pumps inside the tank or jet mixing nozzle.

However, developing a model to predict the possible rollover occurrence time is of great importance. Table 1.3 shows a list of multilayer thermodynamic and CFD models to study the rollover phenomenon.

**Table 1.3. A review of studies on the rollover in cryogenic storage tanks.**

<b>Reference</b>	<b>Scope</b>	<b>Approach</b>	<b>Results</b>
Sarsten [26], 1972	Described the La Spezia rollover incident in 1971	<ul style="list-style-type: none"> <li>Reported the details (composition, temperature, pressure, etc.) of LNG in the La Spezia incident</li> </ul>	<ul style="list-style-type: none"> <li>Estimated the heat flux based on the BOG generation rate</li> <li>The numerical results of analyzing the density showed that the rollover occurred in 120 hours</li> </ul>
Chatterjee et al. [28], 1972	Established a multilayer model to calculate the BOG generation rate in three cases: fast fill from the bottom with large and small density differences between the top and bottom layers, and slow fill from the top with large density differences between the top and bottom layers	<ul style="list-style-type: none"> <li>Established heat and mass transfer equations for the heel and cargo layers</li> <li>Mass transfer equations were calculated based on the correlations from the experimental data of salt-water solution</li> </ul>	<ul style="list-style-type: none"> <li>An increase in the height of the bottom layer, and fast filling rate resulted in a high peak vaporization rate</li> <li>The peak vaporization period prolonged if the density difference between the heel and cargo layers increased</li> <li>A warmer bottom layer mixed quicker than a colder bottom layer if the density difference was the same</li> </ul>
Germeles [57], 1975	Established a multilayer model to simulate the La Spezia incident	<ul style="list-style-type: none"> <li>Adopted thermohaline correlations to calculate double-diffusive convection between the heel and cargo layers</li> </ul>	<ul style="list-style-type: none"> <li>The La Spezia rollover incident was predicted to happen after 34 hours</li> <li>Defined some parameters related to the geometry and the heat flux rate to estimate the rollover time quickly</li> </ul>
Heestand et al. [27], 1983	Established a multilayer model to simulate the La Spezia incident	<ul style="list-style-type: none"> <li>Considered the Rayleigh flow at the vapor-liquid interface</li> <li>The calculation of the mass transfer coefficient was based</li> </ul>	<ul style="list-style-type: none"> <li>Predicted the La Spezia incident rollover time ranging from 20.4 hours to 33.1 hours by using various correlations for the heat</li> </ul>

Reference	Scope	Approach	Results
		on the Reynolds analogy	transfer between the heel and cargo layers
Shi et al. [29], 1993	Developed a two-dimensional CFD model to simulate the mixing and rollover of two stratified layers (liquid nitrogen and liquid nitrogen with a small amount of liquid oxygen)	<ul style="list-style-type: none"> <li>• Studied the liquid domain only</li> <li>• Neglected the evaporation</li> </ul>	<ul style="list-style-type: none"> <li>• Large heat flux from the bottom of the liquid layer resulted in a stronger rollover</li> </ul>
Bates et al. [58], 1997	Established a multilayer model to simulate three experiments conducted at Nates cryogenic testing station in France	<ul style="list-style-type: none"> <li>• Analyzed the rollover in three stages: Stationary interface, migrating interface, and rollover occurrence</li> <li>• Used the model developed by Heestand et al. [27] to simulate Stage 1</li> </ul>	<ul style="list-style-type: none"> <li>• Critical point stability number was more related to the accuracy than the transfer parameters at the heel-cargo interface at Stage 1</li> <li>• The temperature trend of the lower layer remained unchanged at Stage 2</li> </ul>
Zimmerman et al. [59], 2007	Employed mathematical modelling and non-dimensional analysis to study the rollover instability	<ul style="list-style-type: none"> <li>• Modeled the double diffusion in a stable stratification</li> <li>• Established a FEM model to simulate the rollover</li> </ul>	<ul style="list-style-type: none"> <li>• Defined a stability parameter to reflect the rollover stability</li> <li>• The pre-rollover flow was laminar, and mass and heat transfers were time-dependent</li> <li>• The eddy flow in the tank corner was a driver for rollover</li> <li>• Velocity, heat flux, and Shannon entropy reached their maximum when the rollover occurred</li> </ul>
Li et al. [60], 2015	Developed a two-dimensional	<ul style="list-style-type: none"> <li>• Established two stratified liquid layers</li> </ul>	<ul style="list-style-type: none"> <li>• Rollover strength was related to the initial density difference</li> </ul>

Reference	Scope	Approach	Results
	CFD model to simulate the rollover in LNG tanks	<ul style="list-style-type: none"> <li>• Did not consider the energy equation</li> </ul>	<ul style="list-style-type: none"> <li>• Found that the threshold of initial density differences for 5,000, 30,000, and 160,000 m<sup>3</sup> LNG storage tanks were 7, 5, and 3 kg/m<sup>3</sup> to prevent rollover, respectively</li> </ul>
Arjomandnia [61], 2015	Developed a multilayer model to simulate the rollover in LNG tanks	<ul style="list-style-type: none"> <li>• Solved energy equation, and mass transfer equations in heel, cargo, and vapor domains</li> <li>• Adopted two convective mass transfer mechanisms to calculate the mass transfer in two distinct stages of rollover</li> </ul>	<ul style="list-style-type: none"> <li>• The model could model the La Spezia incident</li> <li>• A criterion was identified to indicate the rate of auto-stratification</li> <li>• Nitrogen content above 1% did not affect the rollover occurrence directly, but increased the BOG generation rate and operating cost</li> </ul>
Hubert et al. [62], 2019	Developed a three-dimensional CFD model to simulate the rollover in LNG tanks	<ul style="list-style-type: none"> <li>• Established two stratified liquid layers</li> <li>• Considered the heat flux at the vapor-liquid interface due to the evaporation</li> </ul>	<ul style="list-style-type: none"> <li>• The three-dimensional CFD model predicted the La Spezia incident</li> <li>• The rapid mixing was caused by the two stratified layers interface moving downward</li> </ul>

A review of the models listed in Table 1.3 indicates that the multilayer models only considered the rollover effect due to the temperature difference between the heel and cargo layers in the liquid domain, and did not consider the thermal stratification caused by natural convection. Although the CFD models provided a detailed profile of the temperature distribution in the liquid phase, the computation time was long. In the CFD model developed by Hubert et al. [62], 28-core parallel computation was used. The CFD simulations predicted that the rollover occurred in 40-60 hours. However, the CFD computation time took 200-440 hours, much longer than the actual rollover

time. This illustrates that the CFD simulations are not fast and efficient methods to predict the possible rollover start time based on the input parameters of a real LNG storage tank.

#### **1.4 Research objectives**

In the literature review of the non-equilibrium thermodynamic model, most studies were developed by using a constant heat transfer convection coefficient and constant wall temperature assumptions. Also, the thermal capacity of the tank wall, which affects the amount of the heat transfer rate from the environment to the LNG inside the tank, is widely neglected. In this work, a new non-equilibrium thermodynamic model based on the concept of a resistance-capacitance network is developed to assess the performance of LNG storage tanks. To accurately calculate the temperature and pressure of the LNG inside the tank, the heat transfer convection coefficients on the tank walls are calculated based on empirical correlations and tank geometry. Also, the effects of the thermal capacity of the tank wall, insulation, and tank positioning (vertical vs horizontal tanks) are included in the model. This non-equilibrium thermodynamic model provides a robust, easy-to-implement tool to design and predict the pressure rise and bulk temperatures of vapor and liquid phases in LNG storage tanks in refueling stations, LNG-fueled vessels, LNG peak shaving and storage facilities, and LNG carriers.

To obtain the detailed temperature distribution in the liquid and vapor phases inside LNG storage tanks in a short time and overcome the limitation of the CFD method, this work introduces a new non-equilibrium multilayer thermodynamic model in the vapor and liquid domains and considers the natural convection boundary flow along the tank walls to accommodate the limitations of models discussed in Table 1.2 and Table 1.3. The present model uses an adaptive mesh to

accommodate the changes in the LNG level in the tank over time due to heat transfer, evaporation, and condensation. In addition, to quickly evaluate the rollover phenomenon, the mass transfer mechanism is incorporated in the non-equilibrium multilayer thermodynamic model. The accuracy of the multilayers model is compared against the thermal stratification and rollover via experimental data. This non-equilibrium multilayer thermodynamic model will be used as an efficient tool to optimize the thermal stratification of the LNG storage tanks and estimate the rollover occurrence time. All models are developed in Microsoft Visual C++ language.

### **1.5 Technical road map**

Figure 1.3 shows the scope of this Ph.D. research project. The non-equilibrium thermodynamic model can be used to study the thermal performance of stationary vertical and horizontal tanks, and the dynamic performance of storage tanks in LNG refueling stations. Also, the non-equilibrium multilayer thermodynamic model can be applied to study the thermal stratification and rollover phenomena in LNG storage tanks.

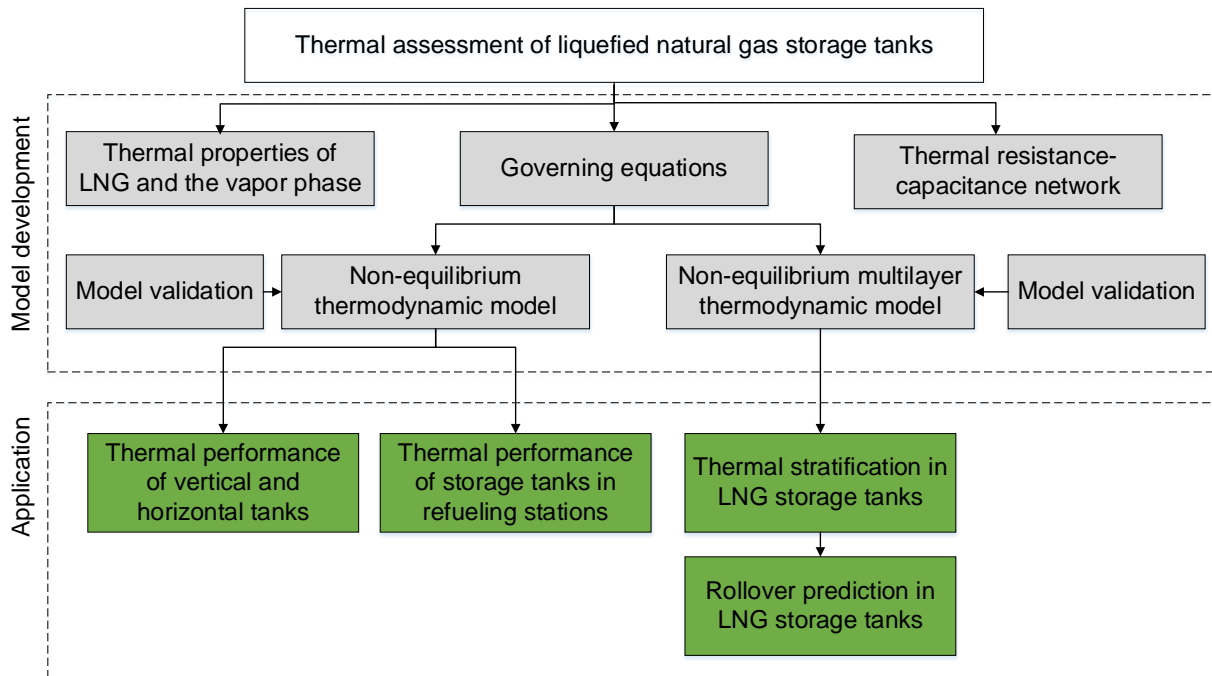


**Figure 1.3. Scope of the Ph.D. research project and applications.**

## **Chapter 2: Development of Non-equilibrium and Non-equilibrium Multilayer Thermodynamic Models**

In LNG refueling stations and LNG-fueled marine vessels, LNG is stored in pressurized vacuum-jacketed storage tanks. In large LNG peak shaving and storage facilities, LNG is stored in well-insulated concrete tanks at near atmospheric pressure. In both applications, the heat transfer from the surroundings causes the evaporation of LNG and increases the pressure in the storage tanks. Due to the large volumetric heat capacity difference between the LNG and gaseous natural gas (e.g.,  $1470.28 \text{ kJ/m}^3 \cdot \text{K}$  for the LNG and  $4.03 \text{ kJ/m}^3 \cdot \text{K}$  for the gaseous natural gas at  $-162^\circ\text{C}$  and 1 atm) and underutilization of LNG, the thermal stratification can happen inside the tanks. To simulate the thermal performance of the storage tanks, this chapter presents the development of non-equilibrium and non-equilibrium multilayer thermodynamic models.

In the non-equilibrium thermodynamic model, two control volumes are established in the vapor and liquid phases. This model can estimate the pressure rise and bulk temperatures of the vapor and liquid phases with a short computation time. Also, this model calculates the convective heat transfer coefficients along the tank walls and predicts the tank wall temperature. In the non-equilibrium multilayer thermodynamic model, several control volumes are constructed in the vapor and liquid phases to capture the temperature gradient in the LNG storage tanks. This model computes the mass flow within the boundary layers along the tank vertical walls. Also, the mass transfer mechanism is modelled between the heel and cargo layers to predict the rollover

occurrence time. Although the computation cost of this model is higher than the non-equilibrium thermodynamic model due to the complexities, this model is still much more time-efficient to predict the thermal stratification in LNG storage tanks compared with CFD models.

## 2.1 Non-equilibrium thermodynamic model

In the non-equilibrium thermodynamic model, the entire LNG storage tank is divided into three segments: vapor phase, liquid phase, and tank walls as shown in Figure 2.1. The vapor-liquid interface is part of the liquid and vapor phases. The heat from the environment passes through the tank wall and transfers to the vapor and liquid phases. Therefore, the vapor temperature,  $T_v$ , and the liquid temperature,  $T_l$ , increase. Simultaneously, the evaporation or condensation occurs at the vapor-liquid interface.

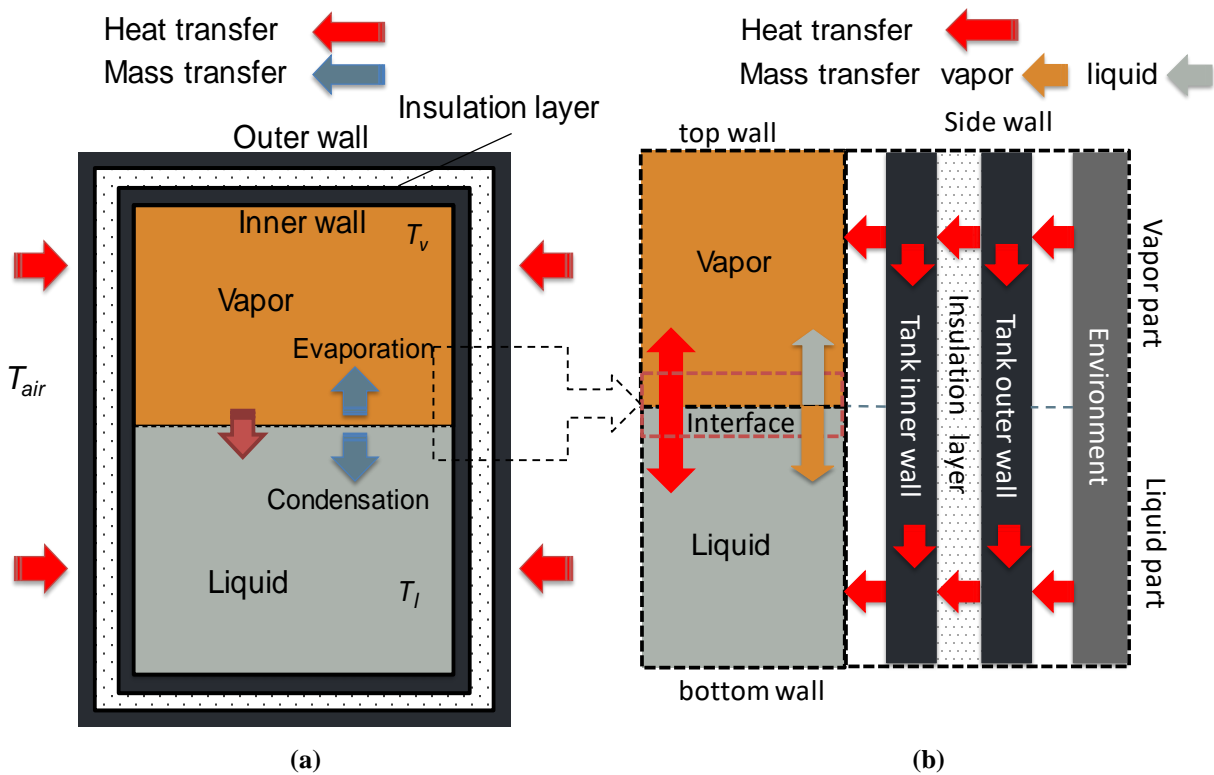


Figure 2.1. (a) Schematic of heat and mass transfer in an LNG storage tank and (b) the main segments of the LNG storage tank considered in the non-equilibrium thermodynamic model.

## 2.1.1 Governing equations in the non-equilibrium thermodynamic model

### 2.1.1.1 Conservation of mass in the liquid and vapor phases

The changes in the mass of liquid and vapor phases due to the evaporation and condensation at the vapor-liquid interface can be calculated as follows:

$$\dot{m}_{lv} = (\dot{m}_e''' - \dot{m}_c''')\mathcal{V}_{interface} \quad (2-1)$$

where,  $\mathcal{V}_{interface}$  represents the volumes of liquid and vapor phases contributing to the evaporation and condensation processes, respectively, and is calculated by Eq.(2-2).

$$\mathcal{V}_{interface} = A_{interface} \cdot \delta \quad (2-2)$$

$A_{interface}$  and  $\delta$  in Eq. (2-2) are the area of the vapor-liquid interface ( $m^2$ ) and the thickness of the liquid and vapor phases affected (m) during the evaporation and condensation, respectively. In this study, the thickness of the layer  $\delta$  is set at 0.005 m based on the experimental work conducted by Beduz and Scurlock [63]. The experimental data show that the evaporation phenomenon does not affect the liquid temperature profile 0.005 m below the interface.

The Lee model [64] is applied to calculate the volumetric evaporation and condensation rates with respect to the bubble point,  $T_{bubble}$ , and dew point,  $T_{dew}$  at the vapor-liquid interface.  $T_{bubble}$  and  $T_{dew}$  are a function of species composition and pressure, and they are calculated from the vapor-liquid equilibrium (VLE) state.

If  $T_l > T_{bubble}$ , the evaporation occurs,

$$\dot{m}_e''' = f_e \cdot \rho_l \frac{T_l - T_{bubble}}{T_{bubble}} \quad (2-3)$$

and if  $T_v < T_{dew}$ , the condensation occurs,

$$\dot{m}_c''' = f_c \cdot \rho_v \frac{T_{dew} - T_v}{T_{dew}} \quad (2-4)$$

$f_e$  and  $f_c$  in Eqs. (2-3) and (2-4) represent the evaporation and condensation coefficients, respectively, and are determined based on the experimental data. The values of  $f_e$  and  $f_c$  can vary from  $10^{-3}$  to  $10^3$  1/s [35,65–67]. In this study, the values of  $f_e$  and  $f_c$  coefficients are varied from 0.001 to 1 for horizontal LNG and vertical liquid nitrogen storage tanks presented in Section 3.1.2 (model validation). The results show that the pressure rise in the tank is independent of these coefficients. A similar conclusion was reported in a CFD modelling of a cryogenic storage tank conducted by Kassemi and Kartuzova [67]. However, very high and low values of  $f_e$  and  $f_c$  lead to the numerical divergence and underestimating the pressure rise, respectively. The Lee model considers the evaporation and condensation at the interface under a quasi-thermal equilibrium state. Therefore, small values of  $f_e$  and  $f_c$  lead to the large saturation temperature difference at the interface [68] and exceed  $5^\circ\text{C}$ , which is the regime of pool boiling [69] and does not happen in LNG storage tanks under normal operating conditions. To maintain the saturation temperature difference of the liquid and vapor phases below  $3^\circ\text{C}$  [70], the  $f_e$  and  $f_c$  coefficients in the present study are set at 0.1.

Considering filling the tank,  $\dot{m}_{l,fill}$ , dispensing liquid from the tank,  $\dot{m}_{l,dis}$ , vapor release from the tank,  $\dot{m}_{v,rel}$ , and vapor injection to the tank,  $\dot{m}_{v,inj}$ , as well as mass transfer between the liquid and vapor phases, Eq.(2-1), the conservation of mass in the LNG storage tank can be expressed as,

$$\frac{d(m_l)}{dt} = \frac{d(\rho_l V_l)}{dt} = -\dot{m}_{lv} - \dot{m}_{l,dis} + \dot{m}_{l,fill} \quad (2-5)$$

$$\frac{d(m_v)}{dt} = \frac{d(\rho_v \forall_v)}{dt} = \dot{m}_{lv} - \dot{m}_{v,rel} + \dot{m}_{v,inj} \quad (2-6)$$

In addition, assuming a constant volume for the storage tank, the summation of changes in the volume of liquid and vapor phases as a function of time equals zero:

$$\frac{d(\forall_l + \forall_v)}{dt} = \frac{d(\forall_{tank})}{dt} = 0 \quad (2-7)$$

### 2.1.1.2 Conservation of energy in the liquid and vapor phases

Equations (2-8) and (2-9) give the heat balance in the liquid and vapor phases:

$$\begin{aligned} \frac{dH_l}{dt} = & \dot{Q}_{l,wall} + \dot{Q}_{vl} - \max[\dot{m}_{lv}, 0] \cdot h_v(T_{bubble}, P) - \min[\dot{m}_{lv}, 0] \cdot h_l(T_{dew}, P) \\ & - \dot{m}_{l,dis} \cdot h_l(T_{l,dis}, P) + \dot{m}_{l,fil} \cdot h_l(T_{l,fil}, P) + \forall_l \frac{dP}{dt} \end{aligned} \quad (2-8)$$

$$\begin{aligned} \frac{dH_v}{dt} = & \dot{Q}_{v,wall} - \dot{Q}_{vl} + \max[\dot{m}_{lv}, 0] \cdot h_v(T_{bubble}, P) + \min[\dot{m}_{lv}, 0] \cdot h_l(T_{dew}, P) \\ & - \dot{m}_{v,rel} \cdot h_v(T_{v,rel}, P) + \dot{m}_{v,inj} \cdot h_v(T_{v,inj}, P_{v,inj}) + \forall_v \frac{dP}{dt} \end{aligned} \quad (2-9)$$

where,  $H_l$  and  $H_v$  are the total enthalpy of liquid and vapor phases, respectively. In Eqs. (2-8) and (2-9),  $\dot{Q}_{l,wall}$  and  $\dot{Q}_{v,wall}$  are the heat transfer rate from the tank walls to the liquid and vapor phases, respectively.  $\dot{Q}_{vl}$  represents the natural convection heat transfer rate between the liquid and vapor phases at the interface.  $h_l$  and  $h_v$  denote the specific mass enthalpy of liquid and vapor phases at a given temperature,  $T$ , and pressure,  $P$ , respectively.  $\max[\dot{m}_{lv}, 0] \cdot h_v(T_{bubble}, P)$  represents the heat transfer rate due to the evaporation at the vapor-liquid interface ( $\dot{m}_{lv} > 0$ ).  $\min[\dot{m}_{lv}, 0] \cdot h_l(T_{dew}, P)$  represents the heat transfer rate due to the condensation at the vapor-liquid interface ( $\dot{m}_{lv} < 0$ ).  $\dot{m}_{l,fil} \cdot h_l(T_{l,fil}, P)$  represents the liquid enthalpy flow rate into the tank due to the liquid filling.  $\dot{m}_{l,dis} \cdot h_l(T_{l,dis}, P)$  represents the liquid enthalpy flow rate out from

the tank due to the liquid dispensing.  $\dot{m}_{v,inj} \cdot h_v(T_{v,inj}, P_{v,inj})$  represents the vapor enthalpy flow rate into the tank due to the vapor injection.  $\dot{m}_{v,rel} \cdot h_v(T_{v,rel}, P)$  represents the vapor enthalpy flow rate out from the tank due to the vapor release.

Using the finite difference discretization, Eqs. (2-8) and (2-9) can be expressed as:

$$\begin{aligned} \frac{H_l^{t+\Delta t} - H_l^t}{\Delta t} = & \dot{Q}_{l,wall} + \dot{Q}_{vl} - \max[\dot{m}_{lv}, 0] \cdot h_v(T_{bubble}, P) - \min[\dot{m}_{lv}, 0] \cdot h_l(T_{dew}, P) \\ & - \dot{m}_{l,dis} \cdot h_l(T_{l,dis}, P) + \dot{m}_{l,fil} \cdot h_l(T_{l,fil}, P) + \mathcal{V}_l^t \frac{P^t - P^{t-\Delta t}}{\Delta t} \end{aligned} \quad (2-10)$$

$$\begin{aligned} \frac{H_v^{t+\Delta t} - H_v^t}{\Delta t} = & \dot{Q}_{v,wall} - \dot{Q}_{vl} + \max[\dot{m}_{lv}, 0] \cdot h_v(T_{bubble}, P) + \min[\dot{m}_{lv}, 0] \cdot h_l(T_{dew}, P) \\ & - \dot{m}_{v,rel} \cdot h_v(T_{v,rel}, P) + \dot{m}_{v,inj} \cdot h_v(T_{v,inj}, P_{v,inj}) + \mathcal{V}_v^t \frac{P^t - P^{t-\Delta t}}{\Delta t} \end{aligned} \quad (2-11)$$

Therefore, one can calculate  $H_l^{t+\Delta t}$  and  $H_v^{t+\Delta t}$  at time step  $t+\Delta t$ . At time  $t$ , the total enthalpy of the liquid and vapor phases can be expressed as  $m_l^t h_l^t(T_l^t, P^t)$  and  $m_v^t h_v^t(T_v^t, P^t)$ , respectively. Similarly, the specific mass enthalpy of the liquid and vapor phases at  $t+\Delta t$  can be calculated from Eqs. (2-12) and (2-13):

$$h_l^{t+\Delta t} = \frac{H_l^{t+\Delta t}}{m_l^{t+\Delta t}} \quad (2-12)$$

$$h_v^{t+\Delta t} = \frac{H_v^{t+\Delta t}}{m_v^{t+\Delta t}} \quad (2-13)$$

Equations (2-14) and (2-15) give the temperatures of liquid and vapor phases at  $t+\Delta t$ :

$$\int_{T_l^t}^{T_l^{t+\Delta t}} c_{p,l}(T_l, P^t) dT = h_l^{t+\Delta t} - h_l^t \quad (2-14)$$

$$\int_{T_v^t}^{T_v^{t+\Delta t}} c_{p,v}(T_v, P^t) dT = h_v^{t+\Delta t} - h_v^t \quad (2-15)$$

$c_{p,l}(T_l, P^t)$ ,  $c_{p,v}(T_v, P^t)$  refer to the specific heat capacity of the liquid and real gas, respectively.

The pressure  $P^t$  at time  $t$  is employed to calculate  $c_{p,l}(T_l, P^t)$  and  $c_{p,v}(T_v, P^t)$  by using Peng-Robinson equation of state, which is discussed in Section 2.1.1.5.

To solve Eqs. (2-14) and (2-15), the Newton-Raphson method is used to find  $T_l^{t+\Delta t}$  and  $T_v^{t+\Delta t}$  from the liquid and vapor temperatures at the  $i^{th}$  iteration:

$$T_{l,i+1}^{t+\Delta t} = T_{l,i}^{t+\Delta t} - \frac{h_l(T_{l,i}^{t+\Delta t}, P^t) - h_l^{t+\Delta t}}{c_{p,l}(T_{l,i}^{t+\Delta t}, P^t)} \quad (2-16)$$

$$T_{v,i+1}^{t+\Delta t} = T_{v,i}^{t+\Delta t} - \frac{h_v(T_{v,i}^{t+\Delta t}, P^t) - h_v^{t+\Delta t}}{c_{p,v}(T_{v,i}^{t+\Delta t}, P^t)} \quad (2-17)$$

The initial values of  $T_l^{t+\Delta t}$  and  $T_v^{t+\Delta t}$  are given as,  $T_{l,0}^{t+\Delta t} = T_l^t$ ,  $T_{v,0}^{t+\Delta t} = T_v^t$ . The enthalpy of vapor phase  $h_v(T_{v,i}^{t+\Delta t}, P^t)$  and the enthalpy of liquid phase,  $h_l(T_{l,i}^{t+\Delta t}, P^t)$ , are calculated based on the Peng-Robinson equation of state, which is discussed in Section 2.1.1.5. Equations (2-16) and (2-17) converge when the absolute values of  $T_{l,i+1}^{t+\Delta t} - T_{l,i}^{t+\Delta t}$  and  $T_{v,i+1}^{t+\Delta t} - T_{v,i}^{t+\Delta t}$  reach at  $10^{-3}$  K.

### 2.1.1.3 Heat transfer rate through the tank wall

The details of the heat transfer from the environment to the liquid and vapor phases inside a vertical tank are shown in Figure 2.2. The heat transfer rate through the walls can be expressed by using an equivalent resistance-capacitance network [71], as shown in Figure 2.3. The parameters in the resistance-capacitance network are defined in Table A1 in Appendix A .

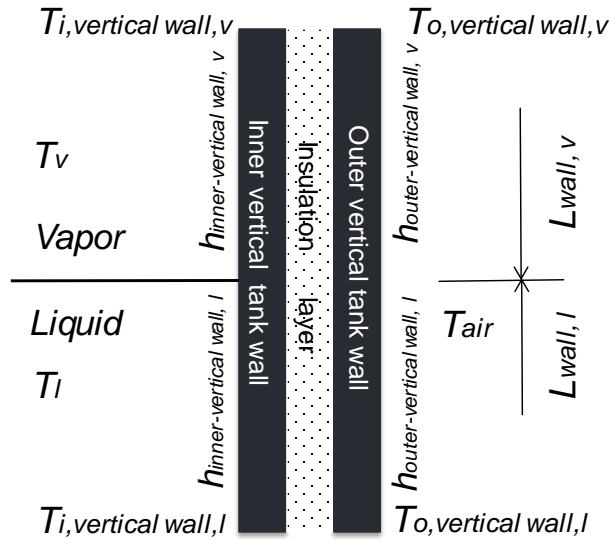


Figure 2.2. Details of the heat transfer from the environment to the liquid and vapor phases inside a vertical storage tank.

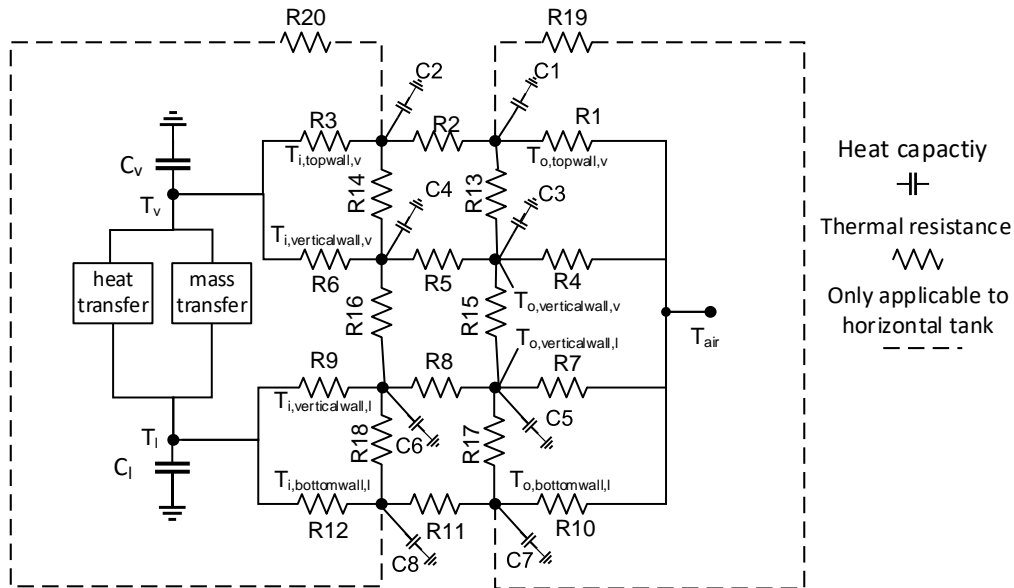


Figure 2.3. The thermal resistance-capacitance network for vertical and horizontal storage tanks. The dashed lines are only for the horizontal storage tanks.

The resistance-capacitance network is solved by using Kirchhoff's circuit law [71]. The outer vertical wall temperature of the vertical tank in contact with the liquid and vapor phases at time  $t+\Delta t$  can be explicitly calculated as,

$$T_{o,vertical\ wall,v}^{t+\Delta t} = \frac{\frac{T_{o,vertical\ wall,v}^t}{\Delta t} C_3 + \frac{T_{air}}{R_4} + \frac{T_{i,vertical\ wall,v}^{t+\Delta t}}{R_5} + \frac{T_{o,top\ wall,v}^t}{R_{13}} + \frac{T_{o,vertical\ wall,l}^t}{R_{15}}}{\frac{C_3}{\Delta t} + \frac{1}{R_4} + \frac{1}{R_5} + \frac{1}{R_{13}} + \frac{1}{R_{15}}} \quad (2-18)$$

$$T_{o,vertical\ wall,l}^{t+\Delta t} = \frac{\frac{T_{o,vertical\ wall,l}^t}{\Delta t} C_5 + \frac{T_{air}}{R_7} + \frac{T_{i,vertical\ wall,l}^{t+\Delta t}}{R_8} + \frac{T_{o,bottom\ wall,l}^t}{R_{17}} + \frac{T_{o,vertical\ wall,v}^t}{R_{15}}}{\frac{C_5}{\Delta t} + \frac{1}{R_7} + \frac{1}{R_8} + \frac{1}{R_{17}} + \frac{1}{R_{15}}} \quad (2-19)$$

Similarly, the inner vertical wall temperature of the vertical tank in contact with the liquid and vapor phases at time  $t+\Delta t$  can be calculated as,

$$T_{i,vertical\ wall,v}^{t+\Delta t} = \frac{\frac{T_{i,vertical\ wall,v}^t}{\Delta t} C_4 + \frac{T_{o,vertical\ wall,v}^{t+\Delta t}}{R_5} + \frac{T_v^t}{R_6} + \frac{T_{i,top\ wall,v}^t}{R_{14}} + \frac{T_{i,vertical\ wall,l}^t}{R_{16}}}{\frac{C_4}{\Delta t} + \frac{1}{R_5} + \frac{1}{R_6} + \frac{1}{R_{14}} + \frac{1}{R_{16}}} \quad (2-20)$$

$$T_{i,vertical\ wall,l}^{t+\Delta t} = \frac{\frac{T_{i,vertical\ wall,l}^t}{\Delta t} C_6 + \frac{T_{o,vertical\ wall,l}^{t+\Delta t}}{R_8} + \frac{T_l^t}{R_9} + \frac{T_{i,bottom\ wall,l}^t}{R_{18}} + \frac{T_{i,vertical\ wall,v}^t}{R_{16}}}{\frac{C_6}{\Delta t} + \frac{1}{R_8} + \frac{1}{R_9} + \frac{1}{R_{18}} + \frac{1}{R_{16}}} \quad (2-21)$$

Therefore, the heat transfer rates from the environment to the liquid and vapor phases in the vertical tank are calculated as,

$$\dot{Q}_{v,wall} = \frac{T_{i,top\ wall,v} - T_v}{R_3} + \frac{T_{i,vertical\ wall,v} - T_v}{R_6} \quad (2-22)$$

$$\dot{Q}_{l,wall} = \frac{T_{i,bottom\ wall,l} - T_l}{R_{12}} + \frac{T_{i,vertical\ wall,l} - T_l}{R_9} \quad (2-23)$$

The total heat transfer rate to the tank is the summation of the heat transfer rates to the liquid and vapor phases calculated from Eqs. (2-22) and (2-23). Similar calculations to Eqs. (2-18)-(2-23) for a horizontal tank can be applied to calculate the heat transfer rate to the tank. The overall heat transfer coefficients between the environment and the liquid and vapor phases are calculated as

$$U_v = \frac{\dot{Q}_{v,wall}}{(T_{air} - T_v)A_{inner\ wall,v}} \quad (2-24)$$

$$U_l = \frac{\dot{Q}_{l,wall}}{(T_{air} - T_l)A_{inner\ wall,l}} \quad (2-25)$$

#### 2.1.1.4 Heat transfer rate at the vapor-liquid interface

The natural convection heat transfer across the vapor-liquid interface due to the temperature gradient between the liquid and vapor phases is calculated by

$$\dot{Q}_{vl} = h_{vl,interface}(T_v - T_l)A_{interface} \quad (2-26)$$

where,

$$\frac{1}{h_{vl,interface}} = \frac{1}{h_{v,interface}} + \frac{1}{h_{l,interface}} \quad (2-27)$$

The convection heat transfer coefficients  $h_{v,interface}$  and  $h_{l,interface}$  at the vapor-liquid interface are calculated based on the empirical correlations of external free convection on a horizontal flat plate.

$$h_{v,interface} = \frac{k_v Nu}{L_{ref}} \quad (2-28)$$

where,  $k_v$  is the thermal conductivity of the vapor phase.  $L_{ref}$  is the characteristic length and is defined as

$$L_{ref} = \frac{A_{interface}}{\mathcal{P}_{interface}} = \frac{D_{inner}}{4} \quad (2-29)$$

where,  $A_{interface}$ ,  $\mathcal{P}_{interface}$ , and  $D_{inner}$  are the vapor-liquid interface area, perimeter, tank inner diameter, respectively. The correlations for the average Nusselt number are calculated by

a) Upper surface of a hot plate or lower surface of a cold plate [72]:

$$Nu = 0.54Ra^{1/4} \quad (10^4 \leq Ra \leq 10^7) \quad (2-30)$$

$$Nu = 0.15Ra^{1/3} \quad (10^7 \leq Ra \leq 10^{11}) \quad (2-31)$$

b) Lower surface of a hot plate or upper surface of a cold plate [73]:

$$Nu = 0.27Ra^{1/4} \quad (10^5 \leq Ra \leq 10^{10}) \quad (2-32)$$

where,

$$Ra = \frac{g\beta_v\Delta TL_{ref}^3}{\alpha_v\nu_v} \quad (2-33)$$

$\Delta T$  in Eq.(2-33) is the difference between the vapor temperature  $T_v$  and liquid temperature  $T_l$ .

Similarly,  $h_{l,interface}$  in the liquid phase is calculated by using Eqs. (2-28)-(2-33).

### 2.1.1.5 Equation of state

To calculate the density, specific heat capacity, and enthalpy of LNG and gaseous natural gas, the Peng-Robinson equation of state (PR-EoS) is used. The PR-EoS was initially developed to calculate the thermodynamic properties of natural gas. Later, it was widely used in the oil and gas industry due to its simplicity and versatility [74]. The PR-EoS can be expressed as [75]:

$$P = \frac{R_u T}{v - b} - \frac{a}{v(v + b) + b(v - b)} \quad (2-34)$$

where,

$$a = \sum_{i=1}^N \sum_{j=1}^N x_i x_j \sqrt{a_i a_j} \quad (2-35)$$

$$b = \sum_{i=1}^N x_i b_i \quad (2-36)$$

$$a_i = 0.45724 \frac{R_u^2 T_{cri_i}^2}{P_{cri_i}} \left\{ 1 + f_{\omega_i} \left[ 1 - \left( \frac{T}{T_{cri_i}} \right)^{0.5} \right] \right\}^2 \quad (2-37)$$

$$b_i = 0.0778 \frac{R_u T_{cri_i}}{P_{cri_i}} \quad (2-38)$$

$$f_{\omega_i} = 0.37464 + 1.54226\omega_i - 0.26992\omega_i^2 \quad (2-39)$$

The parameters  $\omega_i$ ,  $P_{cri_i}$ ,  $T_{cri_i}$  and  $x_i$  are the acentric factor, critical pressure and temperature, and mole fraction of species  $i$ , respectively.

The molar enthalpy and internal energy of the vapor and liquid phases at a given temperature and pressure can be calculated as follows [76],

$$h = \sum_i^N x_i h_i^{ideal} + P\mathcal{v} - R_u T - \frac{1}{2\sqrt{2}b} \left( a - T \frac{da}{dT} \right) \ln \left[ \frac{\mathcal{v} + (1 + \sqrt{2})b}{\mathcal{v} + (1 - \sqrt{2})b} \right] \quad (2-40)$$

$$u = \sum_i^N x_i h_i^{ideal} - R_u T - \frac{1}{2\sqrt{2}b} \left( a - T \frac{da}{dT} \right) \ln \left[ \frac{\mathcal{v} + (1 + \sqrt{2})b}{\mathcal{v} + (1 - \sqrt{2})b} \right] \quad (2-41)$$

$x_i$  is the mole fraction of species  $i$  in the liquid or vapor phases. The specific molar volume of the liquid or vapor phase,  $\mathcal{v}$ , is chosen to calculate the enthalpy and internal energy of the liquid or vapor phase accordingly. The ideal enthalpy of species  $i$  is calculated as follows:

$$h_i^{ideal} = h_i^{ref} + \int_{T_{ref}}^T c_{p,i}^{ideal} dT \quad (2-42)$$

In addition, the compressibility factor,  $Z$ , is defined as follows:

$$Z = \frac{Pv}{R_u T} \quad (2-43)$$

The standard PR-EoS predicts the specific molar volume (or density) of vapor phase. However, its prediction of the specific molar volume (or density) of the liquid phase is not accurate. Therefore, a volume-translated method is employed to modify the standard PR-EoS to calculate the specific molar volume (or densities) of the liquid phase [77]. The volume-translated function,  $v_{VTPR}$ , is defined as the sum of the specific molar volume calculated by the standard PR-EoS,  $v_{PR}$ , and the volume-translated term.

$$v_{VTPR} = v_{PR} + c - \delta_c \left( \frac{0.35}{0.35 + d} \right) \quad (2-44)$$

The dimensionless distance function,  $d$ , is given as

$$d = \frac{1}{R_u T_{cri}} \left( \frac{\partial P}{\partial \rho} \right)_T \quad (2-45)$$

$\delta_c$  in Eq. (2-44) is the volume correction at the critical temperature and is defined as,

$$\delta_c = v_{cri} - 3.95116b \quad (2-46)$$

The volume-translated term,  $c$ , in Eq. (2-44) is defined as

$$c = \left( \frac{RT_{cri}}{P_{cri}} \right) [c_1 - (0.004 + c_1)\exp(-2d)] \quad (2-47)$$

where,  $c_1$  is a constant, species-dependent parameter. In the liquid mixture, the determination of the  $c_{mix}$  is based on the mixing rule [78],

$$c_{mix} = \sum_i^N x_i c_i \quad (2-48)$$

Further information regarding the vapor-liquid equilibrium calculations and thermal properties of vapor and liquid mixtures is provided in Appendix B .

## **2.1.2 Computational algorithm in the non-equilibrium thermodynamic modelling**

The non-equilibrium thermodynamic model developed in this study is expected to calculate the thermodynamic state of the liquid and vapor phases in LNG storage tanks at the equilibrium and non-equilibrium states. The computational algorithms for the equilibrium and non-equilibrium states are discussed in this section.

### **2.1.2.1 Equilibrium thermodynamic modelling**

In an equilibrium thermodynamic modelling, it is assumed that the changes in the vapor and liquid phases are slow enough to ensure the system reaches the equilibrium state at each time step. Therefore, the vapor and liquid temperatures are identical. Figure 2.4 shows the algorithm of solving the governing equations under the thermal equilibrium assumption. The input parameters to the model include the tank geometry, tank positioning (horizontal vs vertical) and initial temperature, pressure and LNG level in the tank. The output parameters of this modelling are the tank pressure and temperature, LNG level in the tank, and the tank wall temperature. At every time step, the heat and mass transfers at the vapor-liquid interface are solved iteratively until the temperature difference between the liquid and vapor phases satisfies the convergence criteria ( $\epsilon <$

$10^{-3}$  K) (as shown with a dotted rhombus in Figure 2.4). The Newton-Raphson method is employed to solve the temperature of the liquid and vapor phases,  $T_l$  and  $T_v$ .

#### **2.1.2.2 Non-equilibrium thermodynamic modelling**

In the non-equilibrium thermodynamic modelling, the vapor and liquid phases have different temperatures. The flow chart of the non-equilibrium thermodynamic modelling is shown in Figure 2.4. The input and output parameters in this modelling are similar to those in the equilibrium thermodynamic modelling. In the non-equilibrium thermodynamic modelling, the heat and mass transfers in the liquid and vapor phases are solved only once at each time step without enforcing the vapor and liquid temperatures,  $T_v$  and  $T_l$ , to be equalized (as shown with a dashed line in Figure 2.4).

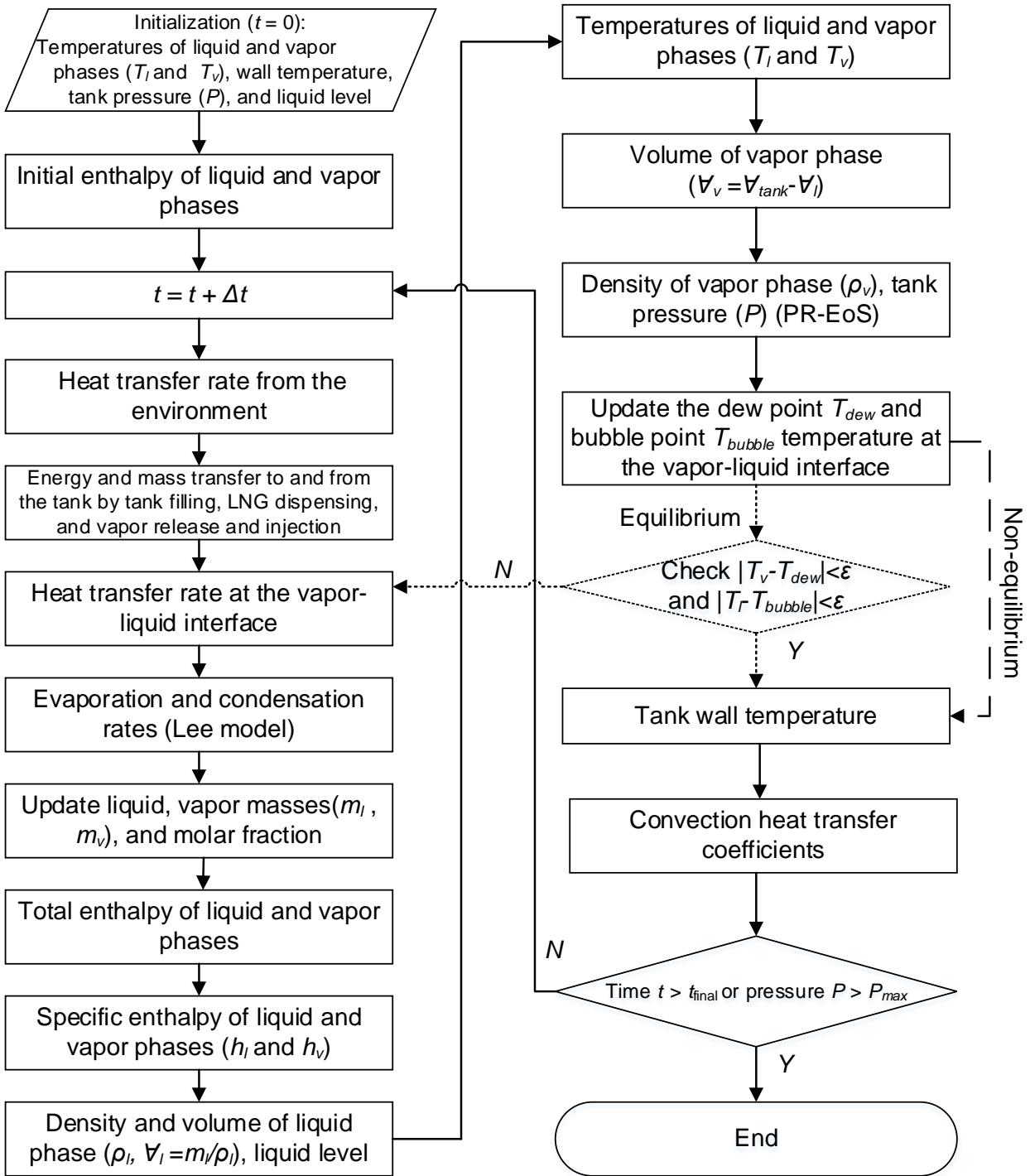


**Figure 2.4. The flow chart of solving governing equations for the equilibrium and non-equilibrium thermodynamic modelling. The dotted and dashed lines are for the equilibrium and non-equilibrium thermodynamic modelling, respectively.**

## 2.2 Non-equilibrium multilayer thermodynamic model

Figure 2.5 shows a schematic of a cylindrical LNG storage tank and the multilayer control volumes in the liquid and vapor domains. The heat transfer from the environment heats the LNG storage tank. The warm vertical walls adjacent to the LNG in the liquid domain and the gaseous natural gas in the vapor domain cause the formation of thermal boundary layers along the tank vertical walls. The buoyancy force moves the heated fluid in the boundary layer upward and creates flow circulations in the liquid and vapor domains. Under this mechanism, a temperature gradient or thermal stratification along the axial-axis ( $z$ -axis) of the LNG storage tank is created. To model this thermal phenomenon, the fluid flow and associated heat transfer are considered in the liquid and vapor domains.

### 2.2.1 Governing equations in the non-equilibrium multilayer thermodynamic model

#### 2.2.1.1 Conservation of mass in the liquid and vapor phases

(a) vapor domain

Figure 2.5 shows the  $n_v$  layers established in the vapor domain from the vapor-liquid interface (layer 1) to the top of the tank (layer  $n_v$ ). In each layer (or control volume), the fluid domain consists of the boundary layer along the tank vertical wall and a bulk vapor zone outside the boundary layer. The continuity equations in the vapor domain are derived as follows:

$$\frac{dm_{v,k}}{dt} = \dot{m}_{Bulk,v,k} - \dot{m}_{Bulk,v,k-1} - \dot{m}_{BL,v,k} + \dot{m}_{BL,v,k-1} \quad (1 < k < n_v) \quad (2-49)$$

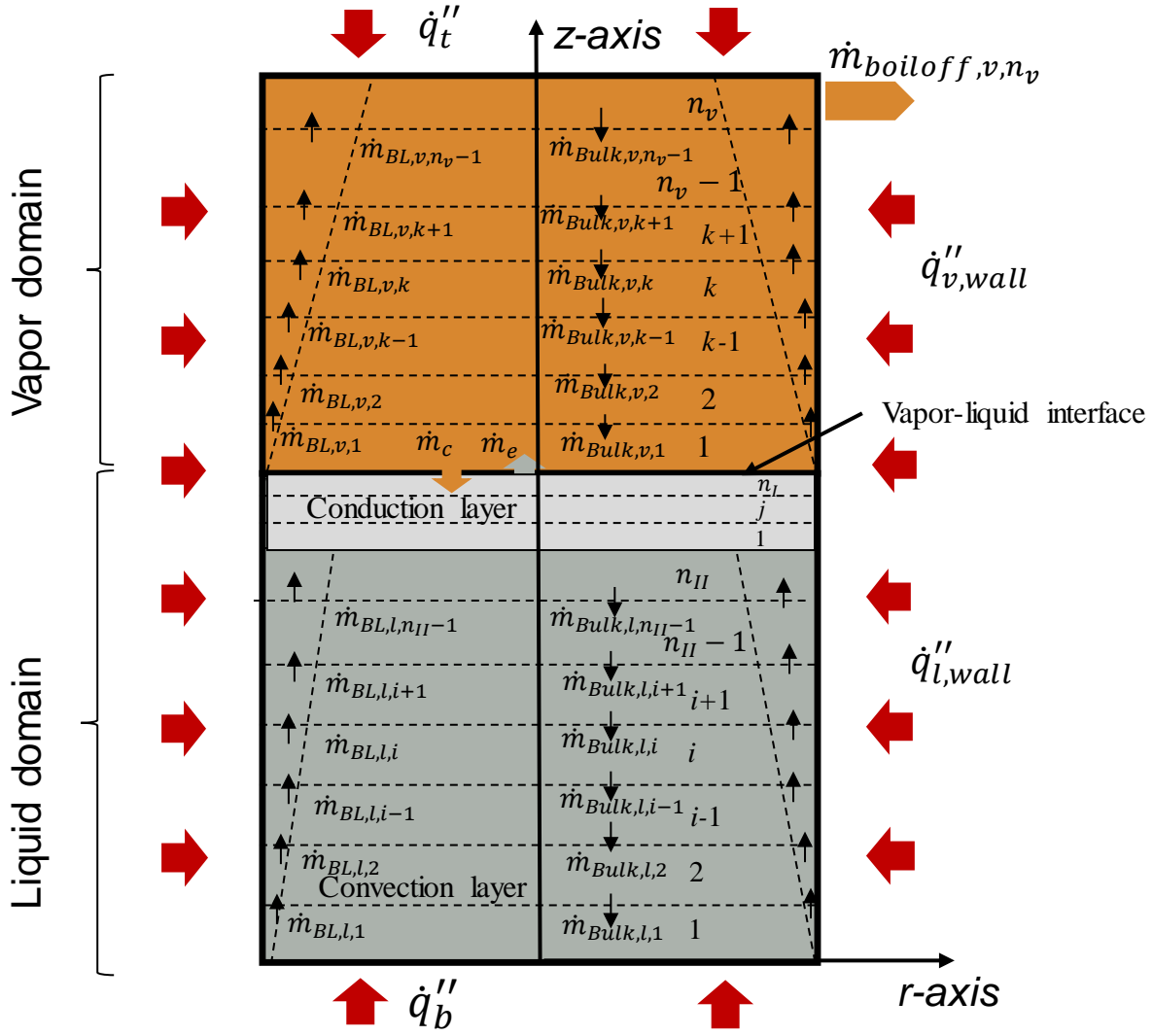


Figure 2.5. A schematic of the multilayer model in the liquid and vapor domains in a vertical cylindrical storage tank.

The first and the last vapor cells (layers 1 and  $n_v$ ) should accommodate for the evaporation and condensation mass transfer rates at the vapor-liquid interface,  $\dot{m}_e$  and  $\dot{m}_c$ , and the BOG release rate from the tank, respectively. Therefore, the continuity equations for the first and the last vapor cells are derived as,

$$\frac{dm_{v,1}}{dt} = \dot{m}_{Bulk,v,1} - \dot{m}_{BL,v,1} + \dot{m}_e - \dot{m}_c \tag{2-50}$$

$$\frac{dm_{v,n_v}}{dt} = -\dot{m}_{Bulk,v,n_v-1} + \dot{m}_{BL,v,n_v-1} - \dot{m}_{boiloff,v,n_v} \quad (2-51)$$

The summation of Eqs. (2-49)-(2-51) in the vapor domain gives the total mass of vapor phase:

$$\sum_{k=1}^{n_v} \frac{dm_{v,k}}{dt} = \frac{dm_{v,total}}{dt} = \dot{m}_e - \dot{m}_c - \dot{m}_{boiloff,v,n_v} \quad (2-52)$$

where,  $m_{v,k}$  and  $m_{v,total}$  represent the mass of the vapor layer  $k$ , and the total mass of the vapor phase, respectively.

#### (b) liquid domain

In the liquid domain, experimental studies indicated that a thermal conduction layer forms near the vapor-liquid interface [44,46]. Consequently, in this model, two subdomains are created in the liquid phase: a conduction domain and a convection domain.

The conduction domain is divided into multilayers ( $j = 1, \dots, n_l$ ). In the conduction domain, the conduction heat transfer is the dominant phenomenon, and the boundary layer formation is neglected [79]. The continuity equations in the conduction domain are as follows:

$$\frac{dm_{l,j}}{dt} = 0 \quad (1 \leq j < n_l) \quad (2-53)$$

$$\frac{dm_{l,n_l}}{dt} = -\dot{m}_e + \dot{m}_c \quad (2-54)$$

The convection domain in the liquid phase is divided into multilayers ( $i = 1, \dots, n_{II}$ ), and the derivation of continuity equations is similar to the vapor domain:

$$\frac{dm_{l,1}}{dt} = \dot{m}_{Bulk,l,1} - \dot{m}_{BL,l,1} \quad (2-55)$$

$$\frac{dm_{l,i}}{dt} = \dot{m}_{Bulk,l,i} - \dot{m}_{Bulk,l,i-1} - \dot{m}_{BL,l,i} + \dot{m}_{BL,l,i-1} \quad (1 < i < n_{II}) \quad (2-56)$$

$$\frac{dm_{l,n_{II}}}{dt} = -\dot{m}_{Bulk,l,n_{II}-1} + \dot{m}_{BL,l,n_{II}-1} \quad (2-57)$$

Therefore, the total mass of the liquid phase is equal to the sum of the masses in the conduction and convection domains:

$$\sum_{j=1}^{n_I} \frac{dm_{l,j}}{dt} + \sum_{i=1}^{n_{II}} \frac{dm_{l,i}}{dt} = \frac{dm_{l,total}}{dt} = -\dot{m}_e + \dot{m}_c \quad (2-58)$$

Adding Eqs. (2-52) and (2-59), the conservation of mass in the storage tank is satisfied.

$$\frac{d(m_{v,total} + m_{l,total})}{dt} = \frac{dm_{total}}{dt} = -\dot{m}_{boiloff,v,n_v} \quad (2-59)$$

In addition, the summation of volumes of the vapor phase (Eq. (2-60)) and liquid phase (Eq. (2-61)) equals the entire volume of the tank (Eq.(2-62)).

$$\forall_{v,total} = \sum_{k=1}^{n_v} \forall_{v,k} = \sum_{k=1}^{n_v} \left( \frac{m_{v,k}}{\rho_{v,k}(T_{v,k}, P)} \right) \quad (2-60)$$

$$\forall_{l,total} = \sum_{j=1}^{n_I} \forall_{l,j}^I + \sum_{i=1}^{n_{II}} \forall_{l,i}^{II} = \sum_{j=1}^{n_I} \left( \frac{m_{l,j}}{\rho_{l,j}(T_{l,j}, P)} \right) + \sum_{i=1}^{n_{II}} \left( \frac{m_{l,i}}{\rho_{l,i}(T_{l,i}, P)} \right) \quad (2-61)$$

$$\forall_{v,total} + \forall_{l,total} = \forall_{tank} \quad (2-62)$$

The evaporation and condensation rates at the vapor-liquid interface are calculated using the method described in Section 2.1.1.1 (Eqs. (2-3) and (2-4)).

### 2.2.1.2 Conservation of energy in the liquid and vapor phases

(a) vapor domain

The energy equations in the vapor phase are given as follows:

$$\begin{aligned} \frac{dH_{v,1}}{dt} = & \dot{Q}_{v,wall,1} + \dot{Q}_{lv} - \dot{m}_{BL,v,1} \cdot h_v(T_{v,1}, P) + \dot{m}_{Bulk,v,1} \cdot h_v(T_{v,2}, P) + \dot{m}_e \\ & \cdot h_v(T_{bubble}, P) - \dot{m}_c \cdot h_l(T_{dew}, P) + \dot{Q}_{v,layer,1} + \forall_{v,1} \frac{dP}{dt} \end{aligned} \quad (2-63)$$

$$\begin{aligned} \frac{dH_{v,k}}{dt} = & \dot{Q}_{v,wall,k} - (\dot{m}_{BL,v,k} + \dot{m}_{Bulk,v,k-1}) \cdot h_v(T_{v,k}, P) + \dot{m}_{BL,v,k-1} \cdot h_v(T_{v,k-1}, P) \\ & + \dot{m}_{Bulk,v,k} \cdot h_v(T_{v,k+1}, P) + \dot{Q}_{v,layer,k} - \dot{Q}_{v,layer,k-1} + \forall_{v,k} \frac{dP}{dt} \\ & (1 < k < n_v) \end{aligned} \quad (2-64)$$

$$\begin{aligned} \frac{dH_{v,n_v}}{dt} = & \dot{Q}_{v,wall,n_v} + \dot{Q}_t - \dot{m}_{Bulk,v,n_v-1} \cdot h_v(T_{v,n_v}, P) + \dot{m}_{BL,v,n_v-1} \cdot h_v(T_{v,n_v-1}, P) \\ & - \dot{Q}_{v,layer,n_v-1} + \forall_{v,n_v} \frac{dP}{dt} - \dot{m}_{boiloff,v,n_v} \cdot h_v(T_{v,n_v}, P) \end{aligned} \quad (2-65)$$

(b) liquid domain

The energy equations in the liquid phase are divided into two parts. In the conduction domain, the energy equations are calculated as,

$$\frac{dH_{l,1}^I}{dt} = \dot{Q}_{l,wall,1}^I + \dot{Q}_{l,layer,1}^I - \dot{Q}_{l,layer,n_{II}}^{II} + \forall_{l,1}^I \frac{dP}{dt} \quad (2-66)$$

$$\frac{dH_{l,j}^I}{dt} = \dot{Q}_{l,wall,j}^I + \dot{Q}_{l,layer,j}^I - \dot{Q}_{l,layer,j-1}^I + \forall_{l,j}^I \frac{dP}{dt} \quad (1 < j < n_I) \quad (2-67)$$

$$\frac{dH_{l,n_I}^I}{dt} = \dot{Q}_{l,wall,n_I}^I - \dot{m}_e \cdot h_v(T_{bubble}, P) + \dot{m}_c \cdot h_l(T_{dew}, P) - \dot{Q}_{lv} - \dot{Q}_{l,layer,n_I-1}^I + \forall_{l,n_I}^I \frac{dP}{dt} \quad (2-68)$$

In the convection domain, the energy equations are given as follows:

$$\frac{dH_{l,1}^{II}}{dt} = \dot{Q}_{l,wall,1}^{II} + \dot{Q}_b + \dot{m}_{Bulk,l,1} \cdot h_l(T_{l,2}, P) - \dot{m}_{BL,l,1} \cdot h_l(T_{l,1}, P) + \dot{Q}_{l,layer,1}^{II} + \forall_{l,1}^{II} \frac{dP}{dt} \quad (2-69)$$

$$\begin{aligned} \frac{dH_{l,i}^I}{dt} = & \dot{Q}_{l,wall,i} - (\dot{m}_{BL,l,i} + \dot{m}_{Bulk,l,i-1}) \cdot h_l(T_{l,i}, P) + \dot{m}_{BL,l,i-1} \cdot h_l(T_{l,i-1}, P) \\ & + \dot{m}_{Bulk,l,i} \cdot h_l(T_{l,i+1}, P) + \dot{Q}_{l,layer,i}^I - \dot{Q}_{l,layer,i-1}^I + \nabla_{l,i}^I \frac{dP}{dt} \quad (1 < i < n_{II}) \end{aligned} \quad (2-70)$$

$$\begin{aligned} \frac{dH_{l,n_{II}}^I}{dt} = & \dot{Q}_{l,wall,n_{II}} + \dot{m}_{BL,l,n_{II}-1} \cdot h_l(T_{l,n_{II}-1}, P) - \dot{m}_{Bulk,l,n_{II}-1} \cdot h_l(T_{l,n_{II}}, P) \\ & + \dot{Q}_{l,layer,n_{II}}^I - \dot{Q}_{l,layer,n_{II}-1}^I + \nabla_{l,n_{II}}^I \frac{dP}{dt} \end{aligned} \quad (2-71)$$

In Eqs. (2-63)-(2-71),  $H_{v,k}$ ,  $H_{l,j}^I$ , and  $H_{l,i}^I$  are the total enthalpies of vapor cell  $k$ , liquid cell  $j$  in the conduction domain, and liquid cell  $i$  in the convection domain, respectively. These parameters are defined as,

$$H_{v,k} = m_{v,k} \cdot h_v(T_{v,k}, P) \quad (1 \leq k \leq n_v) \text{ in vapor domain} \quad (2-72)$$

$$H_{l,j}^I = m_{l,j} \cdot h_l(T_{l,j}, P) \quad (1 \leq j \leq n_l) \text{ in conduction domain} \quad (2-73)$$

$$H_{l,i}^I = m_{l,i} \cdot h_l(T_{l,i}, P) \quad (1 \leq i \leq n_{II}) \text{ in convection domain} \quad (2-74)$$

$h_v$  and  $h_l$  are the specific mass enthalpies of the vapor and liquid phases at a given temperature and pressure, respectively.

In Eqs. (2-63)-(2-71),  $h_v$  and  $h_l$  are the specific mass enthalpy of vapor and liquid phases at a given temperature and pressure, respectively. Also,  $\dot{Q}_{v,wall,k}$ ,  $\dot{Q}_{l,wall,j}^I$  and  $\dot{Q}_{l,wall,i}^I$  are the heat transfer rates from the tank side vertical walls to the vapor cell  $k$ , the liquid cell  $j$  in the conduction domain, and the liquid cell  $i$  in the convection domain, respectively.  $\dot{Q}_t$  and  $\dot{Q}_b$  are the heat transfer rates from the tank top wall to the vapor cell  $n_v$ , and from the tank bottom wall to the liquid cell 1 in the

convection domain, respectively.  $\dot{Q}_{lv}$  represents the natural convection heat transfer rate from the liquid phase to the vapor phase at the vapor-liquid interface.

$\dot{Q}_{v,layer,k}$  represents the heat transfer rate from the vapor cell  $k+1$  to the vapor cell  $k$ . Similarly,  $\dot{Q}_{l,layer,j}^I$  and  $\dot{Q}_{l,layer,i}^{II}$  represent the heat transfer rates from the liquid cell  $j+1$  to the liquid cell  $j$  in the conduction domain, and from the liquid cell  $i+1$  to the liquid cell  $i$  in the convection domain, respectively. These parameters are calculated as follows:

$$\dot{Q}_{v,layer,k} = h_{v,layer,k} A_{interface} (T_{v,k+1} - T_{v,k}) \quad (2-75)$$

$$\dot{Q}_{l,layer,j}^I = h_{l,layer,j} A_{interface} (T_{l,j+1} - T_{l,j}) \quad (2-76)$$

$$\dot{Q}_{l,layer,i}^{II} = h_{l,layer,i} A_{interface} (T_{l,i+1} - T_{l,i}) \quad (2-77)$$

In the liquid conduction domain,  $Nu_{l,layer,j}$  is equal to 1 (i.e., only conduction heat transfer).

Therefore, the heat transfer coefficient  $h_{l,layer,j}$  is calculated as below,

$$\frac{h_{l,layer,j} d_{l,layer,j}}{\bar{k}_{l,j}} = 1 \quad (2-78)$$

The heat transfer coefficients  $h_{v,layer,k}$  and  $h_{l,layer,i}$  are calculated from  $Nu_{v,layer,k}$  and

$Nu_{l,layer,i}$ ,

$$Nu_{v,layer,k} = \frac{h_{v,layer,k} d_{v,layer,k}}{k_{v,k}} \quad (2-79)$$

$$Nu_{l,layer,i} = \frac{h_{l,layer,i} d_{l,layer,i}}{\bar{k}_{l,i}} \quad (2-80)$$

where,  $\overline{k_{v,k}}$ ,  $\overline{k_{l,j}}$ , and  $\overline{k_{l,i}}$  are the average thermal conductivities between the vapor cells  $k$  and  $k+1$ , between the liquid cells  $j$  and  $j+1$  in the conduction domain, and between the liquid cells  $i$  and  $i+1$  in the conduction domain, respectively.  $d_{v,layer,k}$ ,  $d_{l,layer,j}$ , and  $d_{l,layer,i}$  are the thicknesses of the vapor cell  $k$ , liquid cell  $j$  in the conduction domain, and liquid cell  $i$  in the convection domain, respectively.

If  $T_{v,k+1} > T_{v,k}$ , the conduction heat transfer is considered between the vapor cells  $k$  and  $k+1$ .

If  $T_{v,k+1} < T_{v,k}$ , the conduction heat transfer for low  $Ra_v (< 1,708)$  and the convection heat transfer for high  $Ra_v (\geq 1,708)$  are considered between the vapor cells  $k$  and  $k+1$  [80].  $Ra_v$  is defined as

$$Ra_v = \frac{g\beta_v(T_{v,k} - T_{v,k+1})d_{v,layer,k}^3}{\alpha_v\nu_v} \quad (2-81)$$

where,  $g$ ,  $\alpha_v$ ,  $\beta_v$ , and  $\nu_v$  are the gravity acceleration ( $m/s^2$ ), thermal diffusivity ( $m^2/s$ ), thermal expansion coefficient ( $1/K$ ), and kinematic viscosity ( $m^2/s$ ) of the vapor phase.

The thermal expansion coefficient is calculated by

$$\beta_v = -\frac{1}{\rho_v} \left( \frac{\partial \rho_v}{\partial T} \right)_p \quad (2-82)$$

The empirical correlation of heat transfer in an enclosure is employed to calculate the Nusselt number in the vapor phase,  $Nu_{v,layer,k}$  [80,81].

$$Nu_{v,layer,k} = \begin{cases} 1 & \text{if } T_{v,k+1} > T_{v,k} & \text{(conduction)} \\ 1 & \text{if } T_{v,k+1} < T_{v,k}, \text{ and } Ra_v < 1708 & \text{(conduction)} \\ 0.069Ra_v^{1/3} Pr_v^{0.074} & \text{if } T_{v,k+1} < T_{v,k}, \text{ and } Ra_v \geq 1708 & \text{(convection)} \end{cases} \quad (2-83)$$

where,  $Pr_v$  is the Prandtl number of vapor phase. Similar correlations are applied to calculate the Nusselt number in the convection domain of the liquid phase,  $Nu_{l,layer,i}$ .

### 2.2.1.3 Boundary layer

The inner vertical wall of the tank is modeled by a vertical plate with a uniform heat flux rate. In the vapor domain, two Grashof numbers,  $Gr_v$  and  $Gr_{qv}$ , are defined to describe the properties of the boundary layer.  $Gr_v$  is determined by the temperature difference between the vapor cell  $k$  and the vertical tank wall.

$$Gr_v = \frac{g\beta_v(T_{wall} - T_{v,k})l_{v,k}^3}{\nu_v^2} \quad (2-84)$$

$Gr_{qv}$  is determined by the heat flux rate  $\dot{q}''_{v,wall}$ ,

$$Gr_{qv} = \frac{g\beta_v \dot{q}''_{v,wall} l_{v,k}^4}{\nu_v^2 k_v} \quad (2-85)$$

where,  $l_{v,k}$  is the distance between the vapor cell  $k$  and the vapor-liquid interface. At the vapor-liquid interface,  $l_{v,k}$  is equal to 0. Then, the corresponding Raleigh numbers,  $Ra_v$  and  $Ra_{qv}$ , are defined as,

$$Ra_v = Gr_v Pr_v \quad (2-86)$$

$$Ra_{qv} = Gr_{qv} Pr_v \quad (2-87)$$

The Nusselt number  $Nu_v$  on the tank vertical walls in the vapor phase is calculated by [82,83],

$$Nu_v = \frac{h_v l_{v,k}}{k_v} = 0.62 \left( \frac{Pr_v Ra_{qv}}{0.8 + Pr_v} \right)^{0.2}, Ra_{qv} \leq 10^{12} \text{ (laminar)} \quad (2-88)$$

$$Nu_v = \frac{h_v l_{v,k}}{k_v} = 0.17 Ra_{qv}^{0.25}, Ra_{qv} > 10^{12} \text{ (turbulent)} \quad (2-89)$$

Using the definition of the heat flux rate on the vertical wall, given in Eq. (2-90), the temperature difference between the vapor cell  $k$  and the wall is calculated.

$$\dot{q}''_{wall,v} = h_v(T_{wall} - T_{v,k}) \quad (2-90)$$

$$\Delta T_{v,k} = T_{wall} - T_{v,k} = \frac{\dot{q}''_{v,wall} l_{v,k}}{Nu_v k_v} \quad (2-91)$$

The thickness of the velocity boundary layer,  $\delta_{v,k}$ , can be calculated as [84,85],

$$\delta_{v,k} = \begin{cases} 3.93 l_{v,k} \left( \frac{0.952 + Pr_v}{Ra_v} \right)^{1/4} Pr_v^{-1/4} & \textit{laminar} \\ 0.565 l_{v,k} \left( \frac{1 + 0.494 Pr_v^{2/3}}{Ra_v} \right)^{1/10} Pr_v^{-13/30} & \textit{turbulent} \end{cases} \quad (2-92)$$

The upward mass flow rates in the boundary layer of the vapor phase are calculated by [52],

$$\dot{m}_{v,k} = 2\pi R_{inner} \rho_v V_{v,k} \delta_{v,k} \times \begin{cases} 0.0833 & \textit{laminar} \\ 0.1436 & \textit{turbulent} \end{cases} \quad (2-93)$$

where, the average velocity of the upward boundary-layer flow  $V_{v,k}$  is [86,87],

$$V_{v,k} = 1.185 \frac{v_{v,k}}{l_{v,k}} \left( \frac{Gr_v}{1 + 0.494 Pr_v^{2/3}} \right)^{1/2} \quad (2-94)$$

A similar method is employed to calculate the corresponding variables in the liquid domain.

#### 2.2.1.4 Thermal stratification in the liquid domain

Due to the upward flow in the liquid boundary layer along the tank vertical walls, the thermal stratification from the vapor-liquid interface gradually grows over time. In the stratified layer, the conduction heat transfer is the main form of heat transfer between the liquid cells. The thickness of this conduction domain,  $\Delta$ , is calculated as [79],

$$\frac{\Delta}{H_l} = 1 - \left[ 1 - 0.616 \left( \frac{\xi v_l t}{H_l R_{inner}} \right) \frac{(Gr_{ql})^{1/5}}{(0.8 + Pr_l)^{1/5} Pr_l^{3/5}} \right]^5 \quad (laminar) \quad (2-95)$$

$$\frac{\Delta}{H_l} = 1 - \left[ 1 + 0.082 \left( \frac{\xi v_l t}{H_l R_{inner}} \right) \left( \frac{Gr_{ql}}{Pr_l} \right)^{2/7} \right]^{-7} \quad (turbulent) \quad (2-96)$$

where,

$$Gr_{ql} = \frac{g \beta_l \dot{q}''_{l,wall} H_l^4}{v_l^2 k_l} \quad (2-97)$$

and  $\xi$  is a time adjustment factor, which is determined by the experimental data. In addition, the stratified layer growth is valid based on the assumption that the heat transfer occurs from the vapor-liquid interface to the bulk liquid. Therefore, in this study, the thickness of the conduction domain,  $\Delta$ , is only valid where  $T_{l,j+1} > T_{l,j}$ .

### 2.2.1.5 Mass transfer between the heel and cargo layers

The mass transfer between the heel and cargo layers occurs due to their composition and density differences. In the present study, it is assumed that the mole fractions of species in the entire heel and cargo domains are uniform, respectively. The convective mass transfer rates between the heel and cargo layers are calculated by Eqs. (2-98) and (2-99).

$$\begin{aligned} \frac{d}{dt} (c_{cargo,species\ i} V_{cargo}) \\ = A_{interface} h_{mass,species\ i} (c_{heel,species\ i} - c_{cargo,species\ i}) \end{aligned} \quad (2-98)$$

$$\begin{aligned}
\frac{d}{dt}(c_{heel,species\ i}V_{heel}) & \quad (2-99) \\
& = -A_{interface}h_{mass,species\ i}(c_{heel,species\ i} - c_{cargo,species\ i}) \\
& \quad - \dot{m}_e y_{species\ i}^e / \sum_{species\ i}^N (y_{species\ i}^e M_{species\ i}) \\
& \quad + \dot{m}_c x_{species\ i}^c / \sum_{species\ i}^N (x_{species\ i}^c M_{species\ i})
\end{aligned}$$

where,  $c_{heel, species\ i}$  and  $c_{cargo, species\ i}$  are the molar volume concentrations of species  $i$  in the heel and cargo layers, respectively (kmole/m<sup>3</sup>).  $x_{species\ i}^c$  is the mole fraction of species  $i$  in the liquid phase condensed from the vapor phase, and  $y_{species\ i}^e$  is the mole fraction of species  $i$  in the vapor phase evaporated from the liquid phase.  $M_{species\ i}$  is the molar mass of species  $i$  (kg/kmole). The mole fraction of species  $i$  in the vapor phase,  $y_{species\ i}^e$ , originated from the evaporation of the bulk liquid phase with mole fraction  $x_{species\ i}$ , and the mole fraction of species  $i$  in the liquid phase,  $x_{species\ i}^c$ , originated from the condensation of the bulk vapor phase with mole fraction  $y_{species\ i}$  are calculated by  $K$  values ( $K_{species\ i}^e$  and  $K_{species\ i}^c$ ),

$$K_{species\ i}^e = \frac{y_{species\ i}^e}{x_{species\ i}} \quad (2-100)$$

$$K_{species\ i}^c = \frac{y_{species\ i}}{x_{species\ i}^c} \quad (2-101)$$

$K$  values are equal to the ratio of the liquid phase fugacity to the vapor phase fugacity at the vapor-liquid equilibrium (VLE) state discussed in Appendix B .

To calculate the convective mass transfer film coefficient,  $h_{mass}$ , Reynolds analogy [88] is used,

$$h_{mass} = \frac{h_{heat}}{\bar{\rho}\bar{c}_p} \quad (2-102)$$

where,  $\bar{\rho}$  and  $\bar{c}_p$  are the average density (kg/m<sup>3</sup>), and the average of the specific heat capacity (W/(kg·K)) of the heel and the cargo interface layers, respectively. The convective heat transfer coefficient,  $h_{heat}$ , is calculated by using the Nusselt number,  $Nu_{heat}$ , defined on a horizontal plate:

$$Nu_{heat} = \frac{h_{heat}L_{ref}}{\bar{k}} \quad (2-103)$$

where,  $\bar{k}$  is the average thermal conductivity of the heel and the cargo layers (W/(m·K)).  $Nu_{heat}$  is calculated by Eqs. (2-104) and (2-105) [72].

$$Nu_{heat} = 0.54Ra_{heat}^{1/4} \quad (2.2 \times 10^4 \leq Ra_{heat} \leq 8 \times 10^6) \quad (2-104)$$

$$Nu_{heat} = 0.15Ra_{heat}^{1/3} \quad (8 \times 10^6 < Ra_{heat} \leq 1.6 \times 10^9) \quad (2-105)$$

The Rayleigh number,  $Ra_{heat}$ , based on the density difference between the heel and the cargo layers,  $\Delta\rho$ , is calculated as follows:

$$Ra_{heat} = \frac{g\Delta\rho L_{ref}^3 \bar{Pr}}{\bar{\rho} \nu_{LNG}^2} \quad (2-106)$$

where,  $\nu_{LNG}$  is the kinematic viscosity of LNG (m<sup>2</sup>/s) and  $\bar{Pr}$  is the average Prandtl number of the heel and cargo layers. The reference length,  $L_{ref}$ , in Eqs. (2-103) and (2-106) is defined by Eq. (2-29).

Equation (2-107) gives the total mass transfer rate between the cargo and heel layers (positive if the mass is transferred from the heel to cargo).

$$\dot{m}_s = \sum_{species\ i}^N \dot{m}_{species\ i} = \sum_{speices\ i}^N M_{species\ i} \frac{d}{dt} (c_{cargo,species\ i} \nabla_{cargo}) \quad (2-107)$$

To accommodate the mass transfer at the heel-cargo interface, the mass source term,  $\dot{m}_s$ , is added to the mass conservation equation (Eq. (2-56)) in the liquid cells adjacent to the heel-cargo interface. The values of these mass source terms are positive and negative in the heel and cargo cells, respectively.

The heat transfer rate at the vapor-liquid interface, the equation of state, and the thermal properties of the liquid and vapor phases are calculated similarly to those discussed in the non-equilibrium thermodynamic method.

### **2.2.2 Computational algorithm in the non-equilibrium multilayer thermodynamic modelling**

Figure 2.6 shows the steps required to solve the governing equations in the liquid and vapor domains in the non-equilibrium multilayer thermodynamic modelling. As the volume of the LNG in the tank changes over time due to the heat transfer from the environment and phase change at the vapor-liquid interface, the liquid and vapor domains are re-meshed at each time step to adjust the new liquid and vapor volumes, respectively. The physical properties are mapped from the old mesh domain to the new mesh domain accordingly. In the vapor domain, the pressure and bulk mass flow rates exchanged between the numerical cells are determined in an iterative method, and an under-relaxation factor of 0.05-0.4 is used to stabilize the numerical calculation procedure.

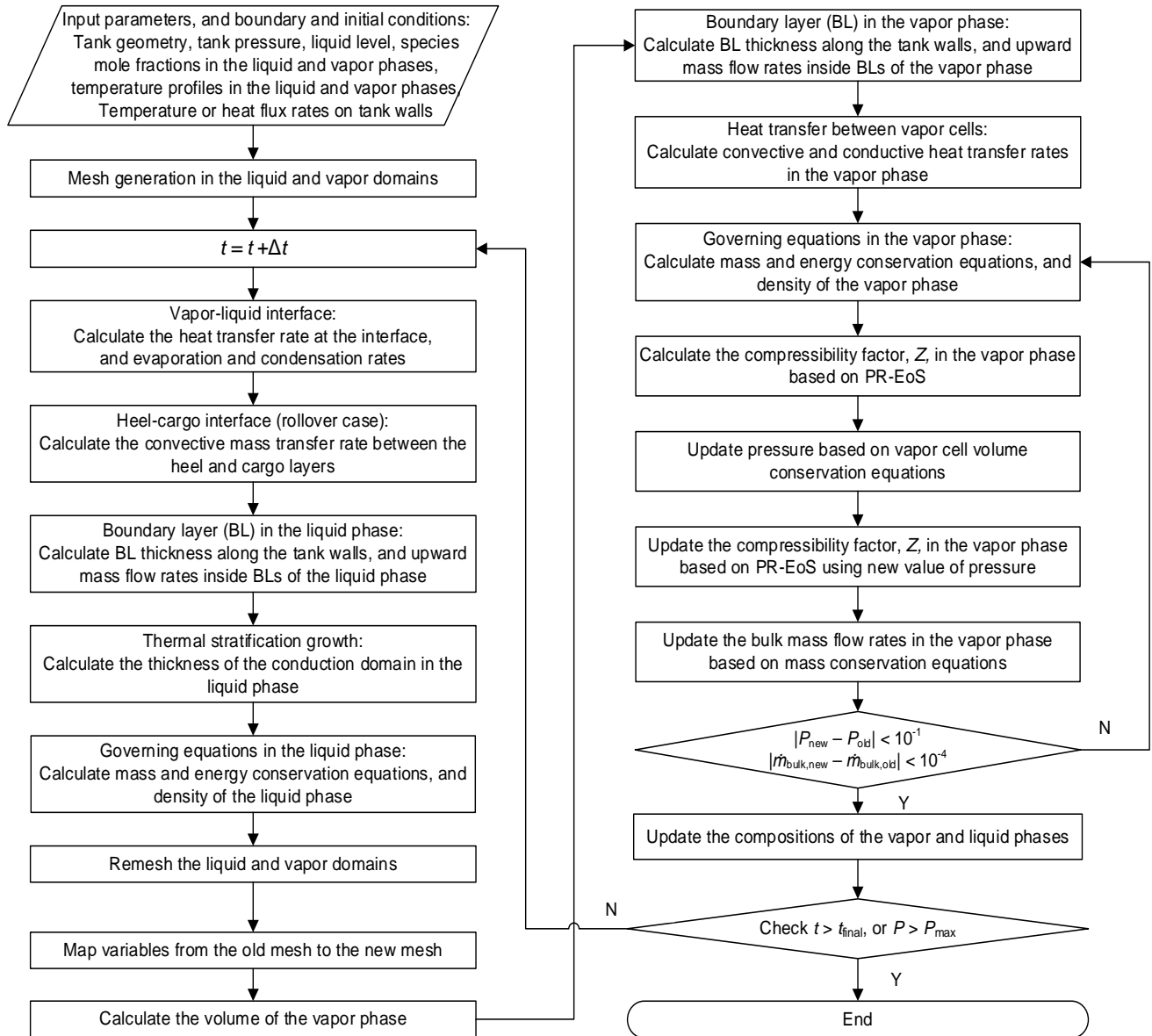


**Figure 2.6. Flow chart to solve the governing equations in a non-equilibrium multilayer thermodynamic model for a cryogenic vertical storage tank.**

## **Chapter 3: Results from Non-equilibrium Thermodynamic Modelling**

### **3.1 Model validation**

In this section, the results of a non-equilibrium thermodynamic model are compared against two sets of experimental data from horizontal and vertical tanks.

#### **3.1.1 The horizontal tank**

To validate the accuracy of the thermodynamic models, experimental data of a horizontal onboard tank reported by Harper and Powars [89] are considered. The tank was initially filled to 75% of its total capacity. The initial pressure of the tank was 283 kPa, and the tank was tested under stationary conditions. The pressure of the tank gradually increased due to heat transfer from the environment until it reached the MAWP of the tank at 1,585 kPa. LNG is assumed to be pure methane for this analysis. The details of the experiment are summarized in Table 3.1.

**Table 3.1. The geometry, thermal properties, and initial conditions in a horizontal LNG storage tank reported by Harper and Powars [89].**

<b>Parameter</b>	<b>Symbol</b>	<b>Value</b>	<b>Remarks</b>
Tank net capacity	$V_{tank}$	0.257 m <sup>3</sup>	
Length of the inner tank	$L_{tank}$	0.909 m	
Inner diameter of the tank	$D_i$	0.6 m	
Tank thickness (including insulation layer)	$t_{tank}$	0.03m	
Mass of the tank (empty)	$m_{tank}$	175 kg	Calculated from the density of stainless steel 304
Specific heat capacity of the tank	$c_{p,tank}$	477 J/kg·K	Assumed from stainless steel 304
Overall heat transfer rate to the tank	$\dot{Q}_{tank}$	20.9 W	
Surface area of the inner tank	$A_{tank}$	2.279 m <sup>2</sup>	
Ambient temperature	$T_{ambient}$	25°C	
Maximum allowable working pressure	MAWP	1,585 kPa	
<b>Initial conditions</b>			
LNG tank level	$L_l$	0.4212 m	
LNG temperature	$T_{l,initial}$	125.7 K	Assumed equilibrium state in the tank
Vapor phase temperature	$T_{v,initial}$	125.7 K	Assumed equilibrium state in the tank
LNG pressure	$P_{initial}$	283 kPa	
Time step	$\Delta t$	60 s	Selected based on the results at 30-, 60-, and 120-s time steps

A comparison of the numerical results and experimental data is shown in Figure 3.1. It can be seen that the results of the equilibrium and non-equilibrium thermodynamic models agree with the experimental data of the stationary horizontal tank. The maximum relative difference between the numerical and experimental data is 8%. The average relative differences between the experimental data and the numerical data calculated by the equilibrium and non-equilibrium thermodynamic models are 3% and 5%, respectively. Considering the duration of the experiment (140 h) and lack of information on the uncertainty of experimental data reported by Harper and Powars [89], the average relative differences of 3% and 5% between the pressures calculated by the numerical

models and the experimental data are reasonable. This model validation highlights that both equilibrium and non-equilibrium thermodynamic models have good accuracy in predicting the pressure of stationary tanks when no external agent, such as vibration and vapor injection to the tank, disturbs the liquid and vapor domains.

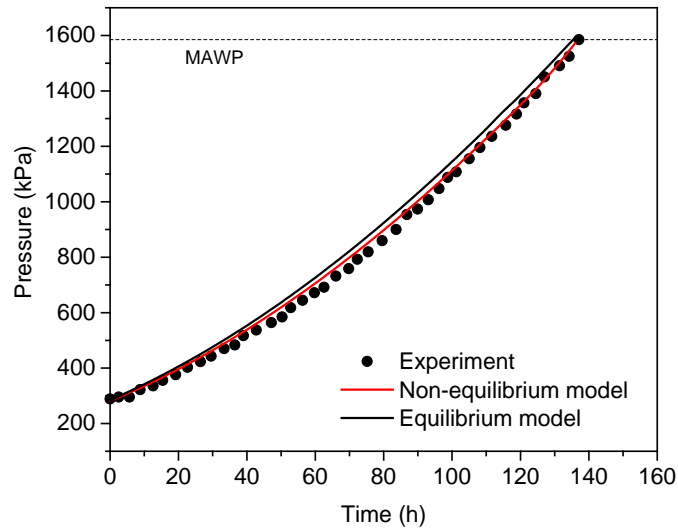


**Figure 3.1. A comparison between the results of the equilibrium and non-equilibrium thermodynamic models developed in this study and the experimental data of a horizontal tank reported by Harper and Powars [89].**

### 3.1.2 The vertical tank

Ludwig et al. [90] conducted an experiment on a vertical tank filled with liquid nitrogen. In the present study, the models are developed independently from the tank geometry and cryogenic fluid properties. Therefore, the models should be able to predict the performance of a vertical tank filled with liquid nitrogen. The vertical tank used in the experiment of Ludwig et al. [90] and the locations of thermocouples installed inside the tank are shown in Figure 3.2. The tank geometry, and initial and boundary conditions are summarized in Table 3.2.

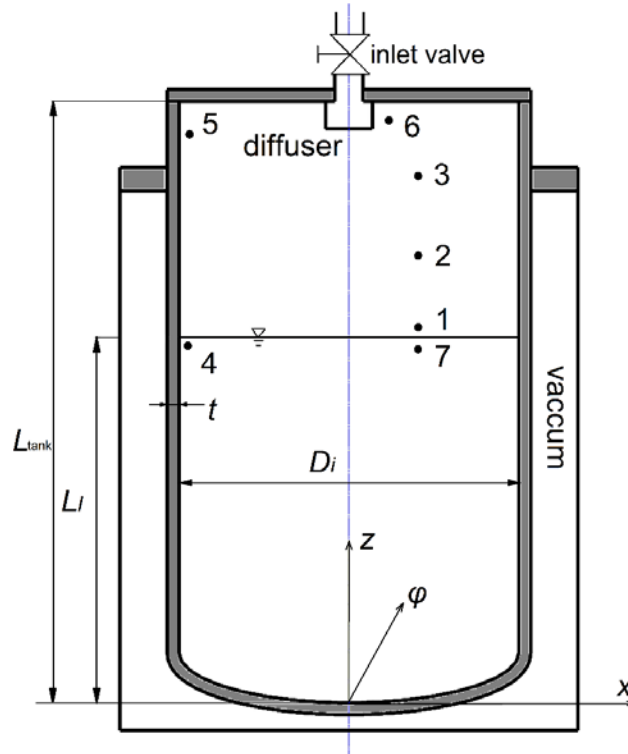


Figure 3.2. Schematic of the liquid nitrogen vertical tank and the location of thermocouples [90].

Table 3.2. The geometry of the vertical tank and its initial conditions in the experiment of Ludwig et al. [90].

Parameter	Symbol	Value	Remarks
Tank net capacity	$V_{tank}$	$43 \times 10^{-3} \text{ m}^3$	
Length of the inner tank	$L_{tank}$	0.650 m	
Inner diameter of the tank	$D_i$	0.296 m	
Tank thickness (including insulation layer)	$t$	1.5 mm	
Mass of the tank (empty)	$m_{tank}$	9.73 kg	Calculated from the density of stainless steel 304
Specific heat capacity of the tank	$c_{p,tank}$	477 J/kg·K	Assumed for stainless steel 304
Surface area of the inner tank	$A_{tank}$	0.742 m <sup>2</sup>	
Ambient temperature	$T_{ambient}$	25°C	
<b>Initial conditions</b>			
LN <sub>2</sub> tank level	$L_l$	0.455 ± 0.001 m	
LN <sub>2</sub> temperature	$T_{l,initial}$	77.7 K	
Vapor phase temperature	$T_{v,initial}$	150.9 K	
LNG pressure	$P_{initial}$	106 kPa	
Time step	$\Delta t$	0.1 s	Selected based on the results at 0.01-, and 0.1-s time steps

In the experiment conducted by Ludwig et al. [90], the tank was initially pressurized by injecting gaseous nitrogen at 294 K to the vapor space of the tank for 53 s until the tank pressure reached 300 kPa. Then, the inlet valve to the tank was shut off. The relaxation phase took 147 s until the tank pressure decreased to 246 kPa due to the condensation of gaseous nitrogen in contact with the liquid nitrogen. Ludwig et al. [90] measured the temperature profiles of liquid and gaseous nitrogen inside the tank. The locations of thermocouples depicted in Figure 3.2 are provided in Table 3.3.

**Table 3.3. Radial and axial locations for the thermocouples inside the vertical nitrogen tank [90].**

<b>Thermocouple number</b>	<b>Radial (x) [m]</b>	<b>Axial (z) [m]</b>
T1	0.0980	0.460
T2	0.0980	0.510
T3	0.0980	0.610
T4	-0.1480	0.450
T5	-0.1480	0.630
T6	0.0063	0.644
T7	0.0980	0.445

In the equilibrium thermodynamic model, the initial temperatures of the liquid and vapor phases are set at 77.8 K to correspond to the initial saturation pressure of the tank at 106 kPa. In the non-equilibrium thermodynamic modelling, the initial liquid temperature is set at 77.7 K based on the measured temperatures by thermocouple T7 installed in the liquid nitrogen space. To calculate the average temperature in the vapor space based on the readings of thermocouples T1, T2, T3, and T6, the specific enthalpies at these locations are calculated. Then, a polynomial curve is fitted to the calculated specific enthalpies along the tank axial direction ( $z$ -direction). Similarly, the density of the gaseous nitrogen is calculated from the experimental temperature and pressure data. Using

the polynomial curves of the specific enthalpy and density, the average mass enthalpy in the vapor space of the tank is calculated:

$$\bar{h}_v = \frac{\int_0^{L_v} h(z) \rho(z) \left( \frac{\pi D_i^2}{4} \right) dz}{\int_0^{L_v} \rho(z) \left( \frac{\pi D_i^2}{4} \right) dz} \quad (3-1)$$

Accordingly, the initial vapor temperature is calculated (150.9 K) from the tank pressure and average mass enthalpy of the vapor.

Ludwig et al. [90] embedded the tank in a vacuum to improve the insulation except for the top lid. Considering the short period of the experiment (200 s), an adiabatic boundary condition is set at the tank wall. The convection heat transfer coefficient on the lid is calculated based on the empirical correlations of external free convection on a horizontal flat plate (Eqs. (2-30), (2-31), and (2-32)). The thickness of the tank lid,  $t_{lid}$ , is assumed to be 3 mm, and the thermal conductivity of the tank lid,  $k_{lid}$ , is assumed to be 14.56 W/m·K at 282 K [91].

Figure 3.3 shows the pressure and temperature profiles calculated using the equilibrium thermodynamic, non-equilibrium thermodynamic, and CFD models, and compared against the experimental data of Ludwig et al. [90]. The computational domain and CFD model are developed by using Ansys ICEM CFD and Ansys Fluent software, respectively [92]. Figure 3.3(a) illustrates that the non-equilibrium thermodynamic and CFD models predict the tank pressure similarly. The tank pressure calculated by the non-equilibrium thermodynamic model has a good agreement with the experimental data with the maximum relative difference of 3.1%. In contrast, the pressure

profile calculated by using the equilibrium thermodynamic model is not able to predict the sudden pressure rise in the tank.

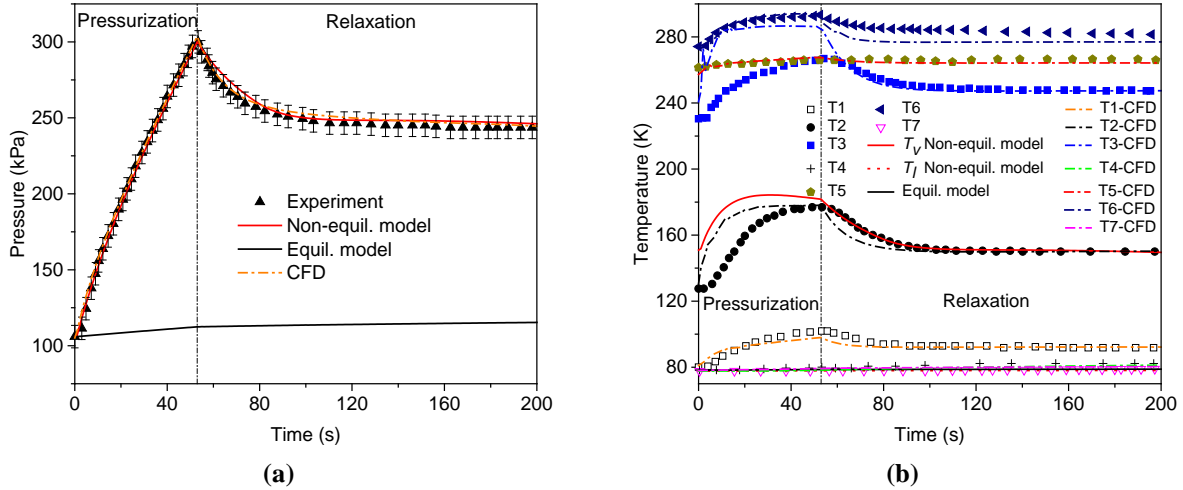


**Figure 3.3. Comparison of equilibrium thermodynamic, non-equilibrium thermodynamic, and CFD models against the experimental data of Ludwig et al. [90]: (a) Tank pressure and (b) temperature profiles in the vapor and liquid nitrogen.**

Figure 3.3(b) shows that the temperature profiles of liquid nitrogen calculated by the equilibrium thermodynamic, non-equilibrium thermodynamic and CFD models have a good agreement with the experimental data (thermocouples T4 and T7 in Figure 3.2). However, the equilibrium thermodynamic model fails to predict the vapor temperature during the pressurization and relaxation processes.

During the pressurization process, Figure 3.3(b) shows that the average temperature of the vapor phase predicted by the non-equilibrium thermodynamic model is between the temperatures measured by thermocouples T2 and T3. During the relaxation process, the non-equilibrium thermodynamic model gives the average temperature of the vapor phase close to thermocouple T2 which is located almost at the center of the vapor space as shown in Figure 3.2. The CFD model

provides more details on the temperature distribution in the vapor phase. However, due to the complexity of the flow field during the pressurization phase, the difference among the temperature profiles calculated by the CFD model and experimental data is larger during the pressurization phase rather than those in the relaxation phase.

Although the CFD model can predict the temperature and pressure profiles, the computational time required for the physical time of 200 s is about 4 hours (CPU: Intel i7-7700K and RAM: 64 GB). This long computation time illustrates that using the CFD model is not practical to investigate the thermal performance of storage tanks holding LNG for a few days, weeks, or months.

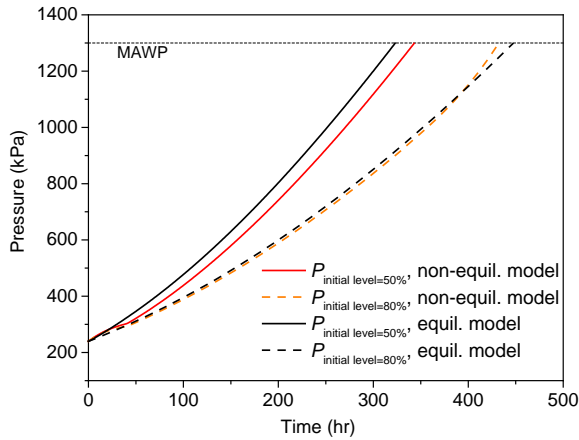
### **3.2 Base-case model analysis**

In this section, the performance of two identical vertical and horizontal LNG storage tanks installed in refueling stations is studied. Table 3.4 shows the specs, boundary and initial conditions of these storage tanks. The tanks are initially filled to 50% and 80% of their capacity. For safety reasons and to accommodate the thermal expansion of LNG due to the heat transfer, LNG storage tanks in refueling stations are filled up to 85% of their capacity [93]. In the case of underutilization of LNG refueling stations, e.g., a limited number of LNG-fueled trucks in a region, the storage tanks are not completely filled. The MAWP of these storage tanks is set at 1,300 kPa, and beyond this pressure, safety valves installed on the storage tanks are activated.

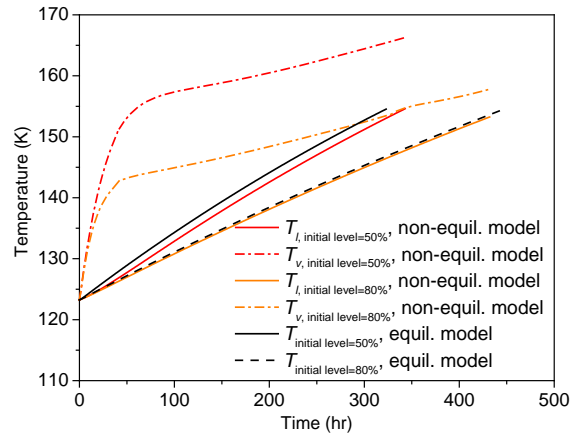
**Table 3.4. Specs of vertical and horizontal LNG storage tanks, and boundary and initial conditions.**

<b>Parameters</b>	<b>Value</b>	<b>Description</b>
Tank net capacity, $V_{tank}$	57.2 m <sup>3</sup>	Ref. [94]
Length of inner tank, $L_{tank}$	12.64 m	Ref. [94]
Outer diameter, $D_o$	2.896 m	Ref. [94]
Inner diameter, $D_i$	2.4 m	Ref. [94]
Mass of the tank (empty), $m_{tank}$	21,455 kg	Ref. [94]
Specific heat capacity of tank, $c_{p,tank}$	477 J/kg·K	Assumed from stainless steel 304
Surface area of inner tank, $A_{tank}$	104.35 m <sup>2</sup>	Calculated from inner tank geometry
Conductivity of insulation material, $k_{insulation}$	0.021 W/m·K	Vacuum Polyurethane insulated tank [95]
Ambient temperature, $T_{air}$	298.15 K	Assumed
Maximum allowable working pressure of storage tank (MAWP)	1,300 kPa	Ref. [96]
<b>Initial conditions</b>		
Liquid phase temperature, $T_{l,initial}$	123.2 K	Assumed
Vapor phase temperature, $T_{v,initial}$	123.2 K	Assumed
LNG tank pressure, $P_{initial}$	240 kPa	Correspond to the saturation pressure at the liquid phase temperature
Inner tank wall temperature	123.2 K	Assumed
Outer tank wall temperature	298.15 K	Set at the ambient temperature
Time step (stationary LNG storage tanks), $\Delta t$	60 s	Selected based on the results at 30-, 60-, and 120-s time steps
Time step (stationary LNG storage tanks), $\Delta t$	15 s	Selected based on the results at 15- and 30-s time steps

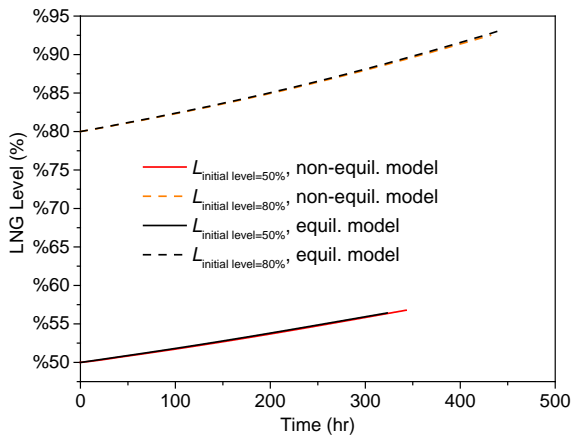
Figure 3.4 shows the performance of the vertical LNG storage tank at 50% and 80% LNG filling levels. Figure 3.4(a) shows that the equilibrium and non-equilibrium thermodynamic models predict the pressure increase of the tank similarly. The tank filled to 50% of its capacity has a shorter holding time than that filled to 80%. This is due to the lower thermal mass of LNG in the storage tank filled to 50%, and consequently, faster evaporation of LNG. Figure 3.4(b) demonstrates that the temperature profiles calculated by the equilibrium thermodynamic model fall between the liquid and vapor temperature profiles calculated by the non-equilibrium thermodynamic model. Also, Figure 3.4(b) indicates that the liquid and vapor temperature gradient can be as high as 25 K for the storage tank initially filled to 50% of its net capacity.



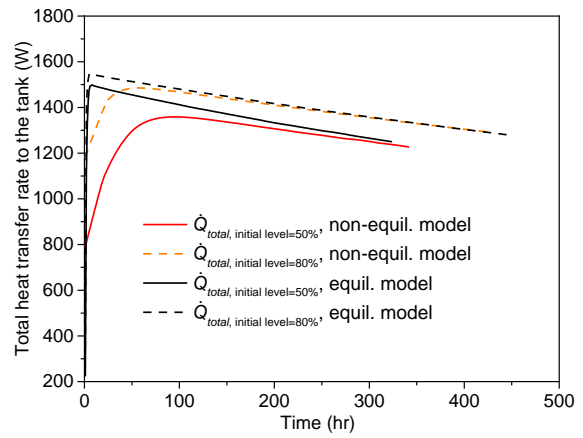
(a)



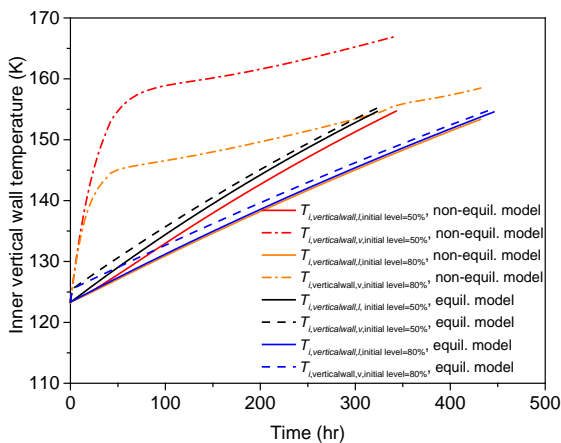
(b)



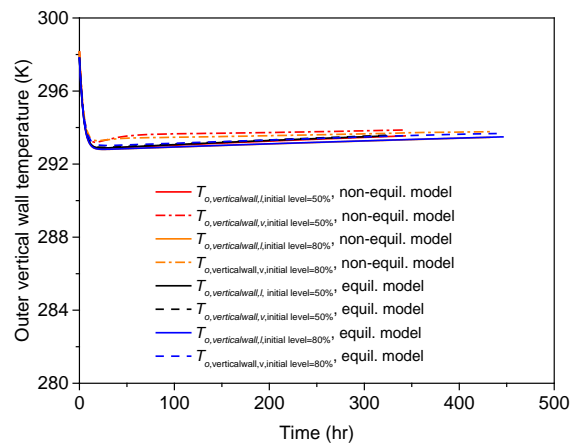
(c)



(d)



(e)



(f)

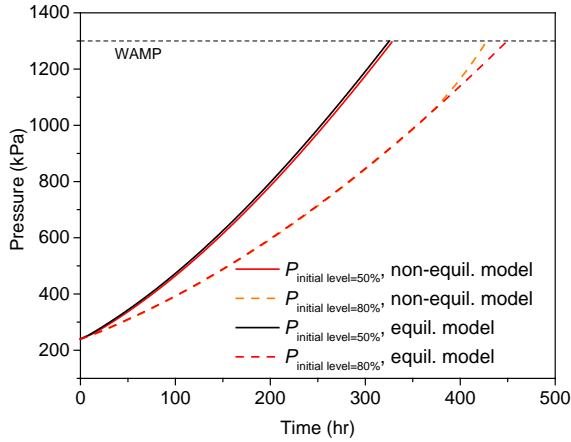
**Figure 3.4. Thermal performance of the vertical LNG storage tank at 50% and 80% initial LNG filling levels: (a) pressure, (b) temperature, (c) LNG level, (d) total heat transfer rate to the storage tank, (e) inner vertical wall temperature, and (f) outer vertical wall temperature.**

The changes in the LNG level in the tank due to the heat transfer are shown in Figure 3.4(c). The equilibrium and non-equilibrium thermodynamic models predict a similar LNG level increase. As LNG temperature increases, its density decreases leading to an increase in the LNG level. For the vertical storage tank with the initial LNG filling levels of 50% and 80%, the final LNG levels increase to 56% and 93%, respectively.

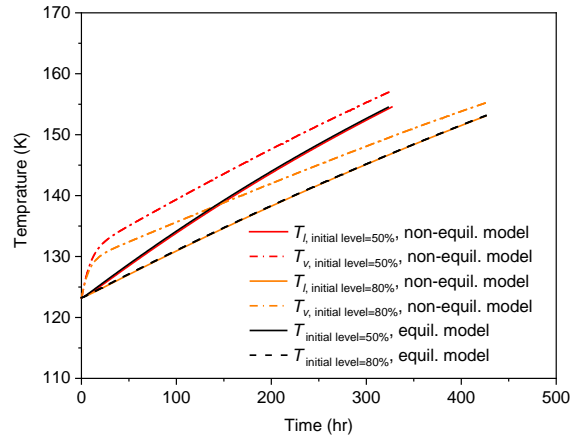
Figure 3.4(d) displays the total heat transfer rate to the vertical LNG storage tank. The total heat transfer rate to the tank is the summation of the heat transfer rates to the liquid and vapor phases calculated from Eqs. (2-22) and (2-23). In this study, the same initial temperatures are set at the inner tank wall, and vapor and liquid phases (shown in Table 3.4). Therefore, the initial total heat transfer rates calculated by using the equilibrium and non-equilibrium thermodynamic models are equal to zero. As the temperatures of LNG, vapor, and tank walls change, the heat transfer rate gradually increases. Figure 3.4(d) indicates that the total heat transfer rate to the tank calculated by using the equilibrium and non-equilibrium thermodynamic models are different during the first 100 hrs and as time passes, the total heat transfer rates to the tank merge together. Within the first 100 hrs, the vapor temperature calculated by the non-equilibrium thermodynamic model increases (e.g., up to 25 K more than the LNG temperature as shown in Figure 3.4(b)) leading to a lower heat transfer rate to the vapor space of the tank than that calculated by using the equilibrium thermodynamic model. This results in a lower total heat transfer rate to the tank predicted by the non-equilibrium thermodynamic model. After the first 100 hrs, the vapor and LNG temperature gradient calculated by the non-equilibrium thermodynamic model decreases. Therefore, the total heat transfer rate to the tank calculated by the non-equilibrium thermodynamic model becomes similar to that calculated by the equilibrium thermodynamic model.

Figure 3.4(e) and (f) display the inner and outer vertical wall temperatures in the vertical LNG storage tank, respectively. The inner vertical wall temperature has a similar trend to the temperature profiles of vapor and liquid phases showed in Figure 3.4(b). The temperature difference between the inner vertical wall in contact with the vapor phase and the bulk vapor is about 2 K. This temperature difference in the liquid part is about 0.1 K due to the stronger convection heat transfer along the vertical walls in contact with the liquid phase than those in contact with the vapor phase. The outer vertical wall temperature does not change significantly as shown in Figure 3.4(f) except the first few hours which is affected by the initial temperature set on the outer vertical wall.

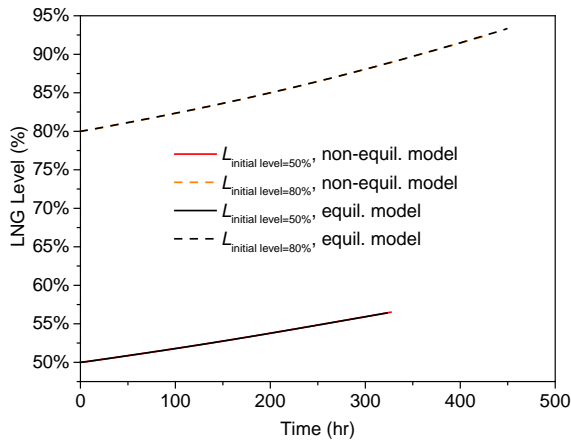
Figure 3.5 shows the performance of the horizontal LNG storage tank at 50% and 80% LNG filling levels. It can be seen that the trends of pressure, temperature, LNG level, total heat transfer rate, and inner and outer wall temperatures in the horizontal tank are similar to those in the vertical LNG storage tank. However, Figure 3.5(b) shows a smaller temperature gradient between the vapor and LNG in the horizontal tank. This is due to the larger vapor-liquid interface in the horizontal tank than that in the vertical tank and, therefore, a higher heat transfer rate between the LNG and vapor phase.



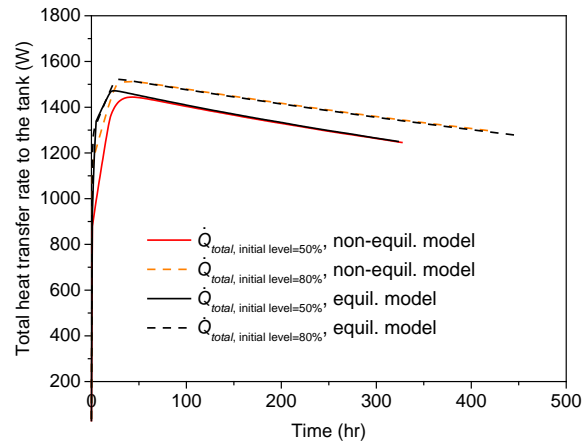
(a)



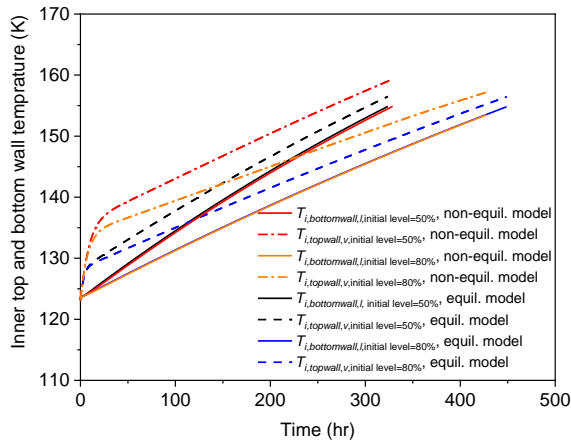
(b)



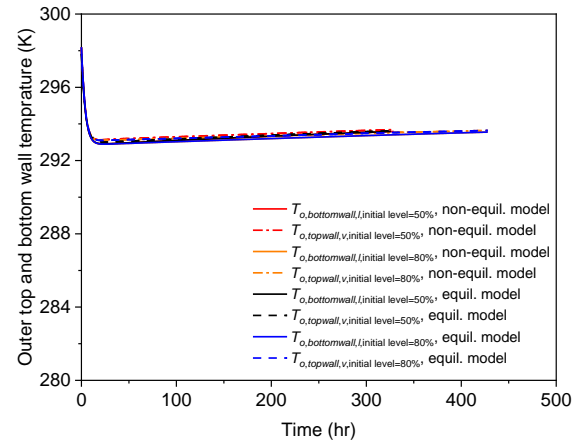
(c)



(d)



(e)



(f)

**Figure 3.5. Thermal performance of the horizontal LNG storage tank at 50% and 80% initial LNG filling levels: (a) pressure, (b) temperature, (c) LNG level, (d) total heat transfer rate to the storage tank, (e) inner top and bottom wall temperatures, and (f) outer top and bottom wall temperatures.**

The average daily BOG generation rate is calculated by

$$BOG = \frac{m_{evap}}{m_{l \text{ at } t=0} t_{holding \text{ time}}} \times 24 \times 100 [\%/day] \quad (3-2)$$

where,  $m_{evap}$  is the amount of the mass of the evaporated vapor phase (kg), and  $m_{l \text{ at } t=0}$  is the initial mass of the LNG in the tank (kg).  $t_{holding \text{ time}}$  is the storage tank holding time (hr) until the pressure reaches the tank MAWP without venting.

In this situation, the LNG storage tank is kept closed. No vapor gas is released from the LNG storage tank, or returned to the tank. Therefore,  $\Delta m_v$ , the changes in the initial and final masses of the vapor phase (kg), is equal to  $m_{evap}$ . Therefore, the average daily BOG generation rate can be expressed as,

$$BOG = \frac{\Delta m_v}{m_{l \text{ at } t=0} t_{holding \text{ time}}} \times 24 \times 100 [\%/day] \quad (3-3)$$

Figure 3.6 shows the holding time and average daily BOG generation rate of the vertical and horizontal LNG storage tanks calculated by using the equilibrium and non-equilibrium thermodynamic models. The vertical and horizontal tanks with 50% filling level have a shorter holding time and a larger BOG generation rate than those with 80% filling level. Therefore, a higher filling level in the tank helps to increase the holding time and decrease the average daily BOG generation rate. Figure 3.6 indicates that both equilibrium and non-equilibrium thermodynamic models predict similar holding time and BOG generation rates for vertical and horizontal storage tanks under stationary conditions.

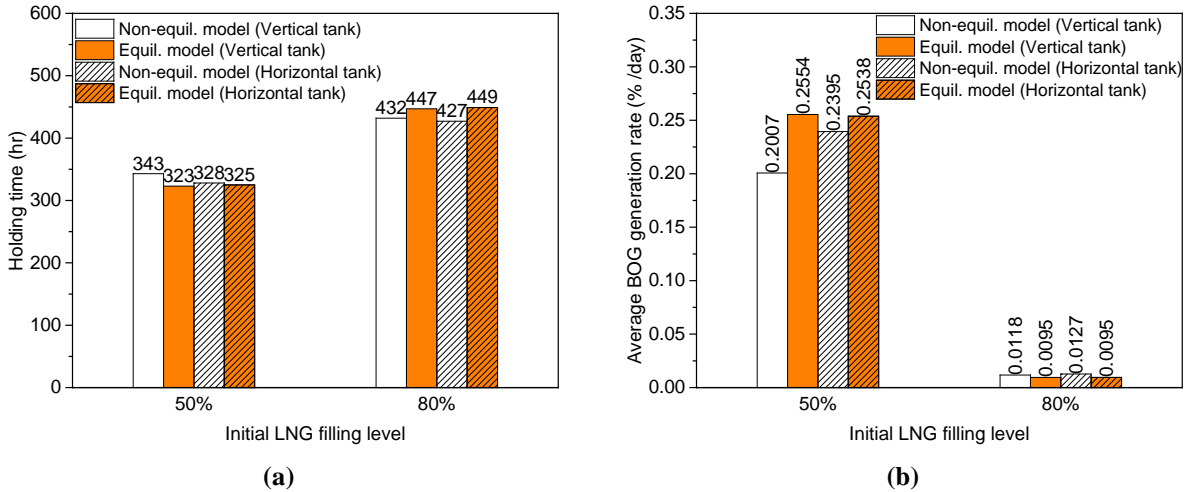


**Figure 3.6. (a) Holding time and (b) average daily BOG generation rate of the vertical and horizontal LNG storage tanks calculated by using the equilibrium and non-equilibrium thermodynamic models at the base-case conditions given in Table 3.4.**

### 3.3 Performance of LNG storage tanks in refueling stations during truck refueling

In this study, LNG dispensing to heavy-duty trucks with two  $0.454\text{-m}^3$  (120-gal) onboard tanks is considered. It is assumed that the heavy-duty trucks are filled when the LNG level in their onboard tanks reaches 20%. At this condition, the average pressure of onboard tanks is 1,273 kPa (170 psig). Before starting the refueling process, the pressure of onboard tanks is reduced by returning the extra vapor to the LNG refueling station. This process takes 2 minutes. Then, the refueling process starts and continues until the LNG level in the onboard tanks reaches 90%. The refueling process takes 10 minutes. A 5-minute interval is assumed between refueling two trucks. The fuel dispensing to trucks is continued daily until the LNG level in the storage tank goes below 20%.

To reduce the pressure of a truck's onboard tank before starting the refueling process, the extra vapor in the onboard tank should be returned to the refueling station. In this study, it is assumed that the pressure of the onboard tank is decreased from 1,273 kPa (170 psig) to 1,135.5 kPa (150 psig) (Process 1), and from 1,273 kPa (170 psig) to 652.9 kPa (80 psig) (Process 2). These

processes are selected based on our observation of operational LNG refueling stations. The average vapor return rate to the refueling station (kg/s) is calculated by

$$\dot{m}_{BOG} = \frac{(\rho_{v,P_i} - \rho_{v,P_f}) \times 2 \times 0.8 \times \forall_{truck\ tank}}{\Delta t_{BOG}} \quad (3-4)$$

where,  $\rho_{v,P_i}$  and  $\rho_{v,P_f}$  are the vapor densities (kg/m<sup>3</sup>) at the initial (1,273 kPa) and final pressures of the onboard tanks, respectively.  $\Delta t_{BOG}$  is the vapor return process duration (2 minutes) and  $0.8 \times \forall_{truck\ tank}$  is the volume of vapor space of an onboard tank (m<sup>3</sup>). Based on Eq. (3-4), the average vapor return rates for Processes 1 and 2 equal 0.0023 and 0.0743 kg/s, respectively.

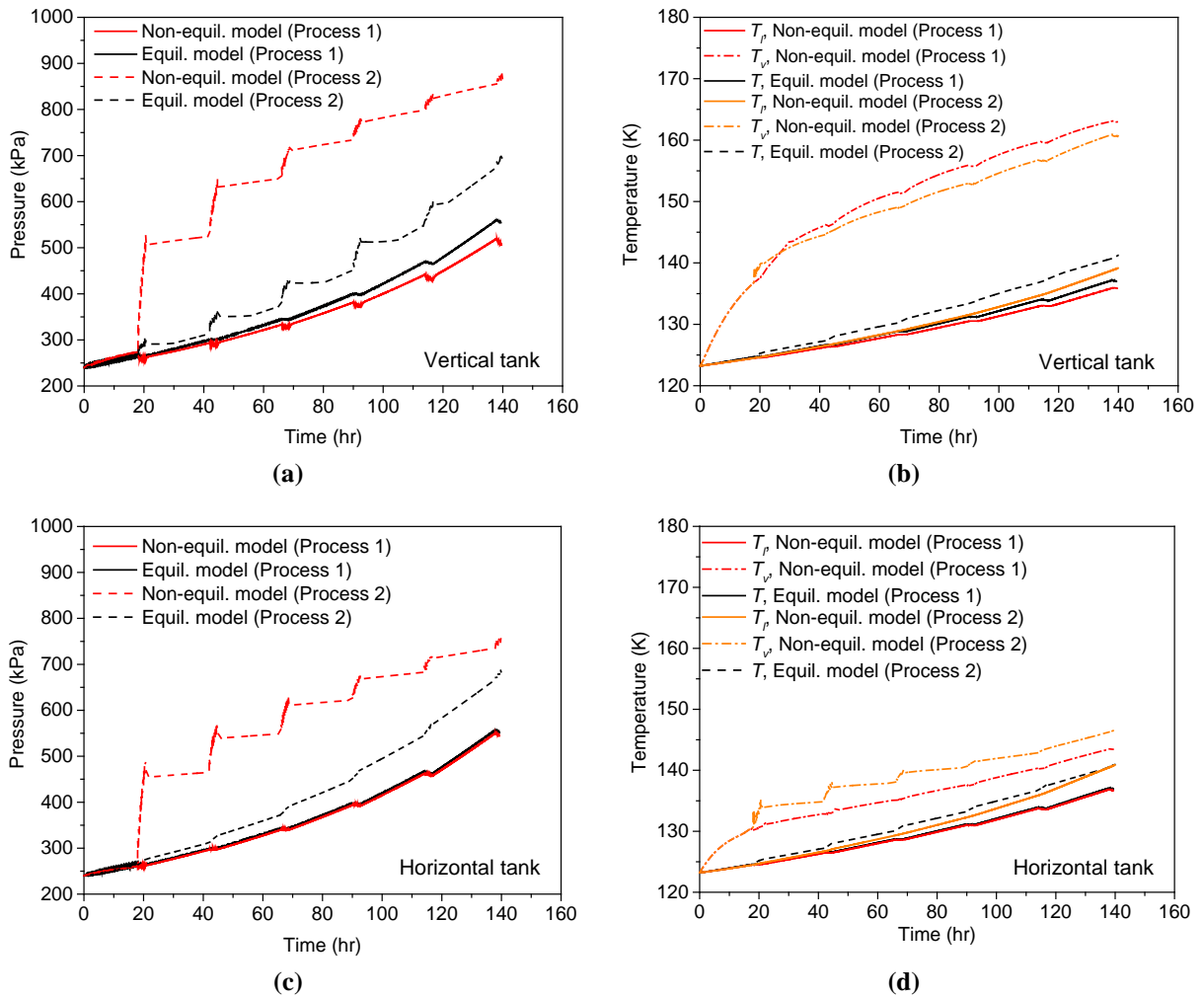
The average LNG refueling rate (kg/s) pumped to the onboard tanks is calculated by

$$\dot{m}_{LNG} = \frac{\rho_{LNG} \times 2 \times 0.7 \times \forall_{truck\ tank}}{\Delta t_{LNG}} \quad (3-5)$$

where,  $0.7 \times \forall_{truck\ tank}$  is the volume of LNG filled in an onboard tank (m<sup>3</sup>) (from 20% to 90% of its capacity) and  $\Delta t_{LNG}$  is the duration of LNG refueling process (10 minutes). Based on Eq.(3-5), the average LNG refueling rate equals 0.4243 kg/s for both Processes 1 and 2.

To study the performance of the vertical and horizontal LNG storage tanks in a refueling station under dynamic operating conditions, fleets of 10 and 20 heavy-duty trucks are considered. Figure 3.7 shows the pressure and temperature changes inside the vertical and horizontal storage tanks calculated by using the equilibrium and non-equilibrium thermodynamic models for the fleet of 10 heavy-duty trucks.

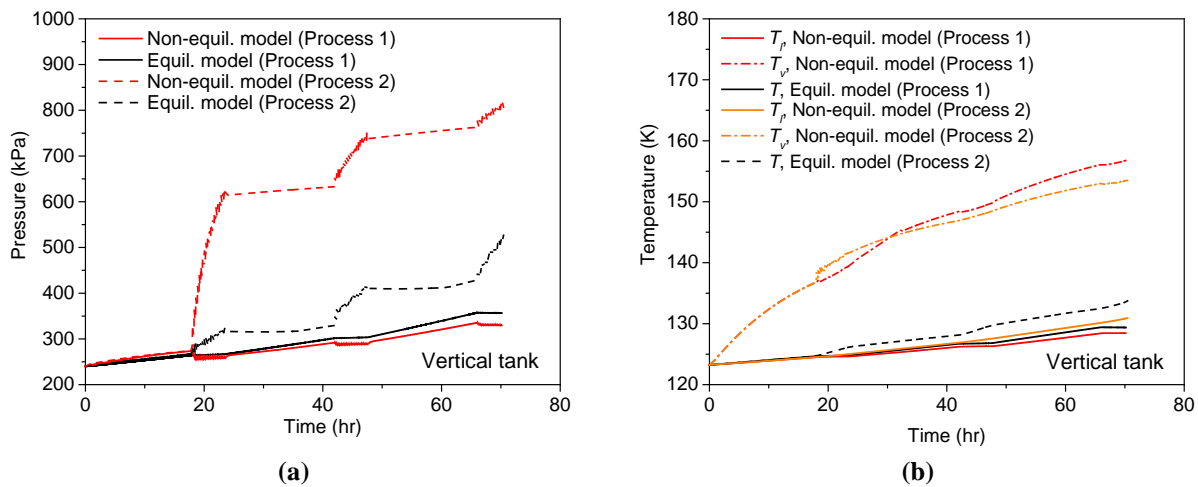
Figure 3.7(a) and (c) show that the pressure rise in the vertical and horizontal tanks is affected by the heat transfer from the environment and vapor return from trucks' onboard tanks. Figure 3.7(a) and (c) highlight the failure of the equilibrium thermodynamic model to predict the pressure increase in the vertical and horizontal storage tanks due to vapor return from trucks' onboard tanks. This is consistent with the conclusion made in the model validation of a storage tank under the pressurization process discussed in Section 3.1.2. In contrast, the non-equilibrium thermodynamic model responds to the sudden pressure rise in the tanks due to the vapor return process.



**Figure 3.7. Changes in the pressure and temperature of (a, b) vertical storage tank and (c, d) horizontal storage tank to fuel the fleet of 10 trucks.**

According to the results of the non-equilibrium thermodynamic modelling shown in Figure 3.7, it can be concluded that the horizontal storage tank has a better performance than the vertical storage tank in condensing the vapor returned from trucks. Due to having a larger vapor-liquid interface, the pressure increase, and the temperature gradient between liquid and vapor phases in the horizontal storage tank are smaller than those in the vertical storage tank after about 140 hrs (~ 6 days) of operating the refueling station. Also, Figure 3.7 indicates that Process 2 (in which the pressure in the onboard tanks is decreased more than Process 1) does not increase the storage tank pressure in refueling stations beyond the tank’s MAWP (1,300 kPa.)

Figure 3.8 shows the pressure and temperature increase in the vertical and horizontal storage tanks when dispensing fuel to the fleet of 20 trucks. Similar to the results of the non-equilibrium thermodynamic modelling shown in Figure 3.7, the horizontal storage tank has better performance than the vertical storage tank. It maintains the tank pressure low by condensing the vapor returned from heavy-duty trucks at a higher rate.



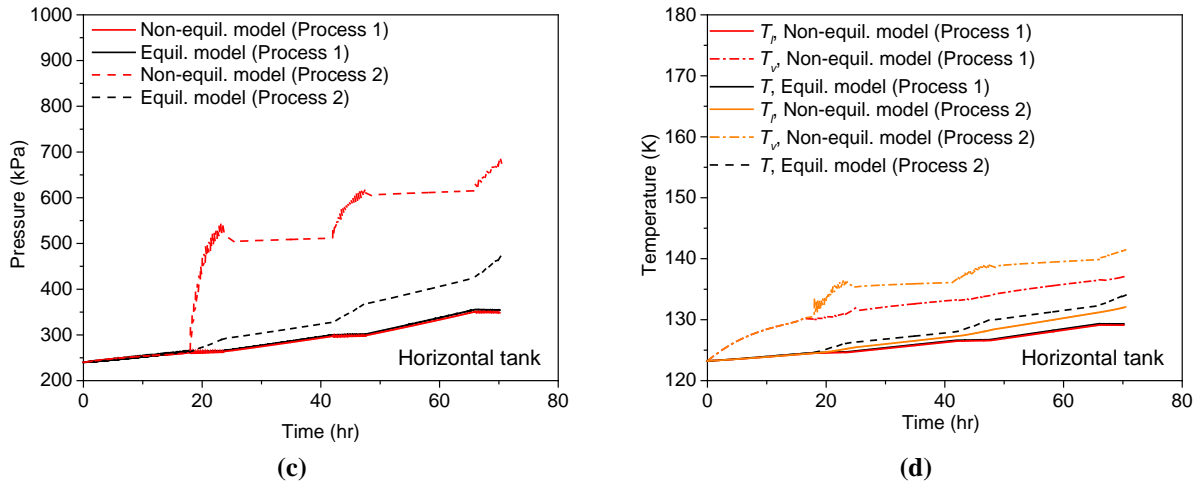


**Figure 3.8. Changes in the pressure and temperature of (a, b) vertical storage tank and (c, d) horizontal storage tank to fuel the fleet of 20 trucks.**

This finding suggests that for refueling stations, where space is not a concern, horizontal storage tanks provide a lower operating pressure and longer LNG holding time than vertical storage tanks.

### 3.4 Summary

This chapter validated the non-equilibrium thermodynamic model applied to vertical and horizontal tanks. The chapter included a comparison between the equilibrium and non-equilibrium thermodynamic models with a parametric study for a base-case tank. The thermal performance of the vertical and horizontal tanks was compared. Analyzing the thermal performance of LNG storage tanks illustrated the advantages and applications of the non-equilibrium thermodynamic model over the equilibrium thermodynamic model.

## **Chapter 4: Results from Non-equilibrium Multilayer Thermodynamic**

### **Modelling**

#### **4.1 Model validation**

The non-equilibrium multilayer thermodynamic model is employed to model the La Spezia rollover incident reported by Sarsten [26]. This incident occurred in SNAM LNG Terminal in La Spezia, Italy, on August 21, 1971. The thermal stratification occurred after the tank was loaded with fresh LNG (cargo) with a different composition from the leftover LNG (heel) in the tank (Figure 4.1). The rollover occurred when the tank experienced a sudden pressure increase which led to the BOG discharge through the tank safety valves. The La Spezia incident arouses questions on what the key factors in the rollover phenomenon were, and what safety measures should be considered in the design and operation of LNG storage tanks. The geometry, and initial and boundary conditions in the La Spezia rollover incident are summarized in Table 4.1, Table 4.2, and Table 4.3, respectively.

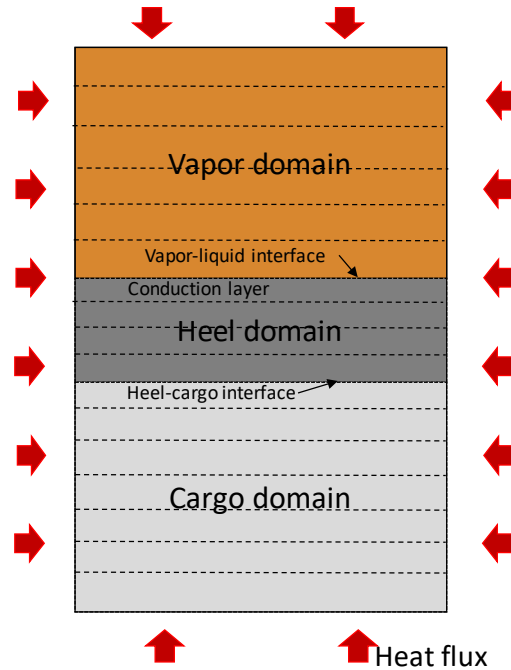


Figure 4.1. A schematic of the LNG storage tank in the La Spezia rollover incident in 1971.

Table 4.1. The tank geometry in the La Spezia rollover incident [26].

Parameter	Symbols	Values	Remark
Tank inner diameter	$D_i$	49.08 m	
Tank height	$H$	43.28	
Tank cross-sectional area	$A_{cross}$	1891.90 m <sup>2</sup>	Calculated based on $D_i$

Table 4.2. Initial composition of LNG and vapor phase [27], LNG level, pressure, as well as the temperature and densities of LNG in the heel and cargo layers, and the vapor phase.

Components	Heel layer (top)	Cargo layer (bottom)	Vapor phase
	Initial mole fraction %		
Methane (CH <sub>4</sub> )	63.62	62.26	95.00
Ethane (C <sub>2</sub> H <sub>6</sub> )	24.16	21.85	0.00
Propane (C <sub>3</sub> H <sub>8</sub> )	9.36	12.66	0.00
<i>n</i> -Butane (C <sub>4</sub> H <sub>10</sub> )	2.51	3.21	0.00
Nitrogen (N <sub>2</sub> )	0.35	0.02	5.00
<i>Initial conditions</i>			
Temperature (K)	114.36	119.0	122.04
Pressure (kPa)	103.78	103.78	103.78
Space height (m)	5.03	17.83	20.42
Density(kg/m <sup>3</sup> )	534.11	538.04	1.746
(based on PR-EoS)			

**Table 4.3. The thermal boundary conditions on the tank in the La Spezia rollover incident [27].**

<b>Parameter</b>	<b>Symbols</b>	<b>Values</b>
Heat flux rate from the tank bottom wall to the cargo layer	$\dot{q}_b''$	20.82 W/m <sup>2</sup>
Heat flux rate from the tank side walls to the LNG in the heel and cargo layers	$\dot{q}_{l,wall}''$	6.94 W/m <sup>2</sup>
Heat flux rate from the tank side walls to the vapor phase	$\dot{q}_{v,wall}''$	6.94 W/m <sup>2</sup>
Heat flux rate from the tank top wall to the vapor phase	$\dot{q}_t''$	15.77 W/m <sup>2</sup>

To test the mesh independence of the non-equilibrium multilayer thermodynamic model, four mesh sizes were tested: (1) 15 cells in the heel and cargo layers, and 7 cells in the vapor phase, (2) 20 cells in the heel and cargo layers, and 10 cells in the vapor phase, (3) 30 cells in the heel and cargo layers, and 15 cells in the vapor phase, and (4) 40 cells in the heel and cargo layers, and 20 cells in the vapor phase.

Figure 4.2 shows the changes in the densities of LNG at the heel-cargo interface. In this analysis, the rollover occurs when the densities of LNG adjacent to the heel-cargo interface equalize and the interface becomes unstable.

The numerical results in Figure 4.2 show that the model predicts the LNG densities adjacent to the heel-cargo interface independent from the mesh sizes. The model predicts that the rollover occurs after 18.2-23 hours compared with the experimental rollover time of 18 hours (the relative difference is 1-28%) [26].

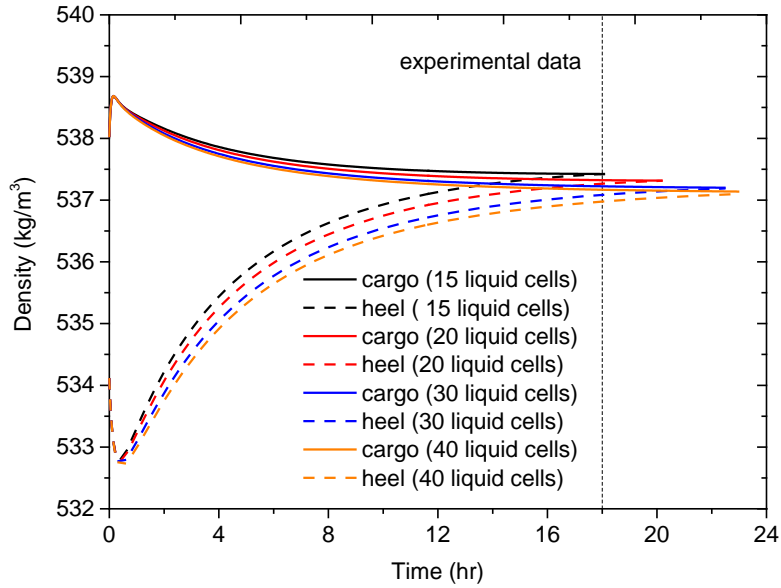
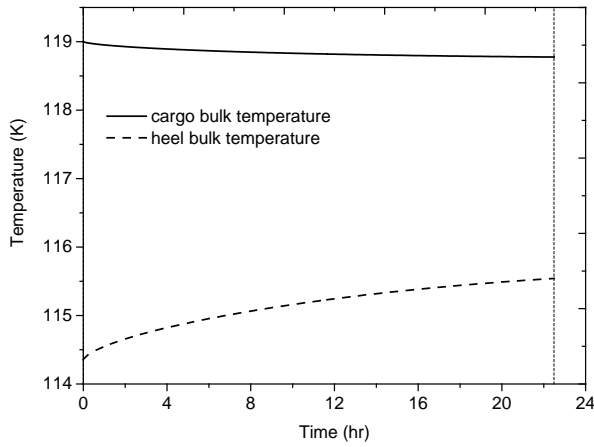
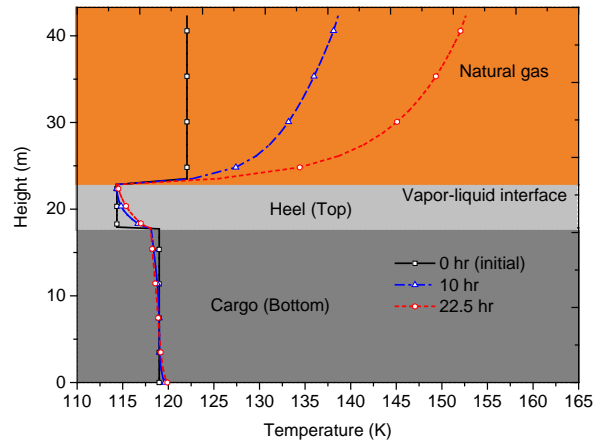


**Figure 4.2. Changes in the LNG densities adjacent to the heel-cargo interface over time calculated by the non-equilibrium multilayer thermodynamic model and compared against the experimental rollover time [26].**

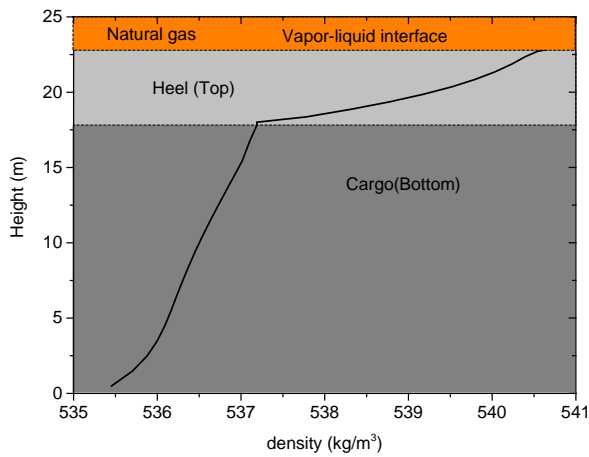
Figure 4.3(a) and (b) show further details about the changes in the LNG and vapor temperatures in the tank over time. In Figure 4.3, 30 cells in the heel and cargo layers, and 15 cells in the vapor phase are employed. Figure 4.3(a) shows that while both heel and cargo receive heat from the tank walls, the cargo bulk temperature decreases over time due to the heat transfer from the cargo layer to the heel layer.



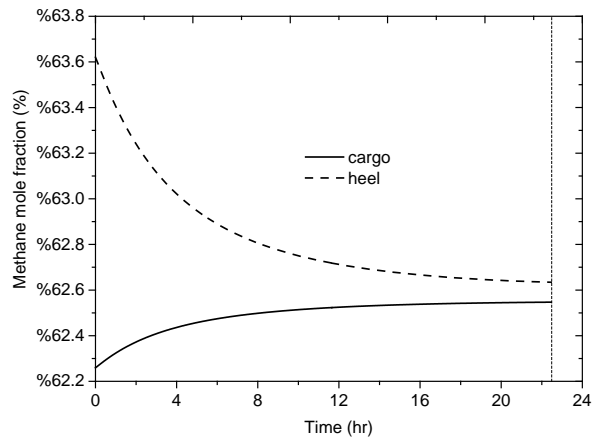
(a)



(b)



(c)



(d)

**Figure 4.3. (a) LNG temperature profiles in the cargo and heel layers, (b) temperature distribution and thermal stratification in the tank over time, (c) LNG density profiles in the cargo and heel layers at the rollover start time, and (d) changes in the methane ( $\text{CH}_4$ ) mole fraction in the cargo and heel layer over time.**

The changes in the temperatures of the cargo, heel, and vapor phase are shown in Figure 4.3(b). The results indicate that the LNG temperature at the bottom of the cargo layer increases over time due to heat transfer from the tank bottom wall, and the LNG temperature at the cargo near the heel-cargo interface decreases over time due to heat transfer to the heel layer. The results in Figure 4.3(b) indicate that the heel bulk temperature increases over time. However, the LNG temperature

in the heel near the vapor-liquid interface remains constant because the LNG bubble temperature in atmospheric LNG storage tanks does not change. The numerical results in Figure 4.3(b) demonstrate that the thermal stratification in the vapor phase is stronger than the liquid phase because of the lower thermal conductivity and thermal mass of gaseous natural gas than those of the LNG.

The LNG density profile in the heel and cargo layers at the rollover start time (22.5 hours) is shown in Figure 4.3(c). In the cargo, the LNG density increases from the bottom to the heel-cargo interface, which inversely correlates to the temperature profile shown in Figure 4.3(b). In the heel, the LNG density is equal to that in the cargo at the heel-cargo interface, which explains why the rollover occurs, and increases at the vapor-liquid interface due to the LNG evaporation.

Figure 4.3(d) shows the changes in the methane ( $\text{CH}_4$ ) mole fraction in the heel and cargo layers over time. Methane ( $\text{CH}_4$ ) has the lowest boiling pressure among hydrocarbons in the LNG mixture. Therefore, it evaporates faster than other species, e.g., ethane, propane, etc. Figure 4.3(d) indicates that the methane mole fraction in the heel layer decreases over time due to the preferential evaporation of methane at the vapor-liquid interface, and the mass transfer between the heel and cargo layers. The methane mole fraction gradually increases in the cargo.

## **4.2 Parametric study on the rollover start time**

In this section, the effects of the heat flux rate along the tank wall, cargo to heel height ratio, and the tank dimensions on the rollover are investigated. Table 4.4 shows the LNG composition and

initial conditions in the LNG storage tank. The tank geometry is similar to that in the La Spezia rollover incident (shown in Table 4.1).

**Table 4.4. The initial LNG and gaseous natural gas compositions, temperatures, and densities used for the parametric study.**

<b>Components</b>	<b>Heel layer (top)</b>	<b>Cargo layer (bottom)</b>	<b>Vapor phase</b>
	<b>mole fraction% [97]</b>		
Methane CH <sub>4</sub>	97.50	92.60	89.00
Ethane C <sub>2</sub> H <sub>6</sub>	2.00	6.47	0.00
Propane C <sub>3</sub> H <sub>8</sub>	0.00	0.46	0.00
Nitrogen N <sub>2</sub>	0.50	0.47	11.00
<i>Initial conditions</i>			
Temperature (K)	111.2	115.2	114.0
Pressure (kPa)	108	108	108
Space height (m)	5.00	15.00	23.28
Density (kg/m <sup>3</sup> )	430.28	440.29	2.04

#### **4.2.1 Effect of heat transfer rate to the tank on the rollover start time**

The heat flux rates on the tank walls given in Table 4.3 are considered as the base-case condition. Figure 4.4 shows the effect of heat transfer rates from the environment to the tank walls on the rollover start time at the base-case heat flux rates (shown in brief with  $\dot{q}''$ ) and when they are multiplied by 0.5, 2, and 3. The numerical results indicate that in an atmospheric tank, the heat flux rates do not significantly affect the temperatures of the heel and cargo layers over time (Figure 4.4(a)). However, the higher heat flux rates increase the LNG evaporation rate, and BOG generation (Figure 4.4(b)). The extra BOG should be removed from the tank to maintain the tank pressure close to the atmospheric pressure. Also, the results shown in Figure 4.4(c) and (d) indicate that the amount of heat transfer to the atmospheric LNG storage tank does not significantly affect the rollover start time (less than 7%).

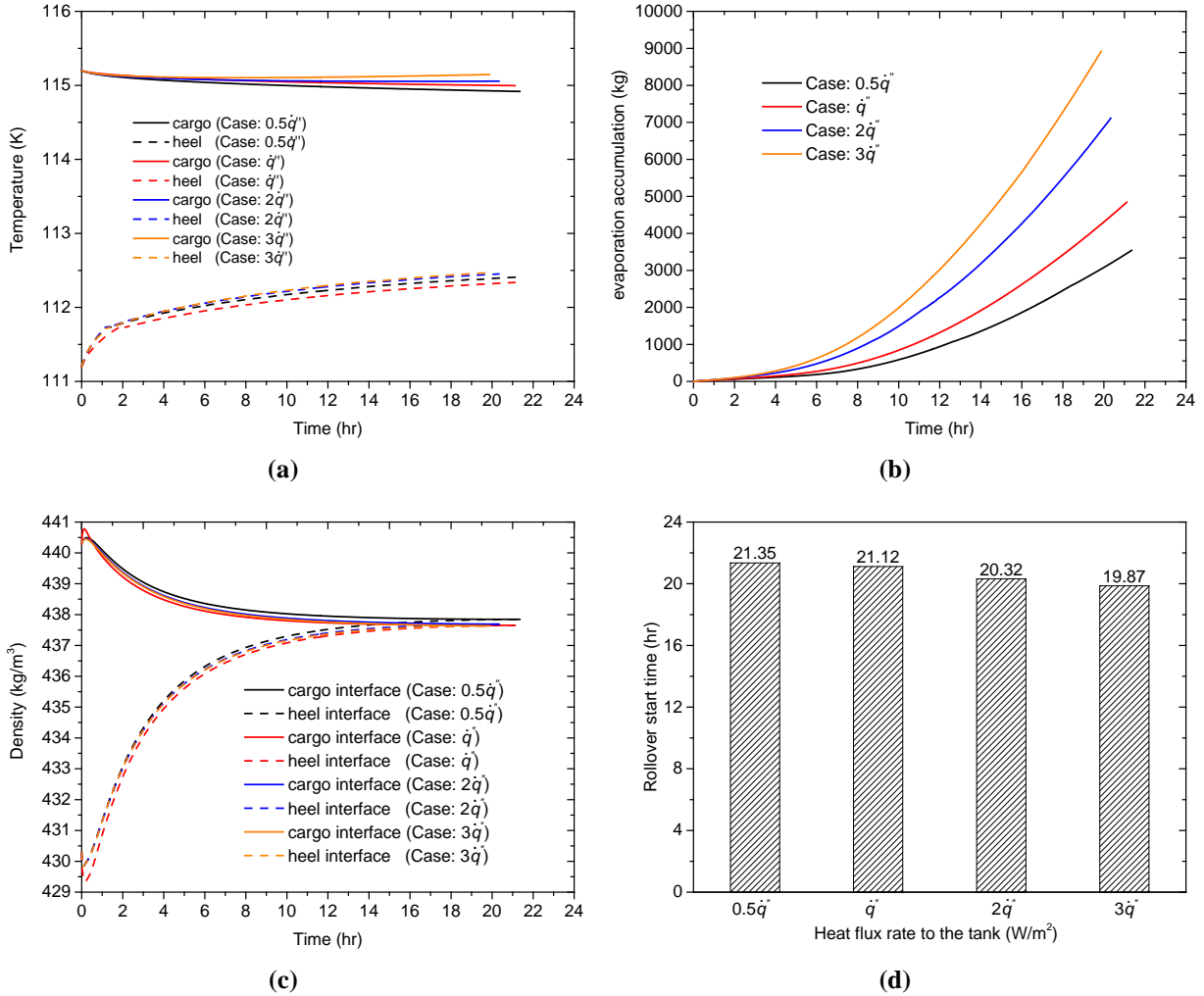


**Figure 4.4. Effect of heat transfer rate from the environment to the LNG storage tank on the rollover start time: (a) bulk temperatures of heel and cargo layers, (b) LNG evaporation accumulation over time, (c) the LNG density at the heel-cargo interface, and (d) the rollover start time.**

#### 4.2.2 Effect of cargo to heel height ratio on the rollover start time

The cargo to heel height ratio (or cargo to heel thermal mass ratio) in cylindrical vertical storage tanks,  $\eta$ , is defined as,

$$\eta = \frac{H_{cargo}}{H_{heel}} \quad (4-1)$$

For the parametric study, the cargo to heel height ratios of 0.5, 1, 2, and 3 are considered. The height of the heel layer,  $H_{heel}$ , is maintained constant at 5.00 m in all cases. Figure 4.5 shows the effect of cargo to heel height ratio on the rollover start time.

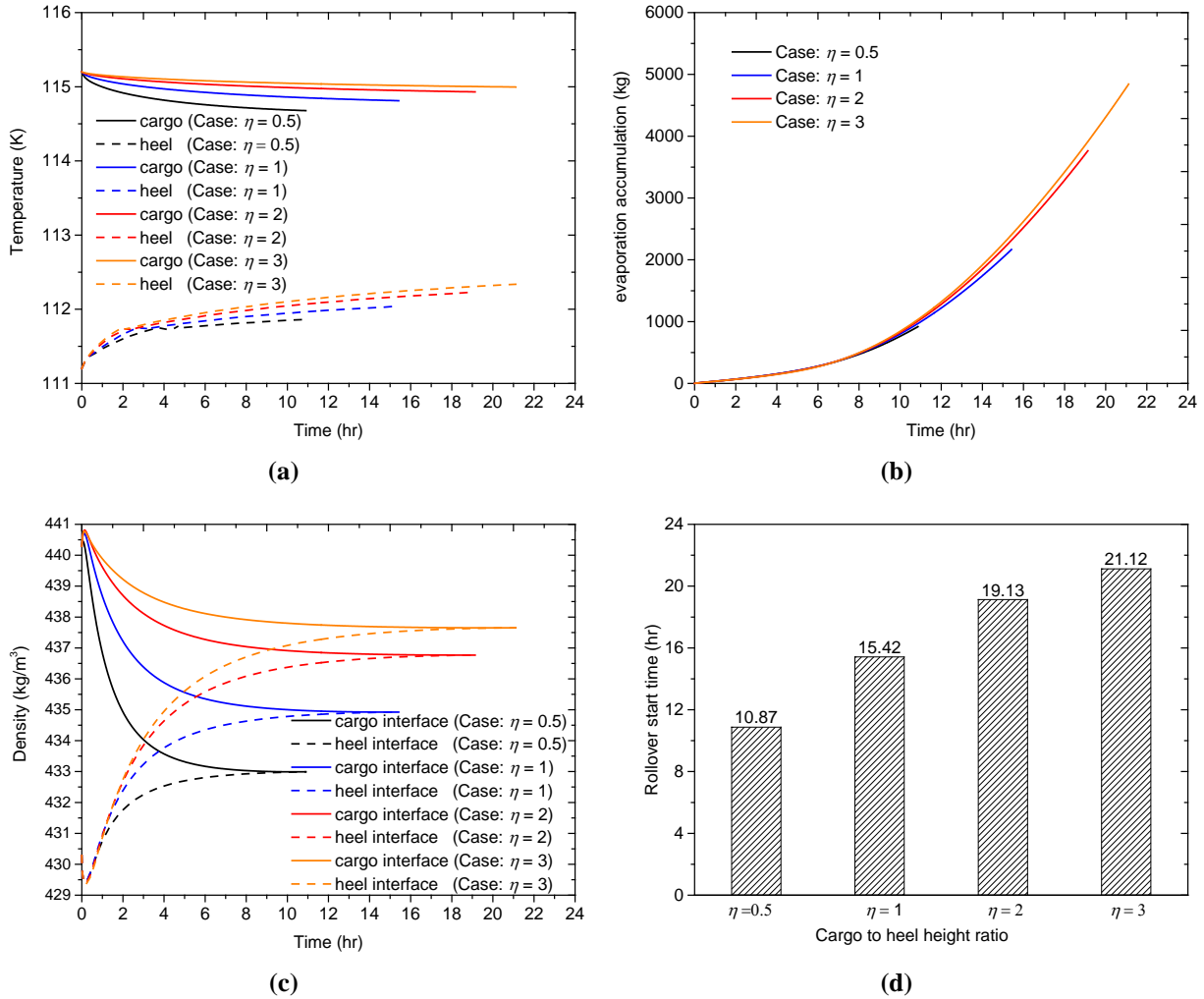


**Figure 4.5. Effect of cargo to heel height ratio on the rollover start time: (a) bulk temperatures of heel and cargo layers, (b) LNG evaporation accumulation over time, (c) the LNG density at the cargo-heel interface, and (d) the rollover start time.**

Figure 4.5(a) shows that decreasing the cargo to heel height ratio causes the bulk temperature of the cargo to vary more over time because its thermal mass decreases. However, the cargo to heel height ratio does not affect the BOG generation rate, and its trend remains unchanged (Figure

4.5(b)) because the evaporation occurs at the vapor-liquid interface and is not affected by the cargo to heel height ratio.

Figure 4.5(c) shows the LNG density profile at the heel-cargo interface. The numerical results indicate that the rollover start time is significantly affected by the cargo to heel height ratio. Increasing the cargo to heel height ratio from 0.5 to 3 increases the rollover start time from 10.87 hr to 21.12 hr (Figure 4.5(d)) which highlights the importance of the cargo thermal mass. The numerical results recommend that a higher cargo thermal mass postpones the rollover start time. Therefore, the amount of the cargo loaded to the tank should be determined taking into account the amount of heel in the tank.

### 4.2.3 Effect of tank aspect ratio on the rollover start time

The tank aspect ratio,  $AR$ , is defined as,

$$AR = \frac{H_{tank}}{D_{inner}} \quad (4-2)$$

For the parametric study, four aspect ratios are considered by varying the values of inner diameter,  $D_{inner}$  while the total height,  $H_{tank}$ , is maintained constant at 43.28 m (as given in Table 4.1). In this way, the volume of the tank also changes accordingly. Figure 4.6 shows the effect of the tank aspect ratio on the rollover start time. The numerical results show that in an atmospheric tank, the tank aspect ratio does not affect the bulk temperatures of the heel and cargo layers over time (Figure 4.6(a)). However, it affects the amount of LNG evaporation rate and BOG generation (Figure 4.6(b)). Increasing the tank aspect ratio increases the thermal mass of LNG in the tank and decreases the amount of BOG generation over time. Figure 4.6(c) shows that the LNG density

profiles at the heel-cargo interface are not affected by the tank aspect ratio over time. Consequently, the rollover start time changes by less than 13% with tank aspect ratios ranging from 0.62 to 1.76 (Figure 4.6(d)).

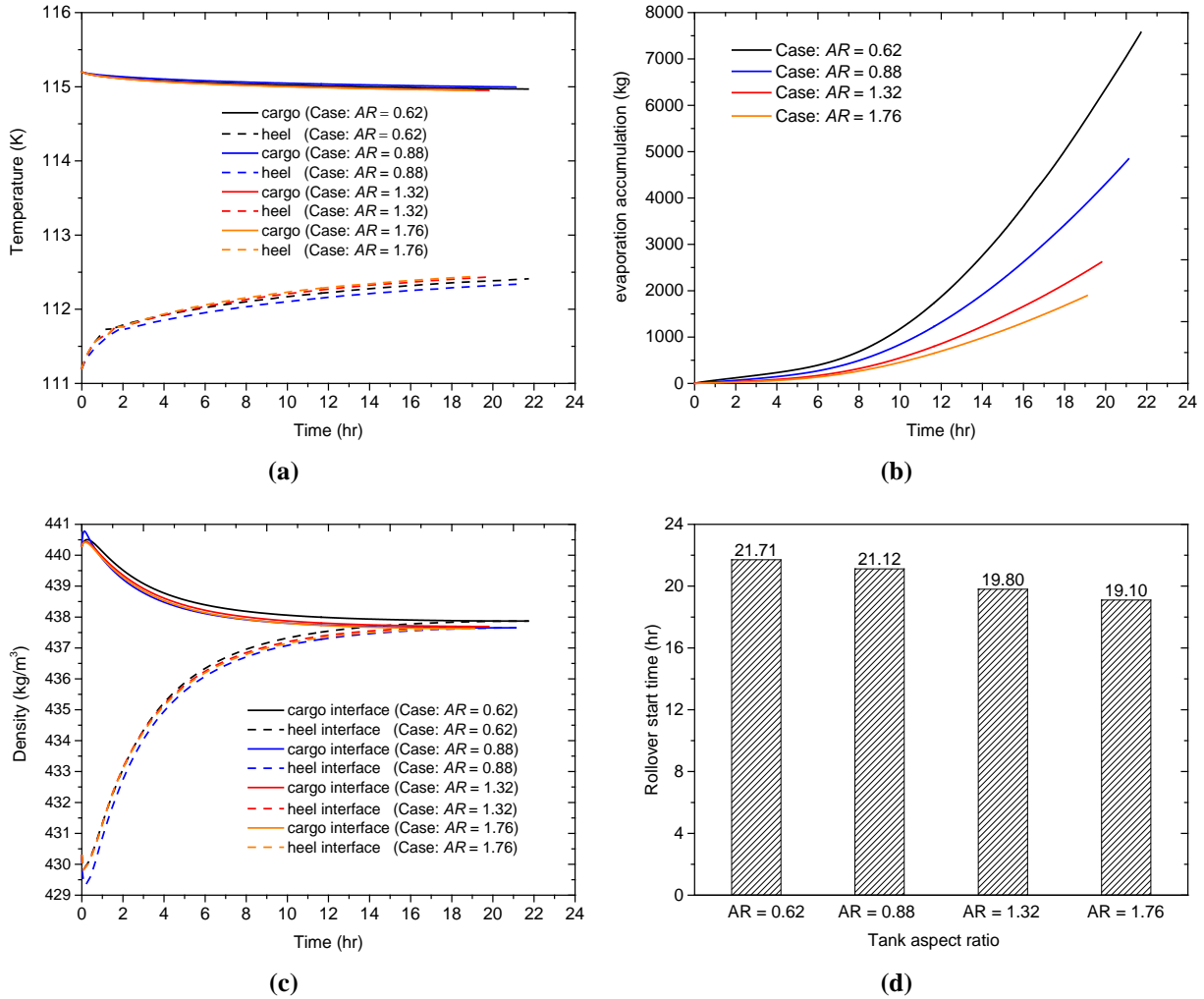


**Figure 4.6. Effect of tank aspect ratio on the rollover start time: (a) bulk temperatures of the heel and cargo layers, (b) LNG evaporation accumulation over time, (c) the LNG density at the cargo-heel interface, and (d) the rollover start time.**

### 4.3 Summary

This chapter demonstrated the application of the non-equilibrium multilayer thermodynamic model to study rollover phenomena in an LNG storage tank (e.g., the La Spezia rollover incidence).

Using this model, the thermal phenomena during the La Spezia rollover were analyzed, including the thermal stratification and density profile in the liquid domain. To find the possible methods to prevent the rollover, three parameters, namely, the heat transfer rate from the environment, cargo to heel height ratio, and tank aspect ratio, were studied. The parametric study indicated that the cargo to heel height ratio was a key factor in the rollover start time.

## **Chapter 5: Conclusions and Future Work**

### **5.1 Contributions of this Ph.D. work**

This Ph.D. study presents two numerical models, namely, the non-equilibrium thermodynamic model and the non-equilibrium multilayer thermodynamic model, to predict the thermal performance of LNG storage tanks including the temperature and pressure profiles, thermal stratification, and rollover with a short computation time.

### **5.2 Conclusions**

#### **5.2.1 Analysis of the non-equilibrium thermodynamic model**

To predict the bulk average temperature and pressure profiles in LNG storage tanks with short computation time, a non-equilibrium thermodynamic model based on the resistance-capacitance network was developed. The accuracy of the non-equilibrium thermodynamic model was verified against the experimental data, and models based on equilibrium thermodynamics and CFD. The model validation showed that both equilibrium and non-equilibrium thermodynamic models could predict the pressure and temperature of LNG storage tanks with good accuracy under stationary operating conditions. In addition, a minor difference between the thermal performance of vertical and horizontal storage tanks under stationary conditions was observed. However, the equilibrium thermodynamic model failed to predict the pressure and temperature of LNG storage tanks under dynamic operating conditions. In contrast, the non-equilibrium thermodynamic model could predict the performance of the LNG storage tanks under dynamic operating conditions, such as

vapor return from heavy-duty trucks to the station during a refuelling process. Further findings of this study were summarized as follows:

- 1) A higher thermal mass of LNG in the tank (i.e. a higher filling level) increased the LNG holding time of the storage tank in comparison with a tank with a lower amount of LNG (i.e. a lower filling level).
- 2) Horizontal LNG storage tanks could condense the extra vapor injected into their vapor space faster than vertical storage tanks because of having a larger vapor-liquid interface.
- 3) Refueling stations with horizontal LNG storage tanks could hold LNG for a longer time than those with vertical LNG storage tanks.
- 4) The non-equilibrium thermodynamic model is able to predict the thermal performance (pressure rise, and average bulk temperatures of vapor and liquid phases) of the LNG storage tanks under stationary and dynamic operating conditions with a low computation cost. In addition, the non-equilibrium thermodynamic model can be applied to BOG management in LNG tanks. Proper BOG management in LNG storage tanks allows them to receive vapor from more vehicles without releasing the BOG to the atmosphere. The non-equilibrium model will provide information on the proper tank size and positioning (vertical or horizontal) with respect to the demand, schedule of receiving a new load of LNG to condense the BOG in the storage tank, and maximizing the amount of vapor reception from vehicles while preventing the BOG being released to the atmosphere.

### **5.2.2 Analysis of the non-equilibrium multilayer thermodynamic model**

A non-equilibrium multilayer thermodynamic model was successfully employed to investigate the thermal stratification and rollover phenomena in cryogenic storage tanks with a short computation

time compared with CFD modelling. The accuracy of the model was checked against experimental data from LNG storage tanks. The validation demonstrated that the non-equilibrium multilayer thermodynamic model could accurately predict the temperature gradient, pressure, and density of LNG in the tank.

A parametric study was conducted to investigate the rollover phenomena, and it indicated that heat transfer rate to the tank and the tank aspect ratio were not the key factors in the rollover start time. However, they affected the amount of LNG evaporation and BOG generation rate (to be removed from the tank) to maintain the tank pressure close to atmospheric pressure. The numerical results highlighted that the amount of the cargo to heel ratio affected the rollover start time. A large cargo to heel height ratio ( $> 2$ ) could postpone the rollover time while the BOG generation rate remained constant. Therefore, the amount of the cargo loaded to the cryogenic tanks should be determined taking into account the amount of heel in the tank (to delay and minimize the probability of rollover.)

The parametric study of the non-equilibrium multilayer thermodynamic model demonstrates that this model can predict the LNG rollover occurrence, and prevent it in LNG industries

### **5.3 The limitations and future work**

The limitations of the research presented in this Ph.D. study are summarized as follows:

- 1) The heat transfer and boundary flow along the vertical tank walls are based on empirical correlations along an infinite vertical wall. This limitation has a minor impact on the results because the diameter of LNG storage tanks is large enough to neglect the effect of the

curvature of the tank walls. The boundary flow along the vertical tank walls in the vapor domain may be influenced by the corners at the top of the tank, and the boundary flow calculations based on an infinite vertical wall cannot be accurate. As the tank corners in the vapor domain cause the creation of secondary flow fields, the results of the non-equilibrium thermodynamic model can still give a good estimation of pressure and vapor average bulk temperature which are mainly affected by the boundary flow along the vertical tank walls. In addition, the boundary flow characters are complicated along non-cylindrical vertical tanks. Therefore, the non-equilibrium multilayer thermodynamic model does not apply to non-cylindrical tanks. However, the pressure and average bulk temperature can be predicted by the non-equilibrium thermodynamic model for the non-cylindrical tanks.

- 2) The mass transfer between the heel and cargo layers in the rollover case is a complex phenomenon. In this work, the Reynolds analogy method is applied to estimate the convective mass transfer rate at the heel-cargo interface. The convective mass transfer rate is calculated from the experimental correlations for different fluids than LNG such as a salt-water solution in the laboratory. Selecting appropriate correlations leads to various rollover start times. Heestand et al. [27] and Arjomandnia [61] compared the results using various correlations, and the ranges of the numerical results were from 20 to 60 hours. Therefore, the convective mass transfer correlation at the LNG heel-cargo interface requires further investigations.

The future research directions based on the current work may be reflected in the following aspects,

- 1) The convective mass transfer between heel and cargo layers is recommended to be fine-tuned based on the experimental data of mixing two LNG layers. In addition, the geometry of the LNG storage tanks, and operation of the LNG facilities (e.g., cargo to heel height ratio) may affect the rollover start time. To obtain a more accurate prediction on the rollover start time by using the non-equilibrium multilayer thermodynamic model, it is recommended to tune up the model by using the experimental data collected from the facility of interest.
- 2) The non-equilibrium thermodynamic model and non-equilibrium multilayer model developed in this Ph.D. study are independent from the cryogenic fluid thermophysical properties. Therefore, the applications of these models are not limited to LNG and can be extended to other cryogenic applications.
- 3) An experimental platform setup is recommended to study the thermal stratification in cryogenic tanks and validate the numerical models. The necessary requirements of the experimental platform include the following,
  - a. The cryogenic liquid tank should meet the national pressure tank codes and carry Canadian Registered Number (CRN). To obtain the thermal behavior inside the tank, the sensors (including a pressure sensor, mass flow meters, thermocouples, liquid level sensors, density sensors, etc.) are needed to be installed in the tank system. The installment of the sensors will unavoidably change the tank structure. For safety reasons, the tank with the changed structure should be re-evaluated to meet the national pressure tank codes and receive CRN stamp.
  - b. Enough space is needed for safety reasons. As methane is a combustible gas, the ventilation system, and emergency plan (isolated area) are also required.

## Bibliography

- [1] I.P.O.C.C. (2007). IPCC, Climate change 2007: synthesis report. UNEP e WMO, Intergovernmental Panel on Climate Change, 2007.  
[http://www.ipcc.ch/publications\\_and\\_data/ar4/syr/en/main.html](http://www.ipcc.ch/publications_and_data/ar4/syr/en/main.html) (accessed August 29, 2017).
- [2] IEA, IEA (2019), Global Energy & CO2 Status Report 2019, Paris, 2019.  
<https://www.iea.org/reports/global-energy-co2-status-report-2019>.
- [3] Global energy and CO2 emissions in 2020 – Global Energy Review 2020 – Analysis - IEA, (n.d.). <https://www.iea.org/reports/global-energy-review-2020/global-energy-and-co2-emissions-in-2020> (accessed June 16, 2021).
- [4] IPCC, A. Chidthaisong, P. Ciais, P. Cox, R. Dickinson, D. Hauglustaine, H. C, E. Holland, D. Jacob, U. Lohmann, S. Ramachandran, P. Leite da Silva, S.C. Wofsy, X. Zhang, Climate Change 2007: Working Group I: The Physical Science Basis, 2007.  
[https://www.ipcc.ch/publications\\_and\\_data/ar4/wg1/en/ch11.html](https://www.ipcc.ch/publications_and_data/ar4/wg1/en/ch11.html) (accessed August 29, 2017).
- [5] M. Levi, Climate consequences of natural gas as a bridge fuel, *Clim. Change*. 118 (2013) 609–623. <https://doi.org/10.1007/s10584-012-0658-3>.
- [6] X. Zhang, N.P. Myhrvold, Z. Hausfather, K. Caldeira, Climate benefits of natural gas as a bridge fuel and potential delay of near-zero energy systems, *Appl. Energy*. 167 (2016) 317–322. <https://doi.org/10.1016/j.apenergy.2015.10.016>.
- [7] Frequently Asked Questions (FAQs) How much carbon dioxide is produced when

- different fuels are burned? - U.S. Energy Information Administration (EIA), (n.d.).  
<https://www.eia.gov/tools/faqs/faq.php?id=73&t=11> (accessed June 16, 2021).
- [8] IEA (2019), *The Role of Gas in Today's Energy Transitions*, Paris, n.d.  
<https://www.iea.org/reports/the-role-of-gas-in-todays-energy-transitions>.
- [9] CER – Canada's Energy Future 2019 - Results, (n.d.). <https://www.cer-rec.gc.ca/en/data-analysis/canada-energy-future/2019/results/index.html> (accessed February 25, 2021).
- [10] R.D. Shell, *Shell LNG Outlook 2020*, 2020. <https://www.shell.com/energy-and-innovation/natural-gas/liquefied-natural-gas-lng/lng-outlook-2020.html#iframe=L3dIYmFwcHMvTE5HX291dGxvb2sv>.
- [11] Environment Canada, *National Inventory Report: Greenhouse Gas Sources and Sinks in Canada - Executive Summary*, (n.d.).  
<http://www.publications.gc.ca/site/eng/9.506002/publication.html> (accessed March 9, 2021).
- [12] IEA (2020), *Gas 2020*, (2020). <https://www.iea.org/reports/gas-2020> (accessed January 28, 2021).
- [13] S. Mokhatab, *LNG Fundamentals*, in: D.A. Mak, John Y.; Valappil, Jaleel V.; Wood (Ed.), *Handb. Liq. Nat. Gas*, Elsevier, 2014: pp. 1–106. <https://doi.org/10.1016/B978-0-12-404585-9.00001-5>.
- [14] Đ. Dobrota, B. Lalić, I. Komar, *Problem of boil-off in LNG supply chain*, *Trans. Marit. Sci.* 2 (2013) 91–100. <https://doi.org/10.7225/toms.v02.n02.001>.
- [15] X. Cheng, A. Rahman, *BOG ventilation and combustion in re-liquefaction plants of LNG carriers*, in: *2014 Ocean. - St. John's, Ocean. 2014, IEEE*, 2015: pp. 1–7.  
<https://doi.org/10.1109/OCEANS.2014.7003288>.

- [16] S.A. Faka, Boil off gas management during ship-to-ship transfer of LNG, US 20090199575A1, 2013. [https://doi.org/10.1016/j.\(73\)](https://doi.org/10.1016/j.(73)).
- [17] A.K. Majumdar, T.E. Steadman, J.L. Maroney, Numerical Modeling of Propellant Boiloff in Cryogenic Storage Tank, NASA Tech. Rep. (Report No. NASA/TM-2007-215131, M-1206). (2007) 90. <https://ntrs.nasa.gov/search.jsp?R=20080013162>.
- [18] H.N. Rao, K.H. Wong, I.A. Karimi, Minimizing power consumption related to BOG reliquefaction in an LNG regasification terminal, *Ind. Eng. Chem. Res.* 55 (2016) 7431–7445. <https://doi.org/10.1021/acs.iecr.6b01341>.
- [19] Understanding Natural Gas and LNG Options, US Department of Energy, 2017. <https://energy.gov/ia/downloads/supporting-development-natural-gas-markets-and->.
- [20] C. Migliore, C. Tubilleja, V. Vesovic, Weathering prediction model for stored liquefied natural gas (LNG), *J. Nat. Gas Sci. Eng.* 26 (2015) 570–580. <https://doi.org/10.1016/j.jngse.2015.06.056>.
- [21] H. Thomson, J.J. Corbett, J.J. Winebrake, Natural gas as a marine fuel, *Energy Policy.* 87 (2015) 153–167. <https://doi.org/10.1016/j.enpol.2015.08.027>.
- [22] R. Wurster, W. Zittel, C. Heidt, BMVI, LNG as an alternative fuel for the operation of ships and heavy-duty vehicles, (2014).
- [23] B.H. Min, J.T. Chung, H.Y. Kim, S. Park, Effects of gas composition on the performance and emissions of compressed natural gas engines, *KSME Int. J.* 16 (2002) 219–226. <https://doi.org/10.1007/BF03185173>.
- [24] A. Kowalewicz, M. Wojtyniak, H. Ly, Effects of natural gas composition variations on the operation, performance and exhaust emissions of natural gas-powered vehicles, *NGV 2002 Conf. Pap. Eff. Gas Compos.* 219 (2002) 1–22.

- <https://doi.org/10.1243/095440705X6399>.
- [25] E.R.F. Winter, R.J. Schoenhals, Improved fluid dynamics similarity, analysis and verification. Part 5: Analytical and experimental studies of thermal stratification phenomena, 1968.
- [26] J.A.Sarsten, LNG Stratification and Rollover, Pipeline Gas J. 199 (1972) 37–39.
- [27] J. Heestand, C.W.Shipman, J.W.Meador, C.W. Shipman, J.W. Meador, A predictive model for rollover in stratified LNG tanks, AIChE J. 29 (1983) 199–207.  
<https://doi.org/10.1002/aic.690290205>.
- [28] N. Chatterjee, J.M. Geist, Effects of stratification on boil-off rates in LNG tanks, Pipeline Gas J. 199 (1972).
- [29] J.Q. Shi, C. Beduz, R.G. Scurlock, Numerical modelling and flow visualization of mixing of stratified layers and rollover in LNG, Inst. Cryog. Southampt. 33 (1993) 1116–1124.
- [30] M.S. Khelifi-Touhami, A. Benbrik, D. Lemonnier, D. Blay, Laminar natural convection flow in a cylindrical cavity application to the storage of LNG, J. Pet. Sci. Eng. 71 (2010) 126–132. <https://doi.org/10.1016/j.petrol.2009.12.011>.
- [31] S. Roh, G. Son, Numerical study of natural convection in a liquefied natural gas tank, J. Mech. Sci. Technol. 26 (2012) 3133–3140. <https://doi.org/10.1007/s12206-012-0820-x>.
- [32] S. Roh, G. Son, G. Song, J. Bae, Numerical study of transient natural convection in a pressurized LNG storage tank, Appl. Therm. Eng. 52 (2013) 209–220.  
<https://doi.org/10.1016/j.applthermaleng.2012.11.021>.
- [33] M. Miana, R. Legorburo, D. Díez, Y.H. Hwang, Calculation of boil-off rate of liquefied natural gas in Mark III tanks of ship carriers by numerical analysis, Appl. Therm. Eng. 93 (2016) 279–296. <https://doi.org/10.1016/j.applthermaleng.2015.09.112>.

- [34] S.W. Choi, W. Il Lee, H.S. Kim, Numerical analysis of convective flow and thermal stratification in a cryogenic storage tank, *Numer. Heat Transf. Part A Appl.* 71 (2017) 402–422. <https://doi.org/10.1080/10407782.2016.1264771>.
- [35] A. Saleem, S. Farooq, I.A. Karimi, R. Banerjee, A CFD simulation study of boiling mechanism and BOG generation in a full-scale LNG storage tank, *Comput. Chem. Eng.* 115 (2018) 112–120. <https://doi.org/10.1016/j.compchemeng.2018.04.003>.
- [36] F. Ovidi, E. Pagni, G. Landucci, L. Tognotti, C. Galletti, CFD modelling of vertical LNG tanks adopted in heavy trucks refuelling stations, *Chem. Eng. Trans.* 67 (2018) 547–552. <https://doi.org/10.3303/CET1867092>.
- [37] A. Sharafian, O.E. Herrera, W. Mérida, Performance analysis of liquefied natural gas storage tanks in refueling stations, *J. Nat. Gas Sci. Eng.* 36 (2016) 496–509. <https://doi.org/10.1016/j.jngse.2016.10.062>.
- [38] M. Miana, R. Del Hoyo, V. Rodrigálvarez, Comparison of evaporation rate and heat flow models for prediction of Liquefied Natural Gas (LNG) ageing during ship transportation, *Fuel*. 177 (2016) 87–106. <https://doi.org/10.1016/j.fuel.2016.02.070>.
- [39] M.S. Khan, S. Effendy, I.A. Karimi, A. Wazwaz, Improving design and operation at LNG regasification terminals through a corrected storage tank model, *Appl. Therm. Eng.* 149 (2019) 344–353. <https://doi.org/10.1016/j.applthermaleng.2018.12.060>.
- [40] S. Effendy, M.S. Khan, S. Farooq, I.A. Karimi, Dynamic modelling and optimization of an LNG storage tank in a regasification terminal with semi-analytical solutions for N<sub>2</sub>-free LNG, *Comput. Chem. Eng.* 99 (2017) 40–50. <https://doi.org/10.1016/j.compchemeng.2017.01.012>.
- [41] C. Migliore, A. Salehi, V. Vesovic, A non-equilibrium approach to modelling the

- weathering of stored Liquefied Natural Gas (LNG), *Energy*. 124 (2017) 684–692.  
<https://doi.org/10.1016/j.energy.2017.02.068>.
- [42] R.N. Krikkis, A thermodynamic and heat transfer model for LNG ageing during ship transportation. Towards an efficient boil-off gas management, *Cryogenics (Guildf)*. 92 (2018) 76–83. <https://doi.org/10.1016/j.cryogenics.2018.04.007>.
- [43] Y. Qu, I. Noba, X. Xu, R. Privat, J.N. Jaubert, A thermal and thermodynamic code for the computation of Boil-Off Gas – Industrial applications of LNG carrier, *Cryogenics (Guildf)*. 99 (2019) 105–113. <https://doi.org/10.1016/j.cryogenics.2018.09.002>.
- [44] T.E.Bailey, R.F.Fearn, Analytical and experimental determination of liquid-hydrogen, *Adv. Cryog. Eng.* (1964) 254–264.
- [45] J.H. Chin, E. Harper, F. Hines, S. Hurd, G.C.Vliet, Analytical and experimental study of stratification and liquid-ullage coupling, 1965.
- [46] S.E.Hurd, M.P.Hollister, J.H.Chin, H.M.Satterlee, E.Y.Harper, Analytical and experimental study liquid-ullage coupling and gravity interface, NASA Contractor Rep. NAS 8-11525. (1966).
- [47] R.W. Arnett, R.O. Voth, A computer program for the calculation of thermal stratification and self-pressurization in a liquid hydrogen tank, 1972.
- [48] E.R.F. Winter, R.J. Schoenhals, Analytical and experimental studies of thermal stratification phenomena, (1968).
- [49] S. Gursu, S.A. Sherif, T.N. Veziroglu, J.W. Sheffield, Analysis and Optimization of Thermal Stratification and Self-Pressurization Effects in Liquid Hydrogen Storage Systems—Part 1: Model Development, *J. Energy Resour. Technol.* 115 (1993) 221.  
<https://doi.org/10.1115/1.2905998>.

- [50] S. Gursu, S.A. Sherif, T.N. Veziroglu, J.W. Sheffield, Analysis and Optimization of Thermal Stratification and Self-Pressurization Effects in Liquid Hydrogen Storage Systems—Part 2: Model Results and Conclusions, *J. Energy Resour. Technol.* 115 (1993) 228. <https://doi.org/10.1115/1.2905998>.
- [51] M. Seo, S. Jeong, Analysis of self-pressurization phenomenon of cryogenic fluid storage tank with thermal diffusion model, *Cryogenics (Guildf)*. 50 (2010) 549–555. <https://doi.org/10.1016/j.cryogenics.2010.02.021>.
- [52] M.J. Daigle, V.N. Smelyanskiy, J. Boschee, M. Foygel, Temperature stratification in a cryogenic fuel tank, *J. Thermophys. Heat Transf.* 27 (2013) 116–126. <https://doi.org/10.2514/1.T3933>.
- [53] J. Joseph, G. Agrawal, D.K. Agarwal, J.C. Pisharady, S. Sunil Kumar, Effect of insulation thickness on pressure evolution and thermal stratification in a cryogenic tank, *Appl. Therm. Eng.* (2016). <https://doi.org/10.1016/j.applthermaleng.2016.07.015>.
- [54] M. Kang, J. Kim, H. You, D. Chang, Experimental investigation of thermal stratification in cryogenic tanks, *Exp. Therm. Fluid Sci.* 96 (2018) 371–382. <https://doi.org/10.1016/j.expthermflusci.2017.12.017>.
- [55] Z. Duan, H. Sun, C. Cheng, W. Tang, H. Xue, A moving-boundary based dynamic model for predicting the transient free convection and thermal stratification in liquefied gas storage tank, *Int. J. Therm. Sci.* 160 (2021). <https://doi.org/10.1016/j.ijthermalsci.2020.106690>.
- [56] SIGTTO, Guidance for the Prevention of Rollover in LNG Ships Contents, Bermuda, 2012. [https://www.sigtto.org/media/1398/guidance-for-the-prevention-of-rollover-on-lng\\_ships.pdf](https://www.sigtto.org/media/1398/guidance-for-the-prevention-of-rollover-on-lng_ships.pdf) (accessed May 25, 2021).

- [57] A.E. Germeles, A Model for LNG Tank Rollover, in: *Adv. Cryog. Eng.*, 1975: pp. 326–336. [https://doi.org/10.1007/978-1-4757-0208-8\\_42](https://doi.org/10.1007/978-1-4757-0208-8_42).
- [58] S. Bates, D.S. Morrison, Modelling the behaviour of stratified liquid natural gas in storage tanks: a study of the rollover phenomenon, *Int. J. Heat Mass Transf.* 40 (1997) 1875–1884. [https://doi.org/10.1016/S0017-9310\(96\)00218-9](https://doi.org/10.1016/S0017-9310(96)00218-9).
- [59] W.B. Zimmerman, J.M. Rees, Rollover instability due to double diffusion in a stably stratified cylindrical tank, *Phys. Fluids.* 19 (2007). <https://doi.org/10.1063/1.2827488>.
- [60] Y. Li, Z. Li, W. Wang, Simulating on rollover phenomenon in LNG storage tanks and determination of the rollover threshold, *J. Loss Prev. Process Ind.* 37 (2015) 132–142. <https://doi.org/10.1016/j.jlp.2015.07.007>.
- [61] P. Arjomandnia, Simulation of LNG rollover in storage tanks, Curtin University, 2015.
- [62] A. Hubert, S. Dembele, P. Denissenko, J. Wen, Predicting Liquefied Natural Gas (LNG) rollovers using Computational Fluid Dynamics, *J. Loss Prev. Process Ind.* 62 (2019) 103922. <https://doi.org/10.1016/j.jlp.2019.103922>.
- [63] C. Beduz, R.G. Scurlock, Evaporation mechanisms and instabilities in cryogenic liquids, *Adv. Cryog. Eng.* 39 (1994) 1749–1757. [https://doi.org/10.1007/978-1-4615-2522-6\\_214](https://doi.org/10.1007/978-1-4615-2522-6_214).
- [64] W.H. Lee, A pressure iteration scheme for two-phase flow modeling, in: *Multiph. Transp. Fundam. React. Safety, Appl. Proc. Multi-Phase Flow Heat Transf. Symp.*, New Mexico, USA, 1979: pp. 407–431.
- [65] ANSYS Inc., ANSYS FLUENT Theory Guide, 2011.
- [66] M. Bond, H. Struchtrup, Mean evaporation and condensation coefficients based on energy dependent condensation probability, *Phys. Rev. E - Stat. Physics, Plasmas, Fluids, Relat. Interdiscip. Top.* 70 (2004) 21. <https://doi.org/10.1103/PhysRevE.70.061605>.

- [67] M. Kassemi, O. Kartuzova, Effect of interfacial turbulence and accommodation coefficient on CFD predictions of pressurization and pressure control in cryogenic storage tank, *Cryogenics (Guildf)*. 74 (2016) 138–153.  
<https://doi.org/10.1016/j.cryogenics.2015.10.018>.
- [68] Z. Yang, X.F. Peng, P. Ye, Numerical and experimental investigation of two phase flow during boiling in a coiled tube, *Int. J. Heat Mass Transf.* 51 (2008) 1003–1016.  
<https://doi.org/10.1016/j.ijheatmasstransfer.2007.05.025>.
- [69] M. Gong, J. Ma, J. Wu, Y. Zhang, Z. Sun, Y. Zhou, Nucleate pool boiling of liquid methane and its natural gas mixtures, *Int. J. Heat Mass Transf.* 52 (2009) 2733–2739.  
<https://doi.org/10.1016/j.ijheatmasstransfer.2008.12.011>.
- [70] R.G. Scurlock, Surface Evaporation of Cryogenic Liquids, Including LNG and LPG, in: *Stratif. Roll. Handl. LNG, LPG Other Cryog. Liq. Mix.*, Springer International Publishing, 2016: pp. 41–62. <https://link.springer.com/book/10.1007%2F978-3-319-20696-7>.
- [71] F.P. Incropera, D. David P, T.L. Bergman, A. S.Lavine, Kirchhoff's Law, in: *Fundam. Heat Mass Transf.*, 6th ed., Wiley, 2007: pp. 762–763.  
<https://doi.org/10.1073/pnas.0703993104>.
- [72] J.R. Lloyd, W.R. Moran, Natural convection adjacent to horizontal surface of various planforms, *J. Heat Transfer*. 96 (2010) 443. <https://doi.org/10.1115/1.3450224>.
- [73] E. Radziemska, W.M. Lewandowski, Heat transfer by natural convection from an isothermal downward-facing round plate in unlimited space, *Appl. Energy*. 68 (2001) 347–366. [https://doi.org/10.1016/S0306-2619\(00\)00061-1](https://doi.org/10.1016/S0306-2619(00)00061-1).
- [74] I. Ashour, N. Al-Rawahi, A. Fatemi, G. Vakili-Nezhaad, Applications of Equations of State in the Oil and Gas Industry, *Thermodyn. - Kinet. Dyn. Syst.* (2011) 165–178.

<https://doi.org/10.5772/23668>.

- [75] D.-Y. Peng, D.B. Robinson, A New Equation of State, *Ind. Eng. Chem.. Fundam.* 15 (1976) 59–64.  
<http://www.ncbi.nlm.nih.gov/pubmed/16587439><http://www.pubmedcentral.nih.gov/articlerender.fcgi?artid=PMC522396>.
- [76] J.R. Elliott, C.T. Lira, *Introductory Chemical Engineering Thermodynamics*, 2nd Edition, Pearson, 2012. <https://www.pearson.com/us/higher-education/product/Elliott-Introductory-Chemical-Engineering-Thermodynamics-2nd-Edition/9780132901093.html>.
- [77] A.M. Abudour, S.A. Mohammad, R.L. Robinson, K.A.M. Gasem, Volume-translated Peng–Robinson equation of state for saturated and single-phase liquid densities, *Fluid Phase Equilib.* 335 (2012) 74–87. <https://doi.org/10.1016/j.fluid.2012.08.013>.
- [78] P.M. Mathias, T. Naheiri, E.M. Oh, A density correction for the Peng-Robinson equation of state, *Fluid Phase Equilib.* 47 (1989) 77–87. [https://doi.org/10.1016/0378-3812\(89\)80051-2](https://doi.org/10.1016/0378-3812(89)80051-2).
- [79] D.M. Tellep, E.Y. Harper, Approximate analysis of propellant stratification, *AIAA J.* 1 (1963) 1954–1956. <https://doi.org/10.2514/3.1977>.
- [80] A.Pellew, R.V.Southwell, On maintained convective motion in a fluid heated from below, *Proc. R. Soc. London. Ser. A. Math. Phys. Sci.* 176 (1940) 312–343.  
<https://doi.org/10.1098/rspa.1940.0092>.
- [81] S. Globe, D. Dropkin, Natural-Convection Heat Transfer in Liquids Confined by Two Horizontal Plates and Heated From Below, *J. Heat Transfer.* 81 (1959) 24–28.  
<https://doi.org/10.1115/1.4008124>.
- [82] E.M.E. Sparrow, Laminar free convection on a vertical plate with prescribed nonuniform

wall heat flux or prescribed nonuniform wall temperature, National Advisory Committee for Aeronautics, 1955.

[https://books.google.ca/books?hl=en&lr=&id=bMtCAQAIAAJ&oi=fnd&pg=PA1&ots=9dx2mSNYPs&sig=ADgDI64q4svQxNomtB-ypZtB-q8&redir\\_esc=y#v=onepage&q&f=false](https://books.google.ca/books?hl=en&lr=&id=bMtCAQAIAAJ&oi=fnd&pg=PA1&ots=9dx2mSNYPs&sig=ADgDI64q4svQxNomtB-ypZtB-q8&redir_esc=y#v=onepage&q&f=false).

- [83] G.C. Vliet, D.C. Ross, Turbulent Natural Convection on Upward and Downward Facing Inclined Constant Heat Flux Surfaces., Am. Soc. Mech. Eng. (1974) 549–554.
- [84] E.R.G. Eckert, Introduction to Heat and Mass Transfer, McGraw-Hill, New York, 1963.
- [85] E.R.G. Eckert, T.W. Jackson, Analysis of turbulent free-convection boundary layer on flat plate, 1950.
- [86] A.S. Mujumdar, Handbook Of Single-Phase Convective Heat Transfer, Dry. Technol. (1989). <https://doi.org/10.1080/07373938908916581>.
- [87] P. Schallhorn, D.M. Campbell, S. Chase, J. Piquero, C. Fortenberry, X. Li, L. Grob, Upper stage tank thermodynamic modeling using SINDA/FLUINT, Collect. Tech. Pap. - AIAA/ASME/SAE/ASEE 42nd Jt. Propuls. Conf. 9 (2006) 7062–7076. <https://doi.org/10.2514/6.2006-5051>.
- [88] M. Thirumaleshwar, Fundamentals of heat and mass transfer, Pearson, 2006. <https://learning.oreilly.com/library/view/fundamentals-of-heat/9789332503397/>.
- [89] G. Greg Harper, C. Charles Powars, Advanced liquid natural gas onboard storage system, Golden, CO, 2003. <https://doi.org/10.2172/835120>.
- [90] C. Ludwig, M.E. Dreyer, E.J. Hopfinger, Pressure variations in a cryogenic liquid storage tank subjected to periodic excitations, Int. J. Heat Mass Transf. 66 (2013) 223–234. <https://doi.org/10.1016/j.ijheatmasstransfer.2013.06.072>.

- [91] S.W. Van Sciver, Low-Temperature Materials Properties, in: Helium Cryog., Springer US, Boston, MA, 1986: pp. 17–51. [https://doi.org/10.1007/978-1-4899-0499-7\\_2](https://doi.org/10.1007/978-1-4899-0499-7_2).
- [92] ANSYS® Academic Research fluent, Release 18, (n.d.).
- [93] R.G. Scurlock, Vacuum insulated tanks for pressurised LNG, in: Stratif. Roll. Handl. LNG, LPG Other Cryog. Liq. Mix., Springer International Publishing, Cham, 2016: pp. 63–83. [https://doi.org/10.1007/978-3-319-20696-7\\_5](https://doi.org/10.1007/978-3-319-20696-7_5).
- [94] LNG storage vessels, Chart Ind. Inc. (2016). [www.ChartLNG.com](http://www.ChartLNG.com) (accessed January 25, 2019).
- [95] S.D. Augustynowicz, Cryogenic Thermal Insulation Systems, 16th Thermal and Fluids Analysis Workshop, 2005.
- [96] C.A. Powars, Brookhaven National Laboratory, Powars, C. A. “Best Practices to Avoid LNG Fueling Station Venting Losses.,” San Jose, CA (2010)., 2010.
- [97] N. Baker, M. Creed, Stratification and Rollover in Liquefied Natural Gas Storage Tanks, Inst. Chem. Eng. Symp. Ser. (1995) 621–634.
- [98] S.W. Churchill, H.H.S. Chu, Correlating equations for laminar and turbulent free convection from a vertical plate, Int. J. Heat Mass Transf. 18 (1975) 1323–1329. [https://doi.org/10.1016/0017-9310\(75\)90243-4](https://doi.org/10.1016/0017-9310(75)90243-4).
- [99] S.W. Churchill, H.H.S. Chu, Correlating equations for laminar and turbulent free convection from a horizontal cylinder, Int. J. Heat Mass Transf. 18 (1975) 1049–1053. [https://doi.org/10.1016/0017-9310\(75\)90222-7](https://doi.org/10.1016/0017-9310(75)90222-7).
- [100] N.E. Evans, L.B.; Stefany, An experimental study of transient heat transfer to liquids in an cylindrical enclosures., Chem. Eng. Progr., Symp. 62 (1966) 209–215.
- [101] E.W. Lemmon, M.O. McLinden, D.G. Friend, “Thermophysical Properties of Fluid

Systems” in NIST Chemistry webbook; NIST standard reference database No. 69, 2017.

<https://doi.org/10.18434/T4D303>.

[102] L. Grunberg, A.H. Nissan, Mixture Law for Viscosity, *Nature*. 164 (1949) 799.

<https://doi.org/10.1038/164799a0>.

[103] C.C. Li, Thermal conductivity of liquid mixtures, *AIChE J.* 22 (1976) 927–930.

[104] F. Hering, L. Zipperer, Calculation of the Viscosity of Technical Gas Mixtures from Viscosity of the individual Gases, *Das Gas- Und Wasserfach*. (1936) 49–54 and 67–73.

## Appendices

### Appendix A

#### A.1 Thermal resistance-capacitance network

The details of the thermal resistance-capacitance network shown in Figure 2.3 are summarized in Table A1.

**Table A1. Details of the thermal resistance-capacitance network shown in Figure 2.3.**

<b>Description</b>	<b>Definition</b>	<b>Eq.</b>
<i>Vertical tank</i> : outer convection resistance on the top wall	$R_1 = \frac{1}{h_{outer-top\ wall,v} A_{outer-top\ wall,v}}$	(A-1)
<i>Horizontal tank</i> : outer convection resistance on the end walls in contact with the vapor space	$R_1 = \frac{1}{h_{outer-end\ walls,v} A_{outer-end\ walls,v}}$	
<i>Vertical tank</i> : conduction resistance on the top wall due to insulation	$R_2 = \frac{t_{insulation}}{k_{insulation} A_{inner-top\ wall,v}}$	(A-2)
<i>Horizontal tank</i> : conduction resistance on the end walls in contact with the vapor space due to insulation	$R_2 = \frac{t_{insulation}}{k_{insulation} A_{inner-end\ walls,v}}$	
<i>Vertical tank</i> : inner convection resistance on the top wall	$R_3 = \frac{1}{h_{inner-top\ wall,v} A_{inner-top\ wall,v}}$	(A-3)
<i>Horizontal tank</i> : inner convection resistance on the end walls in contact with the vapor space	$R_3 = \frac{1}{h_{inner-end\ walls,v} A_{inner-end\ walls,v}}$	
<i>Vertical tank</i> : outer convection resistance on the vertical wall in contact with vapor space	$R_4 = \frac{1}{h_{outer-vertical\ wall,v} A_{outer-vertical\ wall,v}}$	(A-4)
<i>Horizontal tank</i> : outer convection resistance on the top wall in contact with the vapor space	$R_4 = \frac{1}{h_{outer-top\ wall,v} A_{outer-top\ wall,v}}$	

Description	Definition	Eq.
<i>Vertical tank</i> : conduction resistance on the vertical wall in contact with the vapor space due to insulation	$R_5 = \frac{\ln(D_{i,outer\ wall} / D_{o,inner\ wall})}{2k_{insulation}A_{outer-vertical\ wall,v} / D_{i,outer\ wall}}$	(A-5)
<i>Horizontal tank</i> : conduction resistance on the top wall in contact with the vapor space due to insulation	$R_5 = \frac{\ln(D_{i,outer\ wall} / D_{o,inner\ wall})}{2k_{insulation}A_{outer-top\ wall,v} / D_{i,outer\ wall}}$	
<i>Vertical tank</i> : inner convection resistance on the vertical wall in contact with the vapor space	$R_6 = \frac{1}{h_{inner-vertical\ wall,v}A_{inner-vertical\ wall,v}}$	(A-6)
<i>Horizontal tank</i> : inner convection resistance on the top wall in contact with the vapor space	$R_6 = \frac{1}{h_{inner-top\ wall,v}A_{inner-top\ wall,v}}$	
<i>Vertical tank</i> : outer convection resistance on the vertical wall in contact with the liquid space	$R_7 = \frac{1}{h_{outer-vertical\ wall,l}A_{outer-vertical\ wall,l}}$	(A-7)
<i>Horizontal tank</i> : outer convection resistance on the bottom wall in contact with the liquid space	$R_7 = \frac{1}{h_{outer-bottom\ wall,l}A_{outer-bottom\ wall,l}}$	
<i>Vertical tank</i> : conduction resistance on the vertical wall in contact with the liquid space due to insulation	$R_8 = \frac{\ln(D_{i,outer\ wall} / D_{o,inner\ wall})}{2k_{insulation}A_{outer-vertical\ wall,l} / D_{i,outer\ wall}}$	(A-8)
<i>Horizontal tank</i> : conduction resistance on the bottom wall in contact with the liquid space due to insulation	$R_8 = \frac{\ln(D_{i,outer\ wall} / D_{o,inner\ wall})}{2k_{insulation}A_{outer-bottom\ wall,l} / D_{i,outer\ wall}}$	
<i>Vertical tank</i> : inner convection resistance on the vertical wall in contact with the liquid space	$R_9 = \frac{1}{h_{inner-vertical\ wall,l}A_{inner-vertical\ wall,l}}$	(A-9)
<i>Horizontal tank</i> : inner convection resistance on the bottom wall in contact with the liquid space	$R_9 = \frac{1}{h_{inner-bottom\ wall,l}A_{inner-bottom\ wall,l}}$	
<i>Vertical tank</i> : outer convection resistance on the bottom wall	$R_{10} = \frac{1}{h_{outer-bottom\ wall,l}A_{outer-bottom\ wall,l}}$	(A-10)
<i>Horizontal tank</i> : outer convection resistance on the end walls in contact with the liquid space	$R_{10} = \frac{1}{h_{outer-end\ walls,l}A_{outer-end\ walls,l}}$	
<i>Vertical tank</i> : conduction resistance on the bottom wall due to insulation	$R_{11} = \frac{t_{insulation}}{k_{insulation}A_{inner-bottom\ wall,l}}$	(A-11)
<i>Horizontal tank</i> : conduction resistance on the end walls in contact with the liquid space due to insulation	$R_{11} = \frac{t_{insulation}}{k_{insulation}A_{inner-end\ walls,l}}$	

<b>Description</b>	<b>Definition</b>	<b>Eq.</b>
<i>Vertical tank</i> : inner convection resistance on the bottom wall	$R_{12} = \frac{1}{h_{inner-bottom\ wall,l} A_{inner-bottom\ wall,l}}$	(A-12)
<i>Horizontal tank</i> : inner convection resistance on the end walls in contact with the liquid space	$R_{12} = \frac{1}{h_{inner-end\ walls,l} A_{inner-end\ walls,l}}$	
<i>Vertical tank</i> : conduction resistance between the outer top wall and outer vertical wall in contact with the vapor space	$R_{13} = \frac{L_{o,top-vertical,v}}{k_{outer\ wall} A_{cross\ section,o,top-vertical,v}}$	(A-13)
<i>Horizontal tank</i> : conduction resistance between outer top wall and outer end walls in contact with the vapor space	$R_{13} = \frac{L_{o,top-end\ walls,v}}{k_{outer\ wall} A_{cross\ section,o,top-end\ walls,v}}$	
<i>Vertical tank</i> : conduction resistance between inner top wall and inner vertical wall in contact with the vapor space	$R_{14} = \frac{L_{i,top-vertical,v}}{k_{inner\ wall} A_{cross\ section,i,top-vertical,v}}$	(A-14)
<i>Horizontal tank</i> : conduction resistance between inner top wall and inner end walls in contact with the vapor space	$R_{14} = \frac{L_{i,top-end\ walls,v}}{k_{outer\ wall} A_{cross\ section,i,top-end\ walls,v}}$	
<i>Vertical tank</i> : conduction resistance in the outer vertical wall in contact with the liquid and vapor spaces	$R_{15} = \frac{L_{vertical\ wall,v-vertical\ wall,l}}{k_{outer\ wall} A_{cross\ section,o,vertical\ wall}}$	(A-15)
<i>Horizontal tank</i> : conduction resistance between outer top wall in contact with the vapor space and the outer bottom wall in contact with the liquid space	$R_{15} = \frac{L_{top\ wall,v-bottom\ wall,l}}{k_{outer\ wall} A_{cross\ section,outer\ wall}}$	
<i>Vertical tank</i> : conduction resistance in the inner vertical wall in contact with liquid and vapor spaces	$R_{16} = \frac{L_{vertical\ wall,v-vertical\ wall,l}}{k_{inner\ wall} A_{cross\ section,i,vertical\ wall}}$	(A-16)
<i>Horizontal tank</i> : conduction resistance between inner top wall in contact with the vapor space and the inner bottom wall in contact with the liquid space	$R_{16} = \frac{L_{top\ wall,v-bottom\ wall,l}}{k_{inner\ wall} A_{cross\ section,inner\ wall}}$	
<i>Vertical tank</i> : conduction resistance between outer bottom wall and outer vertical wall in contact with the liquid space	$R_{17} = \frac{L_{o,bottom-vertical,l}}{k_{outer\ wall} A_{cross\ section,o,bottom-vertical,l}}$	(A-17)

<b>Description</b>	<b>Definition</b>	<b>Eq.</b>
<i>Horizontal tank</i> : conduction resistance between outer bottom wall and outer end walls in contact with the liquid space	$R_{17} = \frac{L_{o,bottom-end\ walls,l}}{k_{outer\ wall} A_{cross\ section,o,bottom-end\ walls,l}}$	
<i>Vertical tank</i> : conduction resistance between inner bottom wall and inner vertical wall in contact with the liquid space	$R_{18} = \frac{L_{i,bottom-vertical,l}}{k_{inner\ wall} A_{cross\ section,i,bottom-vertical,l}}$	(A-18)
<i>Horizontal tank</i> : conduction resistance between inner bottom wall and inner end walls in contact with the liquid space	$R_{18} = \frac{L_{i,bottom-end\ walls,l}}{k_{inner\ wall} A_{cross\ section,i,bottom-end\ walls,l}}$	
<i>Horizontal tank</i> : conduction resistance in the outer end walls in contact with the liquid and vapor spaces	$R_{19} = \frac{L_{end\ walls,v-end\ walls,l}}{k_{outer\ wall} A_{cross\ section,o,end\ walls}}$	(A-19)
<i>Horizontal tank</i> : conduction resistance in the inner end walls in contact with the liquid and vapor spaces	$R_{20} = \frac{L_{end\ walls,v-end\ walls,l}}{k_{inner\ wall} A_{cross\ section,i,end\ walls}}$	(A-20)
<i>Vertical tank</i> : thermal mass of outer top wall in contact with the vapor space	$C_1 = m_{o,top\ wall,v} c_{p,o,top\ wall}$	(A-21)
<i>Horizontal tank</i> : thermal mass of outer end walls in contact with vapor space	$C_1 = m_{o,end\ walls,v} c_{p,o,end\ walls}$	
<i>Vertical tank</i> : thermal mass of inner top wall in contact with the vapor space	$C_2 = m_{i,top\ wall,v} c_{p,i,top\ wall}$	(A-22)
<i>Horizontal tank</i> : thermal mass of inner end walls in contact with vapor space	$C_2 = m_{i,end\ walls,v} c_{p,i,end\ walls}$	
<i>Vertical tank</i> : thermal mass of outer vertical wall in contact with the vapor space	$C_3 = m_{o,vertical\ wall,v} c_{p,o,vertical\ wall}$	(A-23)
<i>Horizontal tank</i> : thermal mass of outer top wall in contact with vapor space	$C_3 = m_{o,top\ wall,v} c_{p,o,top\ wall}$	
<i>Vertical tank</i> : thermal mass of inner vertical wall in contact with the vapor space	$C_4 = m_{i,vertical\ wall,v} c_{p,i,vertical\ wall}$	(A-24)

<b>Description</b>	<b>Definition</b>	<b>Eq.</b>
<i>Horizontal tank:</i> thermal mass of inner top wall in contact with vapor space	$C_4 = m_{i,top\ wall,v}c_{p,i,top\ wall}$	
<i>Vertical tank:</i> thermal mass of outer vertical wall in contact with the liquid space	$C_5 = m_{o,vertical\ wall,l}c_{p,o,vertical\ wall}$	(A-25)
<i>Horizontal tank:</i> thermal mass of outer bottom wall in contact with liquid space	$C_5 = m_{o,bottom\ wall,l}c_{p,o,bottom\ wall}$	
<i>Vertical tank:</i> thermal mass of inner vertical wall in contact with the liquid space	$C_6 = m_{i,vertical\ wall,l}c_{p,i,vertical\ wall}$	(A-26)
<i>Horizontal tank:</i> thermal mass of inner bottom wall in contact with liquid space	$C_6 = m_{i,bottom\ wall,l}c_{p,i,bottom\ wall}$	
<i>Vertical tank:</i> thermal mass of outer bottom wall in contact with the liquid space	$C_7 = m_{o,bottom\ wall,l}c_{p,o,bottom\ wall}$	(A-27)
<i>Horizontal tank:</i> thermal mass of outer end walls in contact with liquid space	$C_7 = m_{o,end\ walls,l}c_{p,o,end\ walls}$	
<i>Vertical tank:</i> thermal mass of inner bottom wall in contact with the liquid space	$C_8 = m_{i,bottom\ wall,l}c_{p,i,bottom\ wall}$	(A-28)
<i>Horizontal tank:</i> thermal mass of inner end walls in contact with liquid space	$C_8 = m_{i,end\ walls,l}c_{p,i,end\ walls}$	

## A.2 Heat transfer coefficients in the vertical LNG storage tank

To calculate the convection heat transfer coefficients on the side walls of the vertical storage tank, the natural convection heat transfer correlation on the vertical flat plate is considered (Churchill-Chu correlation [98]):

$$Nu = \frac{h_{x,wall}L_x}{k_f} = \left\{ 0.825 + \frac{0.387Ra_x^{1/6}}{\left[1 + \left(\frac{0.492}{Pr_x}\right)^{8/27}\right]} \right\}^2 \quad (A-29)$$

where,

$$Ra_x = \frac{g\beta_f\Delta T_x L_x}{\alpha_f\nu_f} \quad (\text{A-30})$$

$$Pr_x = \frac{\nu_f}{\alpha_f} \quad (\text{A-31})$$

In Eqs. (A-30) and (A-31),  $\beta_f$ ,  $\alpha_f$ , and  $\nu_f$  are the thermal expansion coefficient (1/K), thermal diffusivity (m<sup>2</sup>/s), and kinematic viscosity (m<sup>2</sup>/s) of fluid at the reference temperature, respectively.  $g$  is the gravity acceleration (m/s<sup>2</sup>). Other parameters are described in Table A2.

**Table A2. Variables in the calculation of the convection transfer coefficients on the wall.**

$x$	Fluid	$L_x$ [m]	$\Delta T_x$ [K]	$T_{ref}$ [K]
outer-vertical wall, v	air	Length of outer vertical wall (vapor part)	$T_{air} - T_{o-vertical\ wall,v}$	$0.5(T_{air} + T_{o-vertical\ wall,v})$
outer-vertical wall, l	air	Length of outer vertical wall (liquid part)	$T_{air} - T_{o-vertical\ wall,l}$	$0.5(T_{air} + T_{o-vertical\ wall,l})$
inner-vertical wall, v	vapor phase	Length of inner vertical wall (vapor part)	$T_{i-vertical\ wall,v} - T_v$	$0.5(T_{i-vertical\ wall,v} + T_v)$
inner-vertical wall, l	liquid phase	Length of inner vertical wall (liquid part)	$T_{i-vertical\ wall,l} - T_l$	$0.5(T_{i-vertical\ wall,l} + T_l)$

The convection heat transfer coefficients on the top and bottom walls of the vertical tank are calculated based on the empirical correlations of external free convection on a horizontal flat plate.

$$h_{f,wall} = \xi \frac{k_f Nu}{L_{ref}} \quad (\text{A-32})$$

where,  $k_f$  is the thermal conductivity of the vapor and liquid phases.  $\xi$  is the heat transfer adjustment factor (the default value is 1.0). Due to the complex flow fields during the pressurization and relaxation processes discussed in Section 3.1.2, the heat transfer adjustment factor,  $\xi$  in Eq. (A-32) is set at 2.5 during the pressurization process and is gradually reduced to

1.0 during the relaxation process at the vapor-liquid interface.  $L_{ref}$  is the characteristic length and is defined in Eq. (2-29).

The correlations for the average Nusselt number,  $Nu$ , are calculated in Eqs. (2-30)-(2-32), and Eq. (A-30) is used to calculate Rayleigh number,  $Ra$ , with the temperature difference  $\Delta T$  between the fluid and surface temperatures, and the characteristic length,  $L_{ref}$ , is defined by Eq. (2-29).

### A.3 Heat transfer coefficients in the horizontal LNG storage tank

The convection heat transfer coefficient on the outer wall of the horizontal tank is calculated by using Churchill-Chu correlation [99].

$$Nu = \frac{h_{wall}D}{k_f} = \left\{ 0.60 + \frac{0.387Ra_D^{1/6}}{\left[ 1 + \left( \frac{0.559}{Pr_x} \right)^{9/16} \right]^{8/27}} \right\}^2 \quad (A-33)$$

where,  $D$  is the outer diameter of the tank. Other variables are the same as those in the vertical tank. The convection heat transfer coefficient on the inner wall of the horizontal tank is calculated by the following correlation [100].

$$Nu = \frac{h_{wall}L_{ref}}{k_f} = 0.55(Ra)^{0.25} \quad (A-34)$$

The definition of  $Ra$  is the same as Eq. (2-33). The reference length,  $L_{ref}$ , is the length of the horizontal tank. The correlation to calculate the convection heat transfer coefficients at the two end walls of the horizontal tank is similar to Eq. (A-29).

## Appendix B

### B.1 Vapor-liquid equilibrium calculations

The compressibility factor,  $Z$ , of the liquid and vapor mixtures is calculated as follows [76]:

$$Z^3 + (B - 1)Z^2 + (A - 3B^2 - 2B)Z + (B^3 + B^2 - AB) = 0 \quad (\text{B-1})$$

where,  $A$  and  $B$  are defined as,

$$A = \frac{aP}{(R_u T)^2} \quad (\text{B-2})$$

$$B = \frac{bP}{R_u T} \quad (\text{B-3})$$

The binary parameters,  $A_{ij}$ , in the liquid and vapor mixtures are defined as,

$$A_{ij} = \frac{x_i x_j \sqrt{a_i a_j} P}{(R_u T)^2} \quad (\text{liquid mixture}) \quad (\text{B-4})$$

$$A_{ij} = \frac{y_i y_j \sqrt{a_i a_j} P}{(R_u T)^2} \quad (\text{vapor mixture}) \quad (\text{B-5})$$

where,  $a$  and  $b$  are calculated by Eqs. (2-35) and (2-36), respectively.

Solving Eq. (B-1) gives three real values. For the liquid mixture, the minimum real root of Eq. (B-1) is defined as  $Z_L$ . For the vapor mixture, the maximum real root of Eq. (B-1) is defined as  $Z_V$ .

To calculate the bubble and dew pressures and temperatures, the vapor-liquid equilibrium (VLE)  $K$ -ratio of species  $i$  is defined as the ratio of the vapor mole fraction  $y_i$  to the liquid mole fraction

$x_i$ :

$$K_i = \frac{y_i}{x_i} \quad (\text{B-6})$$

Alternatively,  $K_i$  at temperature,  $T$ , and pressure,  $P$ , can be estimated by Eq. (B-7),

$$K_i \approx \frac{P_{cri_i} 10^{\frac{7}{3}(1+\omega_i)} \left(1 - \frac{T_{cri_i}}{T}\right)}{P} \quad (\text{B-7})$$

## B.2 Calculation of the bubble pressure

If the liquid mixture with mole fraction  $x_i$  is at temperature  $T$ , the initial value of the bubble pressure  $P_{bubble}$  is calculated by Eq. (B-8) [76].

$$P_{bubble}^{initial} = \sum_i^N P_{sat,i} x_i \quad (\text{B-8})$$

where,  $P_{sat}$  is the saturation pressure of species  $i$ , and is calculated by Eq. (B-9).

$$P_{sat,i} = P_{cri_i} 10^{\frac{7}{3}(1+\omega_i)} \left(1 - \frac{T_{cri_i}}{T}\right) \quad (\text{B-9})$$

Using  $P_{bubble}$  from Eq. (B-8), the initial value of  $K_i$  is calculated by Eq.(B-7). Then, the evaporated vapor mole fraction  $y_i$  is calculated:

$$y_i = K_i x_i \quad (\text{B-10})$$

Once  $x_i$  and  $y_i$  are calculated, Eq. (B-1) at temperature  $T$  and the initial pressure  $P_{bubble}$  condition can be solved. The liquid fugacity,  $\phi_i^L$ , is calculated by using  $Z_L$  solved from Eq. (B-1):

$$\ln \phi_i^L = \frac{b_i}{b} (Z_L - 1) - \ln(Z_L - B) - \frac{A}{2\sqrt{2}B} \left( \frac{2 \sum_j^N x_j A_{ij}}{A} - \frac{b_i}{b} \right) \ln \left( \frac{Z_L + (1 + \sqrt{2})B}{Z_L + (1 - \sqrt{2})B} \right) \quad (\text{B-11})$$

Similarly, the vapor fugacity,  $\phi_i^V$ , is calculated by using  $Z_V$  solved from Eq. (B-1):

$$\ln\phi_i^V = \frac{b_i}{b}(Z_V - 1) - \ln(Z_V - B) - \frac{A}{2\sqrt{2}B} \left( \frac{2\sum_j^N y_j A_{ij}}{A} - \frac{b_i}{b} \right) \ln \left( \frac{Z_L + (1 + \sqrt{2})B}{Z_L + (1 - \sqrt{2})B} \right) \quad (\text{B-12})$$

Then, the new value of  $y_i$  is updated:

$$y_i = \frac{\phi_i^L}{\phi_i^V} x_i \quad (\text{B-13})$$

The iteration of Eqs. (B-11)-(B-13) by using the new values of  $y_i$  continues until the relative difference of  $y_i$ s becomes less than  $10^{-10}$ . At the end of the iteration, if the absolute difference error between the summation of  $y_i$ s and 1 is larger than  $10^{-6}$ , the new value of bubble pressure is updated by Eq. (B-14).

$$P_{bubble}^{new} = P_{bubble} \sum_i^N y_i \quad (\text{B-14})$$

If the absolute difference error of the summation of  $y_i$  is less than  $10^{-6}$ , the bubble pressure is accepted. Then, the  $K$ -ratio is calculated by Eq. (B-6).

### B.3 Calculation of the dew pressure

If the vapor mixture with mole fraction  $y_i$  is at temperature  $T$ , the initial value of the dew pressure  $P_{dew}$  is calculated by Eq. (B-15) [76],

$$P_{dew}^{initial} = \frac{1}{\sum_i^N \left( \frac{y_i}{P_{sat,i}} \right)} \quad (\text{B-15})$$

thus, using the  $P_{dew}$ , the initial value of  $K_i$  is calculated by Eq. (B-7). Then, based on Eq. (B-6), the condensed liquid mole fraction  $x_i$  is calculated,

$$x_i = y_i/K_i \quad (\text{B-16})$$

similarly, Eqs. (B-11) and (B-12) are calculated to obtain  $\phi_i^L$  and  $\phi_i^V$ , respectively. Then the new value of  $x_i$  is updated,

$$x_i = \frac{\phi_i^V}{\phi_i^L} y_i \quad (\text{B-17})$$

The iteration is established to calculate  $x_i$ . If the change of  $x_i$  is less than  $10^{-10}$ , the summation of  $x_i$  is checked. If the absolute difference between the summation of  $x_i$  and 1 is less than  $10^{-6}$ , the dew pressure  $P_{dew}$  is accepted, and  $K_i$  is calculated. If not, the dew pressure  $P_{dew}$  is updated by Eq. (B-18),

$$P_{dew}^{new} = \frac{P_{dew}}{\sum_i^N x_i} \quad (\text{B-18})$$

#### B.4 Calculation of the bubble temperature

If the liquid mixture with mole fraction  $x_i$  is at pressure  $P$ , the initial value of the bubble temperature  $T_{bubble}$  is estimated by Eq. (B-19) [76].

$$T_{bubble}^{initial} = \sum_i^N x_i T_{sat,i} \quad (\text{B-19})$$

Based on the initial value of  $T_{bubble}$ , the bubble pressure  $P_{bubble}$  is calculated based on the method discussed in Section B.2. If the absolute difference  $|P_{bubble} - P|$  is less than  $10^{-2}$  Pa, the initial

value of  $T_{bubble}$  is accepted. Otherwise, the value of  $T_{bubble}$  is adjusted until  $|P_{bubble} - P|$  reaches less than  $10^{-2}$  Pa.

### B.5 Calculation of the dew temperature

If the vapor mixture with mole fraction  $y_i$  is at pressure  $P$ , the initial value of the dew temperature  $T_{dew}$  is estimated by Eq. (B-20) [76].

$$T_{dew}^{initial} = \sum_i^N y_i T_{sat,i} \quad (\text{B-20})$$

Then, the dew pressure  $P_{dew}$  is calculated based on the method discussed in Section B.3. If the absolute value of  $|P_{dew} - P|$  is less than  $10^{-2}$  Pa, the initial value of  $T_{dew}$  is accepted. Otherwise, the value of  $T_{dew}$  is adjusted until  $|P_{dew} - P|$  reaches lower than  $10^{-2}$  Pa.

### B.6 Dynamic viscosity and thermal conductivity of the liquid and vapor phases

The viscosity ( $\mu_{l,i}$ ,  $\mu_{v,i}$ ), and thermal conductivity ( $k_{l,i}$ ,  $k_{v,i}$ ) of liquid and vapor phases of species  $i$  are a function of temperature. The polynomial functions are fitted to the thermophysical data reported by the National Institute of Standards and Technology (NIST) [101]. The viscosity of the liquid phase mixture is calculated based on Grunberg-Nissan mixing rule [102],

$$\mu_{l,mix} = \exp \sum_i^N x_i \ln(\mu_{l,i}) \quad (\text{B-21})$$

The thermal conductivity of the liquid phase mixture is calculated based on Li model [103],

$$k_{l,mix} = \sum_i^N \sum_j^N \phi_i \phi_j k_{ij} \quad (\text{B-22})$$

where,

$$k_{ij} = 2(k_{l,i}^{-1} + k_{l,j}^{-1})^{-1} \quad (\text{B-23})$$

$$\phi_i = \frac{x_i \nu_{cri,i}}{\sum_{j=1}^N x_j \nu_{cri,j}} \quad (\text{B-24})$$

$x_i$  is the mole fraction of species  $i$  and  $\phi_i$  is the superficial volume fraction of species  $i$ .  $\nu_{cri,i}$  is the critical specific molar volumes of species  $i$  for a non-aqueous liquid system.

The viscosity of the vapor phase mixture is calculated by Herning and Zipperer model [104],

$$\mu_{v,mix} = \frac{\sum_i^N (\mu_{v,i} \cdot x_i \cdot \sqrt{M_i})}{\sum_i^N (x_i \cdot \sqrt{M_i})} \quad (\text{B-25})$$

For non-ideal gases, the mixture thermal conductivity is calculated based on a simple mass fraction weighted average of the pure species' thermal conductivities [65],

$$k_{v,mix} = \sum_i^N w_i \cdot k_{v,i} \quad (\text{B-26})$$

where,  $w_i$  is the mass fraction of the species  $i$ .